VCSEL MODELING AND PARAMETER EXTRACTION FOR OPTICAL LINK SIMULATION AND OPTIMIZATION

A Dissertation
Presented to
The Academic Faculty

by

Alirio A. Melgar Evangelista

In Partial Fulfillment
of the Requirements for the Degree
Doctor of Philosophy in the
School of Electrical and Computer Engineering

Georgia Institute of Technology
August 2021

COPYRIGHT © 2021 BY ALIRIO A. MELGAR EVANGELISTA

VCSEL MODELING AND PARAMETER EXTRACTION FOR OPTICAL LINK SIMULATION AND OPTIMIZATION

Approved by:

Dr. Stephen E. Ralph, Advisor
School of Electrical and Computer Engineering
Georgia Institute of Technology

Dr. Kent D. Choquette
Electrical and Computer Engineering Department
University of Illinois at Urbana-Champaign

Dr. Benjamin D.B. Klein
School of Electrical and Computer Engineering
Georgia Institute of Technology

Dr. Duncan L. MacFarlane
Department of Electrical and Computer Engineering
Southern Methodist University

Dr. Russell D. Dupuis
School of Electrical and Computer Engineering
Georgia Institute of Technology

Date Approved: July 19, 2021

A la más grande fortuna que me ha dado Dios, mi familia,

gracias por todo el apoyo y amor

A mis queridos padres, con mucho cariño

ACKNOWLEDGEMENTS

I would like to thank my advisor Prof. Stephen E. Ralph for providing me the opportunity to work in his lab. I truly appreciate the freedom he gave me to pursue my research and the support he provided through the years. His guidance and advice from day one will stay with me throughout my career. Without his hard work and dedication, none of this research would have been possible.

I would also like to thank Prof. Ben Klein. I very much enjoyed the multiple fruitful discussions about my work, his great ideas, and never-ending optimism. His great support and understanding of VCSEL structures and simulations as well as the many office hours of discussion have led me to develop a deeper understanding of laser physics.

Special thanks to Prof. Duncan MacFarlane for introducing me to the world of optics and optical communication. His work and love for research sparked my interest for this field and ultimately led me to pursue a PhD. I would like to thank my reading committee members – Prof. Russel D. Dupuis and Prof. Ben Klein. I am grateful for their time and effort, as well as for their questions and guidance in the last chapter of my PhD. I am extremely grateful to Prof. Russel D. Dupuis for agreeing to be in my reading committee on short notice. I am also indebted to Prof. Kent D. Choquette for agreeing to be my external committee member and for introducing me to the world of coupled cavity VCSELs.

To my colleagues and friends, thank you for all the memories and lunches together: Dr. V.A. Thomas, Dr. Justin Lavrencik, Dr. Siddharth Varughese, Dr. Jerrod Langston,

Daniel Lippiatt, Gareeyasee Saha, Alec Hammond, Daniel Garon, Christian Bottenfield, Michael Hoff, and Arjun Khurana. You all made my learning experience more enjoyable and meaningful.

Lastly, to my parents, thank you for the unconditional support throughout my life, my brother and sister for their encouragements and support, and my family in El Salvador for always being there.

TABLE OF CONTENTS

LIST OF TABLES

LIST OF FIGURES

LIST OF ABBREVIATIONS

AWG	Arbitrary Wave Generator
AWGN	Additive White Gaussian Noise
BER	Bit Error Rate
BLW	Baseline Wander
BW	Bandwidth
CD	Chromatic Dispersion
DAC	Digital to Analog Converter
DFB	Distributed Feedback Laser
DBR	Distributed Bragg Reflector
DMA	Differential Mode Attenuation
DMD	Differential Mode Delay
EA	Error Analyzer
EMBc	Calculated Effective Modal Bandwidth
ER	Extinction Ratio
FIR	Finite Impulse Response
FP	Fabry-Perot
MD	Modal Dispersion
MM	Multimode
MMF	Multimode Fiber
MPN	Mode Partition Noise
NRZ	Non-return to Zero
OMA	Optical Modulation Amplitude

OOK	On-off Keying
PAM	Pulse Amplitude Modulation
PD	Photodiode
PRBS	Psuedo-Random Bit Sequence
PSD	Power Spectral Density
RIN	Relative Intensity Noise
SER	Symbol Error Rate
SM	Single Mode
SMF	Single Mode Fiber
SNR	Signal-to-Noise Ratio
TIA	Trans-impedance Amplifier
VCSEL	Vertical-Cavity Surface-Emitting Laser
VOA	Variable Optical Attenuator

SUMMARY

Vertical cavity surface emitting lasers (VCSELs) along with multimode fiber (MMF) have long dominated the short reach data communication links. As requirements in high-speed optical communications continue to increase, these systems are becoming increasingly complex. To meet the growing bandwidth demand, optical links are commonly turning to equalization, and multilevel modulation formats. The need for an accurate physics-based rate equation model is critical for the design and analysis of VCSEL links as we move past 25Gb/s. To achieve higher data rates, VCSEL bandwidth is no longer a sufficient metric, since power consumption, noise and device reliability must be considered. Therefore, there is an ever-growing need for computer-aided optical link design. The overall objective of this research is to present a comprehensive set VCSEL models, as well as parameter extraction tools to better understand VCSEL performance in short reach optical links.

CHAPTER 1

INTRODUCTION

Due to their mass production, semiconductor laser diodes have become key components in optical communications systems. In direct detect optical links, laser diodes act as the sources in which the pulses of light travel along the fibers to convey information. In short reach optical communications, vertical cavity surface emitting lasers (VCSELs) currently dominate these types of applications [1]. As their name suggest VCSELs emit light perpendicular to the surface. Their low power consumption, lower manufacturing cost, and high reliability have made them a popular choice for short reach applications. A great deal of work has led us to the VCSEL simulation tools we have today. Yet as data rates continue to increase, VCSELs models will need to account for single and multimode operation, as well as relative intensity noise (RIN), and the underlying RIN enhancement. Furthermore, bias dependent parasitics, pre-emphasis, pulse shaping, and equalization are required to accurately depict and influence system level designs [1],[2]. The accurate modeling of these devices is needed especially as we move toward higher modulation formats, which are required to keep up with bandwidth demands.

Today's short reach optical links are primarily found in datacenters and are usually less than 100 meters in length [3],[4]. In this space, VCSEL technology operating at around 850nm is typically used. Optical links are comprised of multiple components and technologies, which can be classified into three categories: the transmitter, the channel (optical fiber), and receiver [5]. The transmitter is made up of the transmitter electronics and the VCSEL itself. The fiber used is typically multimode fiber and is categorized as

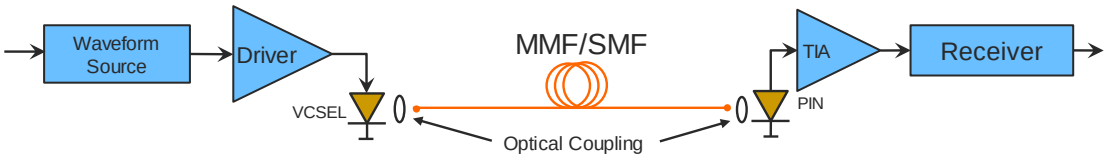

Figure 1. 1 Direct detect VCSEL optical link

OM1, OM2, OM3 and OM4 fiber, the major differences being their modal bandwidth measured in MHz·km and their reach [6]. Finally, the receiver is composed of a PIN diode followed by a TIA and decision circuitry. Figure 1. 1 depicts such a link.

As data rates keep increasing, the need for 25Gbps+ links are on demand. Here, the criteria to measure a reliable link is usually through its bit error rate (BER) where a BER of $1x10^{-12}$ is typically considered error free [7]. Since information in multimode links is generally transmitted through the direct modulation of VCSELs, an optical link's BER is highly dependent on VCSEL characteristics. A VCSEL's bandwidth, optical noise sources, temperature dependence, optical modulation amplitude (OMA), and extinction ratio (ER) will greatly impact the link's BER. Numerous groups have created models to account for such impairments. For example, the IEEE 802.3 group has 10GbE spreadsheets that account for some of these impairments [8], classifying each one as a power/rise time penalty. However, as we move to higher speeds and modulation formats for VCSEL optical links, it will be difficult to accurately estimate link performance through the approximations of this model [2]. Additionally, models that capture only the small signal modulation response of VCSELs would not be able to fully capture the physical phenomena seen in high-speed multilevel modulation formats as the tighter spacing between the symbol levels in these signals would make them more susceptible to noise [9].

This dissertation is arranged into five chapters. We begin with some background information in Chapter 2. Chapter 3 introduces our single mode VCSEL rate equation model which accurately captures both ISI and noise from experimental data. We show that joint optimization of both small signal and RIN spectra measurements as well as multi-objective optimization techniques improve the accuracy of the extracted parameters. Chapter 4 further extends this model to multimode. We show that a multimode model is necessary to account for the intra and intermodal effects and underlying RIN enhancement when launching VCSEL modes into multimode fiber. Here we show the effects that positive and negative correlations have on the VCSEL RIN spectrum. We believe to be the first group to both show the existence of positive and negative correlations in VCSELs. We further believe to be the first group to show that these positive and negative correlation are a cause of increased RIN at lower frequencies. Chapter 5 introduces our component characterization setup and includes a detailed analysis into VCSEL characterization through scattering parameters; here, our characterization and experimental test bed is described. We then tie our modeling efforts by comparing experimental results with our simulation tools. Here we show possible methods to push VCSELs to 100G through various techniques. Chapter 6 gives some concluding remarks and future outlook into VCSEL modeling.

CHAPTER 2

BACKGROUND INFORMATION

The history of communication can be traced back to the origin of speech. Throughout history, clever methods have been developed to increase and improve communication among us. Before the discovery of electricity, early means of communication over a distance included such things as fire beacons or smoke signals [10]. Initially electrical communication systems such as the telegraph were able to transmit Morse code with data rates around 10b/s. With the first transatlantic telegraph completed in 1866 we were able to communicate across continents in minutes rather than weeks. Only a decade later, Alexander Graham Bell was granted a United States patent for what we now know as the telephone [11]. This device sent analog signals through a twisted pair of insulated wires. As the popularity of the telephone increased, the data rates were not sufficient as the need for increased bandwidth and distance became apparent. The coaxial cable became widely used around the 1940s and could support bandwidths up to 3MHz, enough for 1 TV channel or 300 voice channels. Unfortunately, at higher frequencies and longer lengths, wires become transmission lines. In this regime the inductance and capacitance of the coax cause frequency dependent losses, severely limiting transmission length and dates rates [10]. To increase the allotted bandwidth, microwave communication systems became popular around 1950. With carrier frequencies of ~1-10GHz, speeds of around 100Mbps (~1% of the carrier frequency) were possible.

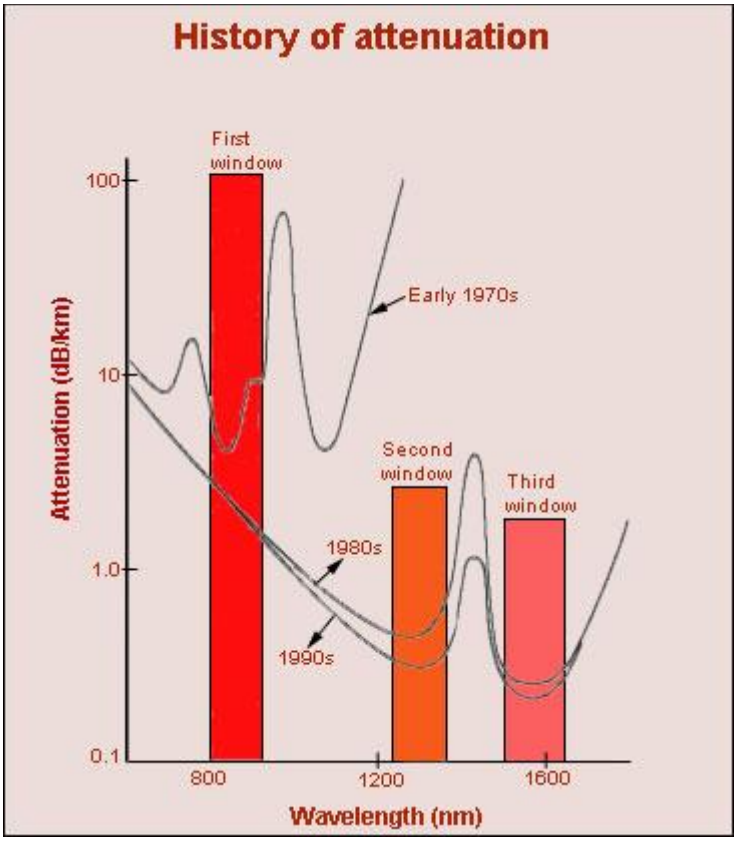

Figure 2. 1 Attenuation of optical fiber over the years [12]

To further improve electrical links, scientists turned to optics. The invention and demonstration of the first laser in the 1960s led to a search for a viable transmission medium [10],[12],[13]. Initially, optical fibers were not considered, as only 10% of light launched into a fiber a few meters long emerged at the other end [10]. In 1966, it was suggested that losses found in optical fibers were not limited by fundamental physical effects such as scattering and could be dramatically reduced by removing impurities from silica glass [14]. By 1970 fiber losses were reduced to 20dB/km, and after two years the same team produced fibers with a loss of only 4dB/km [15]. In 1979 scientist in Japan were able to reduce losses to 0.2dB/km at 1550nm, this limit is set by Rayleigh scattering which affects modern fibers to this day [10],[12],[15]. As such, low loss fibers with attenuation

profiles such as those depicted in Fig. 2.1, became the preferred medium for optical communication. Coincidentally, by 1970, groups in Russia and at Bell Laboratories demonstrated GaAs semiconductor lasers operating at room temperature [10]. The creation of compact optical sources and low loss optical fibers led to a new era of optical fiber communication. With optical carrier frequencies of ~100THz, optical communication systems have the potential of carrying information at bit rates of ~1Tb/s. The potential bandwidth of optical communication systems is the driving force behind research and deployment of light wave systems.

It is difficult to imagine a world without the connectivity we are afforded today. Optical fiber communications links are widely used in long distance communication as well as datacenters to connect everything around us. For long distance communications, single mode fiber is typically used. The 8-micron diameter core in single mode fibers is designed to carry light directly down the fiber. Transmission lengths of tens of kilometers are possible due to the low loss of about 0.2dB/km [10],[15]. Multimode on the other hand, has a larger core and is therefore able to collect more light. With core diameters of 50 microns or more, it allows for simpler connections, enabling more relaxed coupling tolerances. Unfortunately, the larger core comes with its limitations. Multimode step index fibers are severely bandwidth limited when compared to single mode ones. Multipath propagation and group delay experienced over long distances and at high speeds limit both reach and rate. Multimode graded refractive index profile fibers have been manufactured to limit theses effects. Even so, group delay is still an issue which limits modal bandwidths to a few gigahertz per kilometer. Due to lower cost, multimode fiber links alongside with

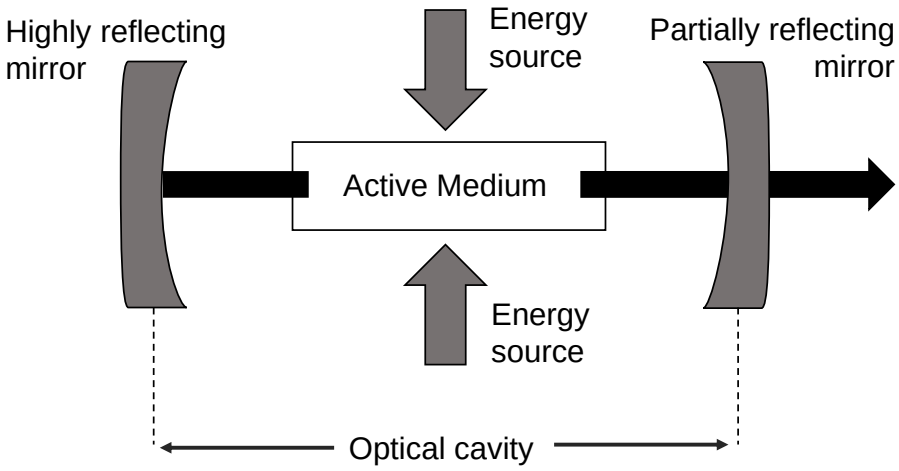

Figure 2. 2 Components of a typical laser

directly modulated VCSELs are mainly used in short reach communications such as data centers [1][3].

As we begin modeling higher speeds and more complex modulation formats, the reliability of simulation models will depend on the extent to which they can accurately capture physical phenomena. For direct detect VCSEL links, major limitations come from the laser itself. These limitations are compensated through various techniques such as equalization and higher modulation formats [1]. Therefore, it is important to have tools that are capable of accurately capturing noise as well as the dynamic and transient properties of VCSELs in optical links. When pushing VCSELs to their performance limits, colored relative intensity noise (RIN) in addition to the typical small signal modulation response will become a deciding factor and therefore need to be accurately calibrated in optical link models. Link models must also account for inherent VCSEL properties when coupled with multimode fiber. These includes modal dispersion, chromatic dispersion, mode partition noise, and lack of polarization control which limit the achievable fiber reach [2][16].

Hence, accurate VCSEL modelling can provide immense benefits to device and link optimization.

2.1 Semiconductor Laser Fundamentals

In its most basic form, a semiconductor laser such as the one depicted in Fig 2.2, consists of 3 distinct parts, specifically a:

a) Gain medium

b) Pumping mechanism

c) Feedback (optical)

Here, the gain medium consists of a material with photoluminescent properties. The existence of such materials allows for the existence of optical gain and therefore the amplification of light. When a pumping mechanism such as a forward voltage is applied electrons combine with holes and emit light. Mirrors at each end confine light until it is amplified, and laser oscillation is generated.

It is surprisingly simple to describe the basic concept of how lasers function. In general, there are two different transitions that occurs between a photon and electron. These

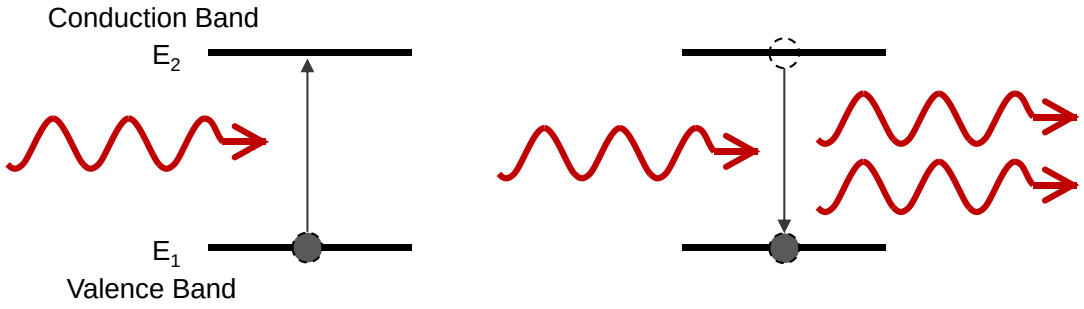

Figure 2. 3 Absorption and stimulated emission

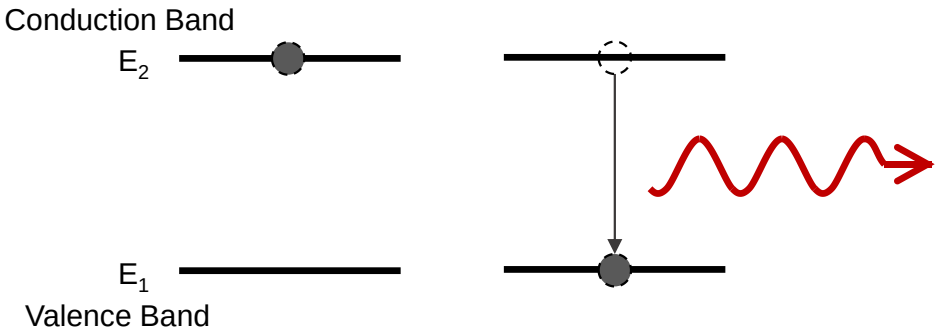

Figure 2. 4 Spontaneous emission

include absorption, and emission, of which the latter can be separated in spontaneous emission and stimulated emission. Absorption occurs when electron absorb photons causing them to gain energy and jump to higher energy levels. When an electron is at a higher energy state, if a photon with the exact energy disturbs the system, the electron will drop the lower level emitting a new photon with the exact wavelength, phase and direction as the original photon which disturbed the system. This process is called stimulated emission and is depicted in Fig 2.3.

When an electron is exited to a higher energy level, it does not tend to stay there forever. Eventually if the exited electron is not disturbed it will suddenly travel to a lower energy state unleashing a single photon with an energy equivalent to the difference between the two energy levels. This process is called spontaneous emission and is depicted in Fig 2.4.

2.2 Modelling VCSELs

To improve performance, VCSEL structures have become increasingly complex. Simulation tools have therefore been developed to understand their operation and aid in their design. Simulating these devices can be achieved through detailed models where a

device's internal mechanisms and characteristics are considered. These models can incorporate multidimensional analysis of spatial behavior and detailed solutions of optical characteristics which take very long to solve [17],[18]. Analysis of diode lasers dynamics can be done through the laser rate equations, which can vary in complexity, based on the type of application [19]-[22]. In problems where coherent properties of light are not critical, these equations can describe the laser characteristics without much complexity. Such models can incorporate multiple photonic and electronic elements. They also are easy to manipulate, and can sweep through large number of parameters, typically necessary in optical link design.

2.2.1 Laser Rate Equations

A generalized form of the laser rate equation is presented in [23]. These equations are widely used to model edge emitting lasers similar with a structure similar to Fig. 2.5 [24]. Here we have assumed that lasing occurs only on one optical mode. This set of equations relate the number of photons N_p inside the laser cavity and the number of exited carriers N responsible for optical gain.

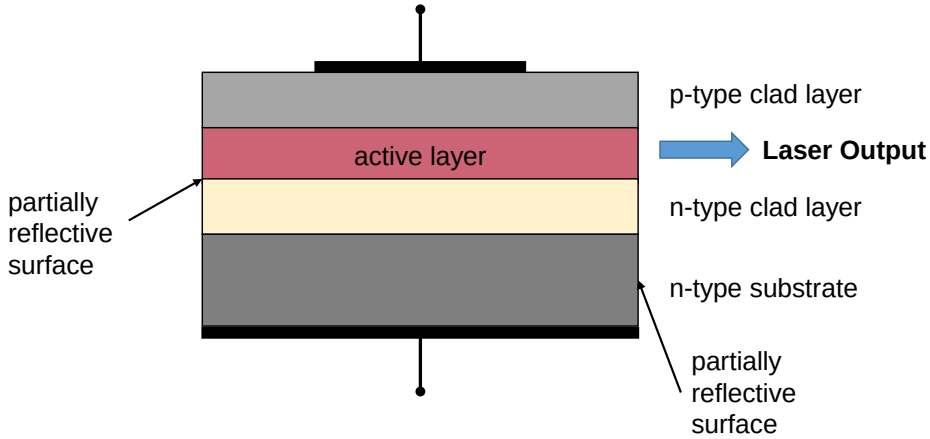

Figure 2. 5 Basic structure of a semiconductor laser [24]

$$V\frac{dN}{dt} = \frac{\eta_i I}{q} - \left(R_{sp} + R_{nr}\right)V - (R_{21} - R_{12})V \tag{2.1}$$

$$V_p\frac{dN_p}{dt} = (R_{21} - R_{12})V - \frac{N_p V_p}{\tau_p} + R'_{sp}V \tag{2.2}$$

Here, η_i is the injection efficiency, q the electron charge, and I the injected current in amps. R_{nr} represents nonradiative recombination. R_{sp} represents the portion of carriers that recombine spontaneously, of which a certain fraction (R'_{sp}) emit photons. R_{21} is the recombination of carriers via stimulated emission while R_{12} defines the photons in the photon reservoir which can be absorbed. τ_p is the photon lifetime, V is the ratio of the active region volume of the carrier reservoir and V_p is the mode volume of the photon reservoir. Simplified models such as (2.1, 2.2) are useful to gain understanding into semiconductor laser behavior, such as its small and large signal characteristics. Note that by dividing equation (2.1) by V and (2.2) by V_p we arrive at the more widely used carrier and photon density laser rate equations.

In (2.1), dN/dt alone, describes the rate of change in carrier density of the device. As more current is injected dN/dt is expected to increase linearly with I. Furthermore, $-\left(R_{sp} + R_{nr}\right)$ denotes the carriers removed from the active region by spontaneous emission and nonradiative carrier recombination processes. This carrier loss is widely characterized as the carrier lifetime, τ_n, such that $\frac{dN}{dt} \propto -N/\tau_n$. Here the carrier lifetime, τ_n, in the carrier rate equation represents the time constant of exponential decay of carriers. The final term in the carrier rate equation, $-(R_{21} - R_{12})$, represents the carrier losses due

to stimulated photon emission which depends on both the optical gain and photon density of the given mode. In this process an electron in the conduction band and a hole in the valence band are removed to create a photon in the given mode. This loss is analogous to how we handle electron losses but characterized as a net loss through the photon lifetime τ_p.

Conversely, in (2.2), dS/dt describes the rate of change in photon density of the device. Here, the photon density increases due to optical gain unlike in (2.1) where carriers are lost. Photon loss here occurs within the cavity due to mirror losses, scattering and unwanted material absorption. Finally, while some carriers recombine to spontaneously at the rate $R_{sp}V$, a certain fraction emit photons into the mode of interest at the rate $R'_{sp}V$, sometimes written as $\beta_{sp}R_{sp}V$, where β_{sp} is the more commonly known spontaneous emission factor.

These equations have been used extensively in order to understand the turn on and transient behaviour of laser diodes. Further improvements to these equations can be made by including nonlinear gain, as well as additional equations to model the phase, thermal, and carrier transport properties and their effects on the lasing mode [25]. Therefore, the rate equations have been extensively used to explain a considerable range of laser diode characteristics. Previous works have used the rate equations to study laser dynamics of several lasers. An IEEE search shows laser rate equations being used back in the 1960's to study relaxation oscillations found in ruby lasers [26]. Spatial dependence of single mode lasers was later studied in 1966 [27]. By 1976 theoretical calculations based on rate equations for gigabit data transmission were being developed [28]. Equivalent circuits

based on laser rate equations, have been used to integrate and facilitate the design of optoelectronic components [29]. Initial studies model the laser diode as a parallel RLC circuit [30]. Further studies elaborate on this method by including effects such as spontaneous emission, and self-pulsations [31]. The following year laser noise was added to simulate relative intensity noise (RIN). The 1990s saw an emergence in tools to aide in laser system level design. Frequency subtraction to extract the intrinsic response of the laser diode lasers was proposed by P.A. Morton *et. al.* [32] and later implemented to extract DFB laser parameters [33]. We note that this extraction process was one of the first to extract laser parameters from the measured small signal modulation response and compare it to experimentally measured data. Results showing extracted parameters using frequency and time domain measurements process was later presented in [34].

2.3 Intensity Noise

The origins of laser noise can be classified as quantum noise, or mechanical noise. While quantum noise is associated as spontaneous emission in the gain medium, mechanical noise arises from outside influences such as the current source, temperature fluctuations or vibrations of the laser resonator. While the noise performance of electronic systems is often limited by thermal noise, optical systems are usually limited by quantum noise. Not only does it determine the overall intensity fluctuations, but it also determines the laser linewidth and transient behavior. In part due to the one-to-one correlation between the spectra of the intensity noise and the intrinsic response of the laser itself. Stimulated emission in lasers is the primary source of laser light. The major source of noise is caused by the amplification of spontaneous emission which in it of itself is a random process. At low light levels spontaneous emission and therefore noise is a significant portion of laser light. Since short

reach optical commutations are largely direct detect systems, intensity modulation may require large swings which may send signals with laser light containing near the threshold level of operation. Therefore, there is an increasing need to understand intensity noise and its effect in optical communication systems. Though the non-stochastic laser rate equations in section 2.2 give us insight into how laser parameters affect the VCSEL's frequency response, they lack the statistical properties of the emitted light. The study of laser noise, primarily RIN, in optical link design is important since it generates intensity fluctuations which affects transient behaviors and limits the highest attainable signal-to-noise ratio (SNR) corresponding to the system level BER [2].

Historically, low complexity modulation formats such as 2 level pulse amplitude modulation (PAM) signaling has been used. PAM-2, shown in Fig 2.6a has been widely used and adopted in short reach optical communication links. As the need faster data rates increases, many are turning to PAM-4, as shown in Fig 2.6b. PAM-4 systems are used in order to double the bitrate without the need to double the required bandwidth. Unfortunately, signal impairments such as jitter, loss, intersymbol interference (ISI) and noise will have to be reevaluated as they behave differently in PAM-4 signaling [35]-[37]. Therefore, the need for an accurate laser model capable of accurately capturing laser noise

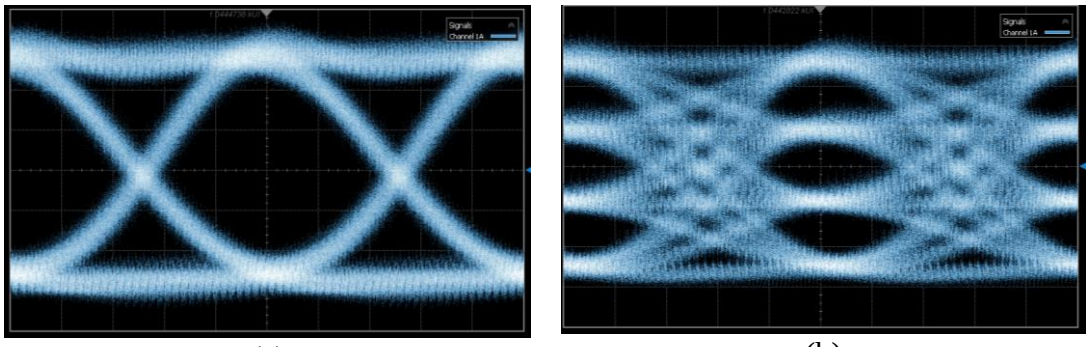

(a) (b)

Figure 2. 6 (a)PAM-2 and (b)PAM-4 formats at 26Gbaud

is necessary. Such laser models can be used to study the effects of transmitter and receiver side equalization in PAM-2 and PAM-4 systems and its impact on noise.

2.3.1 Langevin Noise

RIN through Langevin noise sources have become a popular approach to model laser noise [23]. Here we assume that noise originates from shot noise, a quantum noise effect due in part to the discreteness of photon and electrons. This noise is associated with the discrete random flow of particles into and out of the carrier and photon reservoir. Therefore, photon and carrier numbers rather than density rate equations are used. Laser noise is evaluated through spectral densities represented as auto and cross correlations. The auto correlation strengths $\langle F_i F_i \rangle$ are evaluated by summing over all shot noise contributions over all rates of flow into and out a reservoir i and is strictly positive. Cross-correlation strengths $\langle F_i F_j \rangle$ are computed over the sum of shot noise contributions that affect two reservoirs simultaneously. These cross-correlations are between reservoir i and j and are strictly negative. Therefore, the rates in and out of photon and carrier reservoirs and can be described as such [23]:

$$\langle F_i F_i \rangle = \sum R_i^+ + \sum R_i^- \tag{2.3}$$

$$\langle F_i F_j \rangle = -\left[\sum R_{ij} + \sum R_{ji}\right] \tag{2.4}$$

Here, R_i^+ and R_i^- are rates of particle flow into and out of the reservoir. R_{ij} and R_{ji} are rates of particle flow between two reservoirs. The transitions into and out of the carrier and photon reservoirs are shown in Fig. 2.7.

Noise can be added to laser rate equations through the addition of Langevin sources to the carriers and photons:

$$V\frac{dN}{dt} = \frac{\eta_i I}{q} - \left(R_{sp} + R_{nr}\right)V - (R_{21} - R_{12})V + F_N(t) \tag{2.5}$$

$$V_p\frac{dN_p}{dt} = (R_{21} - R_{12})V - \frac{N_p V_p}{\tau_p} + R'_{sp}V + F_p(t) \tag{2.6}$$

here, $F_N(t)$ and $F_p(t)$ are Langevin noise sources that account for RIN. Note that these noise sources must be added to the carrier and photon number rate equations since (2.3) and (2.4) are based on particles in and out of the carrier and photon reservoirs. By solving the rate equations (2.5), (2.6) at steady state such that $dN/dt = dN_p/dt = 0$ we find that $(N_p V_p)/\tau_p = (R_{21} - R_{12} + R'_{sp})V$. Since the material gain per unit length is proportional

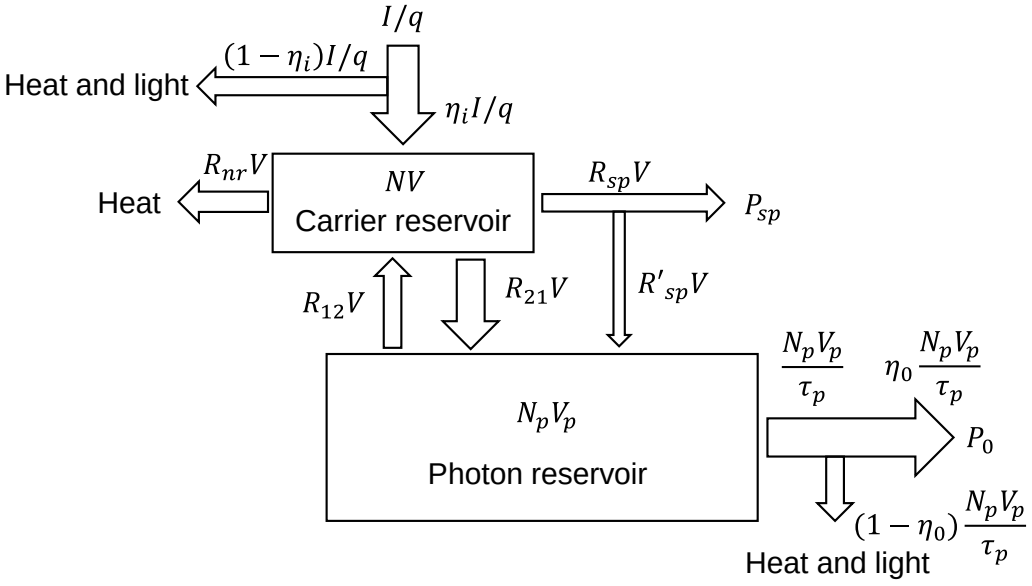

Figure 2. 7 Carrier and photon reservoir particle flow [23]

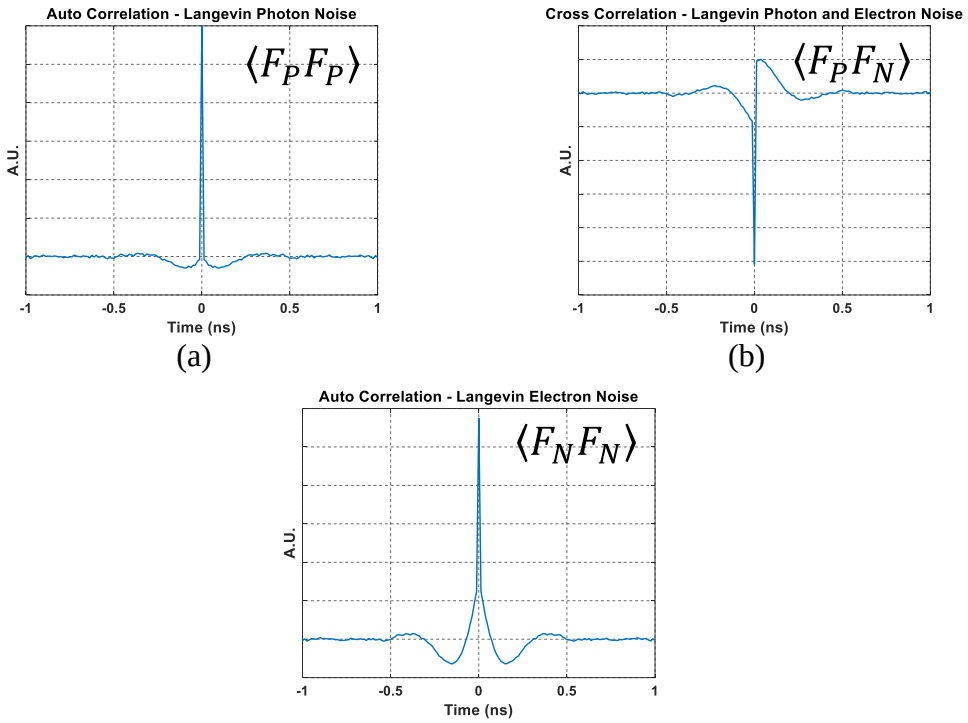

Figure 2. 8 a) Auto correlation of the Lagevin photon noise $\langle F_P F_P \rangle$. b) Cross correlation between the Langevin photon and electron noise $\langle F_P F_N \rangle$. c) Auto correlation of the Langevin electron/carrier noise $\langle F_N F_N \rangle$. Note the inherent negative and positive correlation between and among the photon and electron sources given by (2.3, 2.4).

to the growth of the photon density as it propagates through the material we can also determine that $g = \frac{1}{N_p}\frac{dN_p}{dz} = \frac{1}{v_g N_p}\frac{dN_p}{dt} = \frac{1}{v_g N_p}(R_{21} - R_{12})$ or in simpler terms $R_{\text{stimulated}} = R_{21} - R_{12}$ such that $R_{12} = R_{21} - v_g g N_p$. Furthermore, due to fundamental relations which define the downward transition rate in terms of a weighted stimulated rate constant we set $R_{21} = R'_{sp} N_p V_p$. By assuming above threshold operation such that $N \rightarrow N_{th}$ and $\Gamma v_g g \rightarrow 1/\tau_p$ we find that $R_{sp} - R'_{sp} + R_{nr} = \eta_i I_{th}/qV$, and arrive to the following correlations:

$$\langle F_P F_P \rangle = 2\Gamma \mathrm{R}'_{sp} N_p \left[1 + \frac{1}{N_p V_p}\right] \tag{2.7}$$

$$\langle F_P F_N \rangle = -\left(2\mathrm{R}'_{sp} N_p \left[1 + \frac{1}{2N_p V_p}\right] - \frac{v_g g N_p}{V_p}\right) \tag{2.8}$$

$$\langle F_N F_N \rangle = \frac{2R'_{sp} N_p}{\Gamma}\left[1 + \frac{1}{2V_p N_p}\right] - \frac{v_g g N_p}{V} + \frac{\eta_i (I + I_{th})}{qV^2} \tag{2.9}$$

The above correlations are delta functions as shown in Figure 2.8. These correlations will be referred as the Langevin photon and carrier noise correlations. Note that the Langevin noise sources plotted in Fig. 2.8 are acquired by taking the correlation of the difference of the laser noise at each instance of time. This serves as a check that the initial Langevin noise sources are in fact white and are then filtering by the rate equations such that they are shaped, as can be seen in Fig 2.9. Interestingly enough, we see that the photon noise

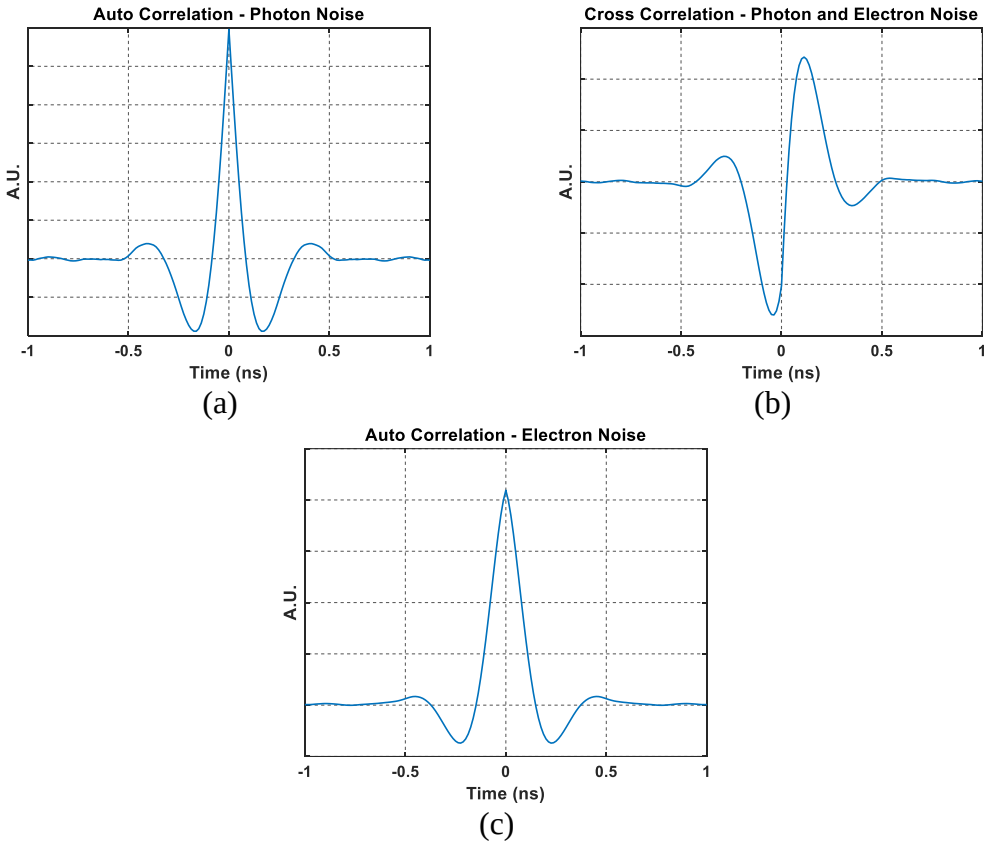

Figure 2. 9 a) auto correlation of the photon noise, this can be measured experimentally b) cross correlation between photon and electron noise c) auto correlation of electron noise

correlations, are in the order of nanoseconds, which is closer to the lifetime of electrons. Therefore, electrons interactions play a vital role and can be characterized through laser noise. As such, capturing laser noise is vital to the understanding electron and photon interactions.

To summarize, white Langevin noise sources are capable of simulating intensity noise for the laser rate equations. This noise is largely dependent on laser parameters some of which can be experimentally measured and/or extracted from experimental measurements [38].

Though models depicting laser noise exist, they are rarely implemented in optical link designs and are rather treated as Gaussian noise sources [8],[39]. A well-known stochastic rate equation model aimed at optimizing optical links is the VISTAS model [17]. Unfortunately, finding a set of parameters that match both the modulation response and RIN spectra at multiple operating conditions is extremely difficult without a prior knowledge of the design and/or structure of the laser. Laser manufacturers rarely disclose this information. Therefore, there is a need to model direct detect lasers and extract laser parameters from measured data in such a way that would allow optical link designers accurate representation of laser characteristics.

2.4 Multimode Optical Links

We can generalize all optical communication systems into 3 parts: an optical transmitter, the communication channel, and an optical receiver [5]. Here, the optical transmitter receives an electrical signal and converts it into the optical domain. This conversion is generated by modulation of the optical carrier wave, through an external modulator or by direct modulation of the laser injection current. The modulated optical wave is then

launched into the communication channel, usually fiber. The main role of the communication channel is to be as transparent as possible, as to not distort the optical signal. After exiting the communication channel, the signal reaches the optical receiver which converts the optical channel back into the electrical domain. In direct detect optical links the optical receiver consists of a photodetector and an amplifier/TIA as depicted in Fig 5.3.

2.4.1 Modulation Formats

Historically, PAM-2 formats widely known as non-return-to-zero (NRZ), or on-off keying (OOK) have been widely used for short reach optical communications. Here, the electrical bit "1" is associated with a higher optical intensity while bit "0" is associated with a lower optical intensity. On the other hand, intensity in PAM-4 systems is represented as levels identified from 0-3, with each level representing two bits of information. PAM-4 serial data links have become a popular modulation formats as VCSEL bandwidths begin to stagnate. For example, in 400GbE, a configuration system with 8 lanes running at 56Gbps is gaining the most traction. This 56Gbps lane data rate is possible through PAM-2 or PAM-4. Therefore, for accurate assessment of optical link impairments for PAM-4 systems, transmitter and receiver measurements must be redefined.

While a 56Gbps NRZ lane rate creates a linear transition from existing 25/28G lanes, channel loss and reflections will be more difficult to manage at these speeds. Therefore, a temporary solution would be to move to 25/28Gbaud PAM 4 signaling. In such a case, problems that have been dealt and solved at 28 Gbps PAM-2, especially those dealing with the inherent channel loss, can be reused again. In part due to the fact that

PAM-4 frequency/bandwidth requirements are similar to those encountered in PAM-2. PAM-4 though, would require more chip real state and power [40],[41]. When compared to PAM-2, PAM-4 gives you smaller eye opening, and therefore for a given amplitude swing an SNR penalty of 9.6dB is taken. Therefore, we primarily use PAM-4 when we wish to double the bit rate, or when we wish to increase propagation distance at a given bit rate. Therefore, modulation formats are highly dependent on the reach and speed requirements of the channel.

2.5 IEEE 10G and 25G Link Model

To estimate link performance, we first turn the IEEE model [8],[42],[43]. This tool was initially developed to understand the potential tradeoffs between various link penalties which are then translated to power penalties which correspond to a power budget model. Here, penalties include effects such as ISI, mode partition noise (MPN), and RIN which impact the total extinction ratio and/or OMA. Losses and modal effects found in fiber are also considered. Penalties are seen as signal degradations which increase noise and reduce receiver sensitivity, limiting reach at a given speed.

As a reminder, these penalties assume a Gaussian impulse response from the laser and multimode fiber, each with a specific 10%-90% rise time. The normalized impulse response of the laser, fiber and receiver channel can then be written as in terms of the RMS width, σ_t ,of the impulse response of the channel [42]-[44]:

$$h(t) = \frac{1}{\sigma_t\sqrt{2\pi}} e^{-\frac{t^2}{2\sigma_t^2}}$$

The optical receiver is assumed to have a non-equalized raised cosine response, in these calculations the optical receiver bandwidth is usually 70-75% of the baudrate. These calculations were initially intended for systems similar to those of 850nm 10GBase-SR serial LAN physical layer specifications. These systems correspond to directly modulated VCSEL links with up to 300 meters of multimode fiber.

2.5.1 Penalty due to Fiber

To calculate dispersion related penalties, we must first calculate the response time of the communication channel [42],[43]. Therefore, the exit response time is:

$$T_e = \sqrt{T_s^2 + 10^6 \left[\left(\frac{C_1}{BW_{me}} \right)^2 + \left(\frac{C_1}{BW_{cd}} \right)^2 \right]} \tag{2.10}$$

where T_s is the laser rise time, since we are assuming the fiber has a Gaussian response $C_1 = 480\ ns \cdot MHz$, and BW_{me} and BW_{cd} are the 3dB optical bandwidths due to modal and chromatic dispersion. Chromatic dispersion in a fiber link is defined as:

$$BW_{cd} = \frac{0.187}{L\sigma_\lambda} \frac{10^6}{\sqrt{D_1^2 + D_2^2}} \tag{2.11}$$

$$D_1 = \frac{S_0}{4} \left(\lambda_c - \frac{\lambda_0^4}{\lambda_c^3} \right) \tag{2.12}$$

$$D_2 = 0.7\sigma_\lambda S_0 \tag{2.13}$$

Table 2. 1 Fiber Standards and Reach for OM3, OM4, and OM5

	OM3	OM4	OM5
Core Size (μm)	50	50	50
Min. Modal Bandwidth (GHz-km)	2@850nm	4.7@850nm	4.7@850nm, 2.47@953nm
10GbE	300m	400m	400m
40GbE	100m	150m	150m
100GbE	75m	150m	150m

Where, L is the fiber length in km, σ_λ is the RMS width of the laser spectrum in nm, S_0 is the dispersion slope parameter ps/(nm^2·km). λ_c is the laser center wavelength in nm, and λ_0 is the zero dispersion wavelength in nm.

The effective modal bandwidth, which is dependent on fiber length is defined as:

$$BW_{me} = \frac{BW_m}{L} \tag{2.14}$$

The modal bandwidth, BW_m, for multiple fiber types are depicted in Table 5.1

Finally, the optical receiver rise time is given by:

$$T_r = \frac{C_2}{BW_r} 10^3 \tag{2.15}$$

Where $C_2 = 329\ ns \cdot MHz$ and BW_r is the 3dB electrical bandwidth of the optical receiver. The approximate 10% to 90% composite optical link rise time can now be computed as:

$$T_c = \sqrt{T_e^2 + T_r^2} \tag{2.16}$$

Which allows us to calculate the dispersion related link penalties in our channel.

2.5.2 Power Penalty due to Intersymbol Interference

The power penalty due to ISI is defined as [44],[45]:

$$P_{isi} = 10\log_{10}\left(\frac{1}{2h_e(0) - 1}\right) \tag{2.17}$$

Such that:

$$h_e(0) = \text{erf}\left(\frac{b_g T_{eff}}{T_c\sqrt{8}}\right) \tag{2.18}$$

Here, $b_g \approx 2.563$ for a gaussian response. T_{eff} is the effective bit period which accounts for duty cycle distortion (DCD) at the transmitter and is calculated such that:

$$T_{eff} = \left(\frac{1}{B \cdot 10^6} - DCD \cdot 10^{-12}\right) \cdot 10^{12} \tag{2.19}$$

B is the signaling rate.

The ISI penalty can also be approximated to:

$$P_{isi} = 10\log_{10}\left(\frac{1}{1 - 1.425e^{-1.28\left(\frac{T}{T_c}\right)^2}}\right) \tag{2.20}$$

This equation is accurate to within 0.3dB for ISI penalties up to 5dB and up to 1dB for penalties less than 20dB.

2.5.3 Power Penalty due to Mode Partition Noise

In this section the penalty due to mode partition noise is defined as [42],[43]:

$$P_{mpn} = \frac{1}{\sqrt{1 - \left(Q \cdot \sigma_{mpn}\right)^2}} \tag{2.21}$$

Generally, the Q factor, is a function of the SNR, which provides a description of receiver performance. For a given Q we can approximate the error rate for a given link such that [5],[44]:

$$\text{BER} = \int_Q^{\infty} \frac{1}{\sqrt{2\pi}} e^{-\frac{x^2}{2}} dx \tag{2.22}$$

The standard deviation due to MPN is defines as:

$$\sigma_{mpn} = \frac{k_{OMA}}{\sqrt{2}} \cdot \left(1 - e^{-\left(\pi B_{eff} L \sigma_\lambda \sqrt{D_1^2 + D_2^2}\right)^2}\right) \tag{2.23}$$

Where, k_{OMA} is the mode partition factor between 0 and 1 and $B_{eff} = 1/T_{eff}$.

2.5.4 Power Penalty due to Relative Intensity Noise

The final noise term due to quantum laser noise is the relative intensity noise, defined as[42],[43]:

$$P_{RIN} = 10 \log_{10} \frac{1}{\sqrt{1 - \left(\frac{Q\sigma_{RIN}}{ISI_r}\right)}} \tag{2.24}$$

The variance due to RIN is defined as:

$$\sigma_{RIN}^2 = \frac{k_{RIN} \cdot 10^6}{\sqrt{\left(\frac{1}{BW_{me}}\right)^2 + \left(\frac{1}{BW_{cd}}\right)^2 + \left(\frac{0.477}{BW_{test}}\right) \cdot 10^{-\frac{RIN_{OMA}}{10}}}} \tag{2.25}$$

Here, k_{RIN} is a scaling factor, for 10G and 25G links $k_{RIN} = 0.75$.

2.5.5 Power Penalty due to Fiber Attenuation

Finally, the attenuation due to optical fiber is calculated as [43]:

$$\text{Att (dB)} = L\frac{R_\lambda}{C_\lambda}\left[\left(\frac{1}{9.4 \cdot 10^{-4} \cdot \lambda_C}\right) + 1.05\right] \tag{2.26}$$

Here, R_λ is the measured cable attenuation in dB/km while $C_\lambda = 3.5\ dB/km$ for wavelengths less than 1000nm.

2.6 Bit Error Rate Estimation

In a communication system, the number of errors received over a stream of data is commonly affected by noise, interference or distortion. At the received side, the sample value *I* will fluctuate from the average bit value I_1 or I_0. In electronics, a decision circuit compares the sampled value with a threshold value I_D which then decides whether the received bit is a 1 or a 0. An error occurs when this decision circuit is unable to correctly differentiate between a 1 or 0 level due to receiver noise. Therefore, the bit error is defined as [5]:

$$\text{BER} = p(1)P(0/1) + p(0)P(1/0) \tag{2.27}$$

Where $p(0)$ and $p(1)$ are the probabilities of receiving a 0 and 1 respectively. $P(0/1)$ is the probability of deciding a 0 when a 1 is received and $P(1/0)$ is the probability of deciding a 1 when a 0 is received. In PAM-2 systems the probability of 1's and 0's are assumed to be equally likely and therefore [5]:

$$\text{BER} = \frac{1}{2}[P(0/1) + P(1/0)] \tag{2.28}$$

If we assume sources such as shot and thermal noise from the photodetector to have a Gaussian probability density function with a standard deviation of σ_1 and σ_0 such that they encapsulate all noise sources in the system, therefore:

$$P(0/1) = \frac{1}{\sigma_1\sqrt{2\pi}}\int_{-\infty}^{I_D} e^{-\frac{(I-I_1)^2}{2\sigma_1^2}}\,dI = \frac{1}{2}\text{erfc}\left(\frac{I_1 - I_D}{\sigma_1\sqrt{2}}\right) \tag{2.29}$$

$$P(1/0) = \frac{1}{\sigma_0\sqrt{2\pi}}\int_{I_D}^{\infty} e^{-\frac{(I-I_0)^2}{2\sigma_0^2}}\,dI = \frac{1}{2}\text{erfc}\left(\frac{I_D - I_0}{\sigma_0\sqrt{2}}\right) \tag{2.30}$$

The error function is defined as:

$$erfc(x) = \frac{2}{\sqrt{\pi}}\int_{x}^{\infty} e^{-y^2}\,dy \tag{2.31}$$

And now the bit error rate in (5.18) can be defined as:

$$\text{BER} = \frac{1}{4}\left[\text{erfc}\left(\frac{I_1 - I_D}{\sigma_1\sqrt{2}}\right) + \text{erfc}\left(\frac{I_D - I_0}{\sigma_0\sqrt{2}}\right)\right] \tag{2.32}$$

Here we see that the bit error ratio is in fact dependent on the decision threshold. While a decision threshold at the midpoint between I_1 and I_0 is possible, it is only optimum when

thermal noise dominates. For real systems where the laser and photodiode shot noise is level dependent the optimum decision threshold is specified by:

$$I_D = \frac{\sigma_1 I_1 + \sigma_1 I_0}{\sigma_0 + \sigma_1} \tag{2.33}$$

Assuming an optimum decision threshold I_D, the bit error rate can also be defined by the Q factor, such that:

$$\text{BER} = \frac{1}{2}\text{erfc}\left(\frac{Q}{\sqrt{2}}\right) \approx \frac{e^{-\frac{Q^2}{2}}}{Q\sqrt{2\pi}} \tag{2.34}$$

Here, Q is defined as [5]:

$$Q = \frac{I_1 - I_0}{\sigma_1 + \sigma_0} \tag{2.35}$$

Here we will calculate noise sources such that the total noise current variance can be expressed as:

$$\sigma_i^2 = \frac{4k_B T F_N}{R_L}\Delta f + 2qI_i\Delta f + RIN \cdot I_i^2 \Delta f \tag{2.36}$$

Where $k_B$is the Boltzmann constant, T is temperature in Kelvin, F_N is the noise figure of the amplifier, R_L is the load resistance, RIN is the average RIN spectral density. The optical power can be calculated if the responsivity, $\Re$, at the wavelength of interest is known such that:

$$P_{optical} = \frac{I_i}{\Re} \tag{2.37}$$

2.6.1 PAM-4 Systems

The previous section dealt with PAM-2 systems. For a generic PAM link with M-levels, a generalized set of equations will be described.

While a PAM-2 system encoded one bit into each level, higher order modulation formats such as PAM-4, are able to encode more than one, increasing spectral efficiency. As before, the ISI penalty can be rewritten such that the worst-case ISI in a system can be expressed as [44]-[47]:

$$P_{ISI}(dB) = 10 * log_{10}\left(\frac{1}{1 - E_m}\right) \tag{2.38}$$

Where E_m is the worst-case relative eye closure which can be approximated to:

$$E_{m,OOK} = 1.425 \exp\left(-1.28\left(\frac{T_{eff}}{T_c}\right)^2\right) \tag{2.39}$$

Again, here, T_{eff} is the bit period and T_c is the 10-90% channel rise time. Extending this ISI penalty to PAM-4, for the same rise time and symbol rate, the eye diagram for a PAM-4 system will be twice as big as in the OOK case and therefore can be written as [44]:

$$E_{m,PAM-4} = 2.85 \exp\left(-1.28\left(\frac{T_{eff}}{T_c}\right)^2\right) \tag{2.40}$$

To calculate BER in PAM-M signals we first calculate the symbol error rate or SER. Assuming that all symbols are equally probable the SER can be calculated by summing the probability of an error and diving by the number of levels [45]:

$$\text{SER} = \frac{1}{M}\sum_{i=0}^{M-1}\sum_{j=0}^{M-1} P(i|j) \tag{2.41}$$

Where $P(i|j)$ is the probability of receiving a symbol j when i was transmitted. Assuming Gaussian noise, the probability $P(i|j)$ can be described as:

$$P(i|j) = \frac{1}{2}erfc\left(\frac{I_{th,j} - I_i}{\sigma_i\sqrt{2}}\right) - \frac{1}{2}erfc\left(\frac{I_{th,j+1} - I_i}{\sigma_i\sqrt{2}}\right) \tag{2.42}$$

Such that $I_{th,j}$ is again the threshold current where $I_{th,0} = -\infty$ and $I_{th,M} = +\infty$, I_i is the photocurrent at symbol i, σ_i is the noise RMS current at symbol i. Assuming that all symbol levels are equally spaced and noise sources are thermally dominated such that $\sigma_i = \sigma$ and $I_{avg} = \frac{\sum I_i}{i+1}$, the SER can be written as:

$$\text{SER} = \frac{M-1}{M}\text{erfc}\left(\frac{I_{avg}}{(M-1)\sqrt{2}\sigma}\right) \tag{2.43}$$

The approximate BER can be then calculated to be [48]:

$$BER \approx d_{avg}\frac{SER}{\log_2 M} \tag{2.44}$$

Here, d_{avg} is the Hamming distance. If Gray labeling is used $d_{avg} = 1$, otherwise [48]:

$$d_{avg} = \sum_{k=0}^{-1+\log_2(M)} \frac{(-\text{k} + \log_2 M)2^k}{M-1} = 2 - \frac{\log_2 M}{M-1} \tag{2.45}$$

CHAPTER 3

SINGLE MODE VCSEL MODEL

The vertical cavity surface emitting laser is a low-cost light source with various properties such as a low threshold current, and wafer level testing which gives it an edge over conventional edge emitting lasers in certain application. VCSELs like the one shown in Fig. 3.1 are made by placing a thin semiconductor of high optical gain such a quantum well between two highly reflective mirrors [49]. Unlike edge emitter the optical cavity is formed perpendicular to the plane of the wafer. High reflectivity mirrors are required to overcome the rather short gain region in the cavity. Therefore, distributed Bragg reflectors parallel to the wafer surface are used. These mirrors consist of alternating quarter wavelength high and low refractive indices, and capable of achieving reflectivities above 99%. Current is confined to the center of the inner cavity through either etching of the top mirror, ion implantation, or selective lateral oxidation. These devices emit a circular light beam,

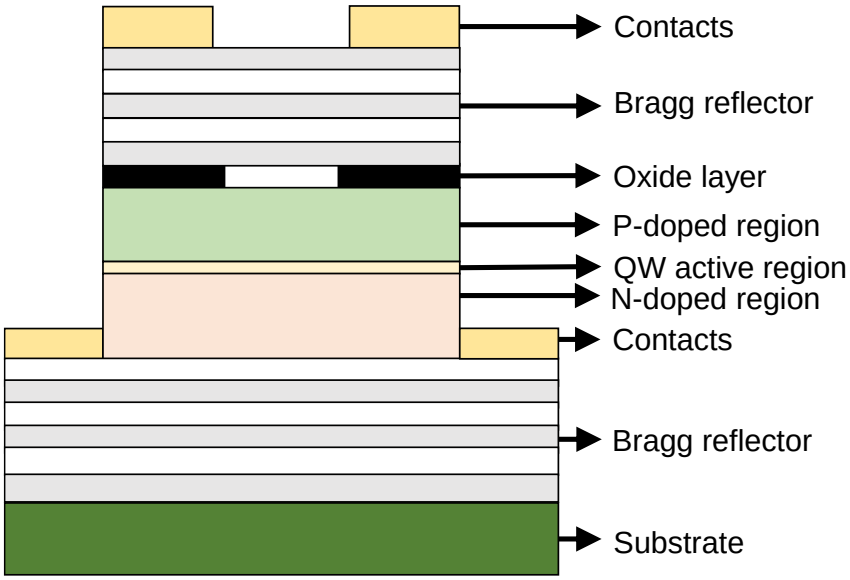

Figure 3. 1 Illustration of VCSEL structure

consuming less power and are capable of 2D array configurations [49]. The advantages over edge-emitters, specifically driven by its low cost, maturity, reliability in short reach data communications make VCSEL links a very enticing solution for next generation optical interconnects [49],[50].

Though the previous section was mainly aimed at understanding the general set of laser rate equations, there exist great interest in laser rate equations specifically aimed at modeling VCSEL dynamics. Fortunately, the general set of laser rate equations gets us very close. For the multimode case, it has been shown experimentally and theoretically, that index guided multimode VCSELs with highly overlapping transverse fields have uniform carrier and photon densities and exhibit a single resonance frequency [51]. Therefore, a single mode laser rate equation model is incredibly helpful in understanding the static and dynamic behavior of VCSELs. By fitting our simulations to experimental data, we can gain a great deal of understanding by describing the laser structure through physical laser parameters such as lifetimes and densities. These parameters can be used to optimize laser design and help us achieve higher speeds by optimizing laser bandwidth as well as reducing laser noise. This section will deal primarily with generating a set of single mode stochastic laser rate equations, along with a parameter extraction methodology to capture multimode VCSEL phenomena.

3.1 VCSEL Rate Equation

Initial efforts into laser modeling are based on laser rate equations first developed by P.V. Mena [21]. This set of equations relates the number of photons, S and the number of carriers, N:

$$\frac{dN}{dt} = \frac{\eta_i(I - I_{off})}{q} - \frac{N}{\tau_n} - GS + F_N(t) \tag{3.1}$$

$$\frac{dS}{dt} = -\frac{S}{\tau_p} + \frac{\beta N}{\tau_n} + GS + F_P(t) \tag{3.2}$$

where, η_i is the injection efficiency, τ_n the carrier lifetime, τ_p the photon lifetime, β is the spontaneous emission coefficient, I_{off} represents the threshold current, I represents the injection current, N_o represents the carrier transparency number. $F_N(t)$ and $F_P(t)$ are Langevin noise sources account for RIN. It should be emphasized that (3.1) and (3.2) only account for the intrinsic response of the laser, therefore laser parasitics must be added. In this section, we model the optical gain G as a linear function of the carrier density [23],[52].

$$G = \frac{g_{lin}(N - N_0)}{1 + \epsilon S} \tag{3.3}$$

where g_{lin} is the linear gain coefficient, ϵ is the gain compression coefficient and N_o the carrier density at transparency. Here, the $1/(1 + \epsilon S)$ term in the equation represents the phenomenological characterization of the nonlinear damping caused by such effects as carrier heating and spectral hole burning.

Though more complex models have been presented in literature to account for more advanced structures, we believe this model can capture the most important characteristics of directly modulated VCSELs.

Whereas equations 1 and 2 only account for the intrinsic response of the laser. Bias dependent VCSEL parasitics are accounted through a third differential equation, which filters the effective drive current I_{drive} by using a low pass filter of bandwidth ω_{3dB}.

$$\frac{dI}{dt} = \omega_{3dB}(I_{drive} - I) \tag{3.4}$$

Thermal effects, like the roll-over in the LI curve, have not been incorporated. However thermal effects can be incorporated by using a fourth differential equation that captures the junction temperature which is dependent on the drive current and ambient temperature [21],[53].

3.2 Linear Representation of VCSEL Rate Equations

Though one can solve the VCSEL rate equations numerically and tune laser parameters until achieving the desired output, the numerical computation required to fit experimentally measured data, such as the small signal frequency response and RIN spectra, to the set of laser rate equations would be difficult. To accelerate parameter extraction, we must first linearize VCSEL dynamics. Two common methods exist, these assume small perturbations to the system, such as the modulation current. A system of linearized rate equations can be found by performing an expansion in the form of $x(t) = x_0 + dx(t)$ for all dynamic variables and neglecting all nonlinear terms. The second method, and the one used here assumes that dynamic changes in the carrier and photon reservoirs at their respective steady state values are small. With this assumption in mind, we take the differential of both rate equations and take $I, N, S,$ and G as dynamic variables. Note that in this section we did not set $F_N(t)$ and $F_P(t)$ as dynamic variables since for now we are interested in the magnitude response rather than any statistical noise properties of the laser. Here we will use (3.1) and (3.2) and apply the differential method described in [23]:

$$d\left[\frac{dN}{dt}\right] = \frac{\eta_i I}{q} dI - \frac{1}{\tau_n} dN - GdS - SdG \tag{3.5}$$

$$d\left[\frac{dS}{dt}\right] = -\frac{1}{\tau_p}dS + \frac{\beta}{\tau_n}dN + GdS + SdG \tag{3.6}$$

The term SdG can be further expanded since it is affected by both carrier and photon variations:

$$SdG = S(adN + a_P dS) \tag{3.7}$$

$$a = \frac{dG}{dN} = \frac{g_{lin}}{1 + \epsilon S} \tag{3.8}$$

$$a_p = -\frac{dG}{dS} = \frac{d(g_{lin}(N - N_0)(1 + \epsilon S)^{-1})}{dS} = \frac{\epsilon G}{1 + \epsilon S} \tag{3.9}$$

By substituting (3.7) into (3.5) and (3.6) and collecting like terms we get:

$$d\left[\frac{dN}{dt}\right] = \frac{\eta_i I}{q}dI - \left(\frac{1}{\tau_n} + Sa\right)dN - \left(G - Sa_p\right)dS \tag{3.10}$$

$$d\left[\frac{dS}{dt}\right] = \left(\frac{\beta}{\tau_n} + Sa\right)dN - \left(\frac{1}{\tau_p} + G + Sa_p\right)dS \tag{3.11}$$

These can be further represented as rate coefficients:

$$\gamma_{NN} = \frac{1}{\tau_n} + Sa \tag{3.12}$$

$$\gamma_{NS} = G - Sa_p \tag{3.13}$$

$$\gamma_{SN} = \frac{\beta}{\tau_n} + Sa \tag{3.14}$$

$$\gamma_{SS} = \frac{1}{\tau_p} + G + Sa_p \tag{3.15}$$

Here the rate coefficients γ_{NN}, γ_{NS}, γ_{SN}, and γ_{SS} correspond to the differential carrier lifetime, the gain, the differential lifetime of the carriers, and the effective photon lifetime, respectively. Furthermore, the introduction of these rate coefficients allows us to represent the differential rate equations in a more compact form [23],[52]:

$$\frac{d}{dt}\begin{bmatrix} dN \\ dS \end{bmatrix} = \begin{bmatrix} -\gamma_{NN} & -\gamma_{NS} \\ \gamma_{SN} & -\gamma_{SS} \end{bmatrix}\begin{bmatrix} dN \\ dS \end{bmatrix} + \frac{\eta_i}{q}\begin{bmatrix} dI \\ 0 \end{bmatrix} \tag{3.16}$$

To obtain the small signal frequency response, first we assume that the system, specifically *I* is driven by a sinusoid. Assuming sinusoid excitation we can transform to the frequency domain through these solutions:

$$dI(t) = I_1 e^{j\omega t} \tag{3.17}$$

$$dN(t) = N_1 e^{j\omega t} \tag{3.18}$$

$$dS(t) = S_1 e^{j\omega t} \tag{3.19}$$

$$\frac{d}{dt} \leftrightarrow j\omega \tag{3.20}$$

We therefore obtain:

$$\begin{bmatrix} \gamma_{NN} + j\omega & \gamma_{NS} \\ -\gamma_{SN} & \gamma_{SS} + j\omega \end{bmatrix}\begin{bmatrix} N_1 \\ S_1 \end{bmatrix} = \frac{\eta_i I_1}{q}\begin{bmatrix} 1 \\ 0 \end{bmatrix} \tag{3.21}$$

Here the determinant of the matrix is given by:

$$\Delta = \begin{vmatrix} \gamma_{NN} + j\omega & \gamma_{NS} \\ -\gamma_{SN} & \gamma_{SS} + j\omega \end{vmatrix} \tag{3.22}$$

Through Cramer's rule we can obtain the small signal photon transfer function with respect to the modulation current:

$$S = \frac{\eta_i I_1}{q}\frac{1}{\Delta}\begin{vmatrix} \gamma_{NN} + j\omega & 1 \\ -\gamma_{SN} & 0 \end{vmatrix} = \frac{\eta_i I_1}{q}\frac{\gamma_{SN}}{\omega_R^2} H_{laser}(\omega) \tag{3.23}$$

3.2.1 Linearized Small Signal Frequency Response

As before, the intrinsic small signal frequency response of the laser can be characterized by the resonance frequency ω_r and damping γ [52]:

$$H_{laser}(\omega) = \frac{\omega_R^2}{\omega_R^2 - \omega^2 + j\gamma\omega} \tag{3.24}$$

The resonance frequency and damping factor can be expressed in terms of laser parameters:

$$\omega_R^2 \approx \frac{S}{\tau_p}\frac{G_o}{1 + \epsilon S} \tag{3.25}$$

$$\gamma = 4\pi^2\tau_p\left[1 + \frac{\epsilon(N - N_0)}{1 + \epsilon S}\right]f_R^2 + \frac{1}{\tau_n} + \frac{\beta N}{\tau_n S} \tag{3.26}$$

Equations (3.24) - (3.26) can now be used to fully characterize the VCSEL's intrinsic response using laser parameters. For simplicity, we will sometimes switch between angular frequency, ω, and linear frequency f, where $\omega = 2\pi f$.

In order for complete dynamic characterization, which include laser parasitics, parameter extraction requires the decoupling of extrinsic and intrinsic bandwidth

limitations. The subtraction method may be used to calculate the intrinsic response of the laser. A more direct approach found here [54] was used where parasitics can be modeled as an RC circuit. This allowed us to extract parasitics directly from the small signal response measurements that lacked S_{11} data. It was also capable of extracting bias dependent parasitics, which was experimentally validated [55]. As before the total response of the system can be expressed in terms of the intrinsic and extrinsic (intrinsic + parasitic) response of the laser:

$$H_{total}(\omega) = H_{laser}(\omega)H_{parasitic}(\omega) \tag{3.27}$$

$$H_{parasitic}(\omega) = \frac{\omega_p}{\omega_p + j\omega} \tag{3.28}$$

Where $H_{parasitic}(\omega)$ has been defined as a simple lowpass filter. More complex parasitic circuits may be chosen on a case-by-case basis, depending on the experimental setup and its parasitics.

3.2.2 Relative Intensity Noise

Up until now, we have yet to formulate a linear representation of the dynamical properties of laser noise. Assuming a constant drive current such that $dI = 0$, and introducing the Langevin noise sources as dynamic variables the differential rate equations can be described as:

$$d\left[\frac{dN}{dt}\right] = -\gamma_{NN}dN - \gamma_{NS}dS + F_N(t) \tag{3.29}$$

$$d\left[\frac{dS}{dt}\right] = \gamma_{SN}dN - \gamma_{SS}dS + F_P(t) \tag{3.30}$$

And can be represented in matrix form as before:

$$\frac{d}{dt}\begin{bmatrix} dN \\ dS \end{bmatrix} = \begin{bmatrix} -\gamma_{NN} & -\gamma_{NS} \\ \gamma_{SN} & -\gamma_{SS} \end{bmatrix}\begin{bmatrix} dN \\ dS \end{bmatrix} + \begin{bmatrix} F_N(t) \\ F_S(t) \end{bmatrix} \tag{3.31}$$

Where $F_N(t)$, and $F_S(t)$ are now considered the driving forces of the system. Transforming (3.31) to the frequency domain gives us:

$$\begin{bmatrix} \gamma_{NN} + j\omega & \gamma_{NS} \\ -\gamma_{SN} & \gamma_{SS} + j\omega \end{bmatrix}\begin{bmatrix} N_1 \\ S_1 \end{bmatrix} = \begin{bmatrix} F_N \\ F_S \end{bmatrix} \tag{3.32}$$

Using a similar treatment as the previous section we get:

$$S_1 = \frac{H(\omega)}{\omega_R^2}\begin{vmatrix} \gamma_{NN} + j\omega & F_N \\ -\gamma_{SN} & F_S \end{vmatrix} \tag{3.33}$$

We can define the photon spectral density as:

$$\boldsymbol{S}_S(\omega) = \frac{1}{2\pi}\int \langle S_1(\omega) S_1(\omega')^* \rangle d\omega' \tag{3.34}$$

Which allows us to obtain an expression of the photon spectral density in terms of rate equation parameters:

$$\boldsymbol{S}_S(\omega) = \frac{|H(\omega)|^2}{\omega_R^4}[(\gamma_{NN}^2 + \omega^2)\langle F_S F_S \rangle + 2\gamma_{NN}\gamma_{SN}\langle F_S F_N \rangle + \gamma_{SN}^2 \langle F_N F_N \rangle] \tag{3.35}$$

Where the parameters γ_{NN}, and γ_{SN} are rate coefficients previously derived in terms of laser parameters in (3.12)-(3.15). Here, Langevin noise source spectral densities are defined as:

$$\langle F_i F_j \rangle = \frac{1}{2\pi} \int \langle F_i(\omega) F_j(\omega')^* \rangle d\omega' \tag{3.36}$$

We can now define RIN as:

$$RIN\left(\frac{dB}{Hz}\right) = 10 \log_{10}\left(2\frac{\boldsymbol{S}_S(\omega)}{S^2}\right) \tag{3.37}$$

By using the formulation described in section 2.3 we can describe the noise correlations for this set of rate equations:

$$\langle F_S F_S \rangle = \frac{S}{\tau_P} + 2 * \frac{\beta NS}{\tau_N} + \frac{\beta N}{\tau_N} - \frac{G_o(N - N_o)}{1 + \epsilon S} S \tag{3.38}$$

$$\langle F_S F_N \rangle = -\left(2 * \frac{\beta NS}{\tau_N} + \frac{\beta N}{\tau_N} - \frac{G_o(N - N_o)}{1 + \epsilon S} S\right) \tag{3.39}$$

$$\langle F_N F_N \rangle = 2 * \frac{\beta NS}{\tau_N} + \frac{\beta N}{\tau_N} - \frac{G_o(N - N_o)}{1 + \epsilon S} S + \frac{\eta_i\left(I + I_{off}\right)}{q} \tag{3.40}$$

It should be noted that the RIN spectrum is directly related to the intrinsic bandwidth of the laser. Therefore, parameter extraction using bandwidth and RIN characteristic must be an iterative process.

3.3 Joint Parameter Extraction

Laser rate equation-based modelling and the associated parameter extraction have been studied in the past for a range of operating conditions [56]-[59]. However, to the best of our knowledge, there was no parameter extraction methodology that simultaneously captured the spectral characteristics of the frequency response $\left(H(\omega)\right)$ and RIN $\left(RIN(\omega)\right)$

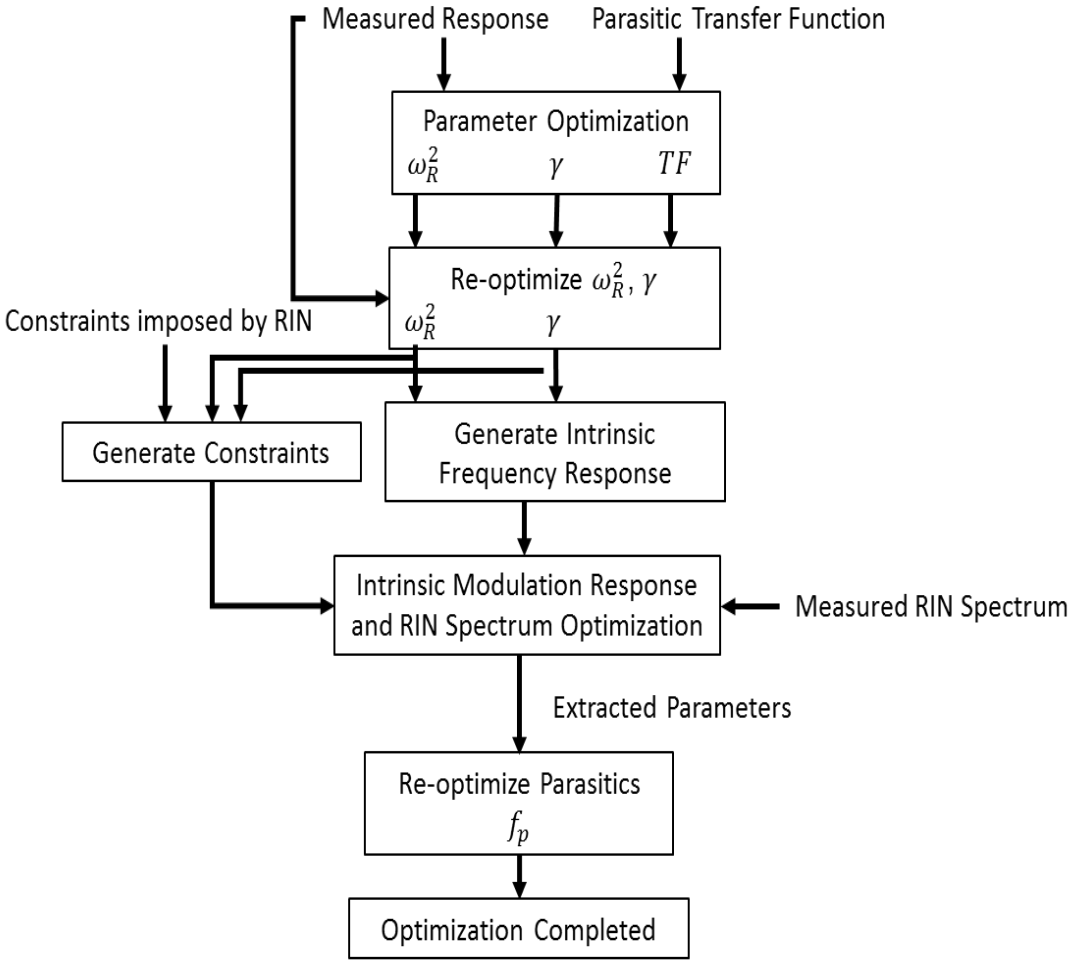

Figure 3. 2 Joint Parameter Extraction Block Diagram

over multiple drive currents for VCSELs or any other directly modulated laser (DML). Capturing this is critical for ensuring consistency between experiments and simulation environments, especially for the large voltage/current swings of PAM-4 modulation. Further it is also necessary to optimize VCSEL performance and minimize limitations in various laser designs. In this section, we demonstrate a parameter extraction technique that is capable of accurately extracting laser rate equation parameters from experimental data. We employ gradient decent algorithm along with a linearized representation of the laser rate equations to search for viable solutions and extract a set of solutions which fit both the

experimental $RIN(\omega)$ and $H(\omega)$ data sets. This allows for accurate simulation of both $H(\omega)$ and $RIN(\omega)$ over a wide range of drive currents using a single set of parameters.

As shown, we first match the analytical expression in (3.24) to the measured frequency response by minimizing the mean squared error in two sub steps: optimization, and re-optimization (fine tuning). Note that each bias dependent frequency response is optimized independently and in the order of increasing bias currents making sure that, the extracted parasitic frequency ω_p increases with the bias current. Through this first step we are also able to separate the intrinsic frequency response of the laser from the extrinsic frequency response which includes the parasitic circuit. After the initial extraction we now have full knowledge of ω_R, γ and ω_p for each bias current, Fig 3.3b. If no RIN data is available, then the extraction is complete. The damping, γ, can be fitted given $\gamma = Kf_R^2 + \gamma_0$, where K is the damping factor, f_R^2 is the resonance frequency in Hz, and γ_0 is the damping offset [60]. Results are shown in Fig. 3.3c. Extracted values using this process are shown in Table 3.1 for VCSEL A.

Table 3. 1 VCSEL Parameters

Description	**VCSEL A**	**VCSEL B**	**VCSEL C**
Injection Efficiency, η_i	0.57	0.81	0.26
Spontaneous Emission Factor, β	$1x10^{-4}$	$1x10^{-3}$	$2.1x10^{-2}$
Carrier Lifetime (ns), τ_n	5	2.12	0.99
Photon Lifetime (ps), τ_p	4.09	5.13	3.02
Gain (s^{-1}), G_o	$10.31x10^5$	$3.69x10^5$	$11.9x10^5$
Gain Saturation Factor, ϵ	$4.18x10^{-6}$	$0.11x10^{-6}$	$2.81x10^{-6}$
Carrier Transparency Number, N_o	$1x10^5$	$1.96x10^4$	$1.7x10^4$

For data that includes both bandwidth and RIN measurements we iteratively match the simulated intrinsic frequency response to the analytical intrinsic frequency response obtained from the first step while simultaneously matching the simulated RIN spectra to the measured RIN spectra. A single joint cost function is used in this step, where all measured frequency response curves RIN spectra are additively considered in arriving at a single error value for optimization. Reasonable start values and bounds are assumed for the parameters. Twenty-five random starting sets of laser parameters are generated and

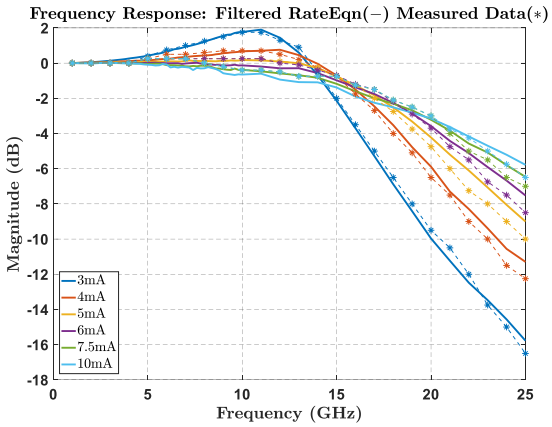

(a)

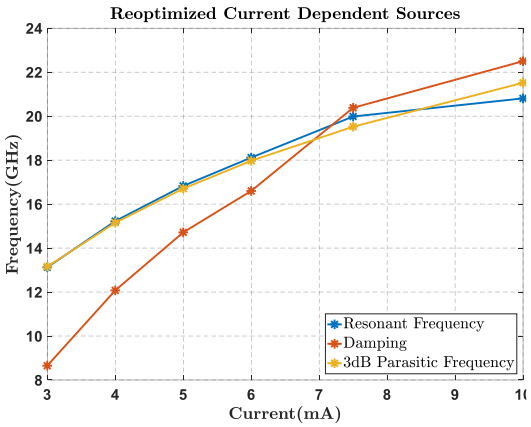

(b)

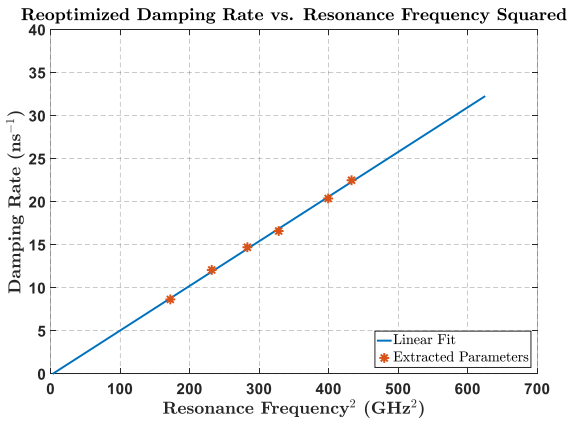

(c)

Figure 3. 3 (a) Matching VCSEL A frequency response with VCSEL rate equation parameters using parasitic filter extracted from optimization. The extracted rate equation parameters together with the extracted parasitic filter provide a good match between the modelled and measured frequency responses. (b) Optimized current dependent sources. (c) Linear fit of γ with ω_R^2 after fine tuning.

iteratively optimized, where the set of values with the lowest associated cost is considered a near global minimum solution. Once the laser rate parameters are extracted the final simulated RIN spectrum and the simulated intrinsic frequency response is now generated directly from the laser rate equations. We later verify our extracted values by numerically computing the magnitude response from the laser rate equations by using sinusoidal tones as the input. Parameter extraction for RIN is then verified by numerically solving the stochastic laser equation using the Euler approach.

The extraction method was applied on 4 different VCSELs:

- VCSEL A is a 7micron 850nm InGaAs QW VCSEL designed for 25-28Gbps operation with a -3dB of ~18GHz at 7.5mA [61]
- VCSEL B is 9micron 850nm oxide confined strained InGaAs QW VCSEL intended for short reach high speed communications [62]
- VCSEL C is a modified version of VCSEL B, here RIN is artificially increased by 30dB in order to better view level dependent effects
- VCSEL D is a 3.1micron thin oxide aperture InGaAs QW VCSEL and a 15GHz 3dB bandwidth at a bias of only 2.1mA [63]

In this set of data, RIN data was available for VCSEL B and C. Figures 3.3a and 3.4a show agreement between simulated and measured magnitude response for both VCSEL A and B. As previously stated, our parameter extraction methodology is capable of capturing the small signal frequency response over a large bias current range and over a wide frequency range. For VCSEL A the magnitude response was fitted from 3mA to 10mA and matched

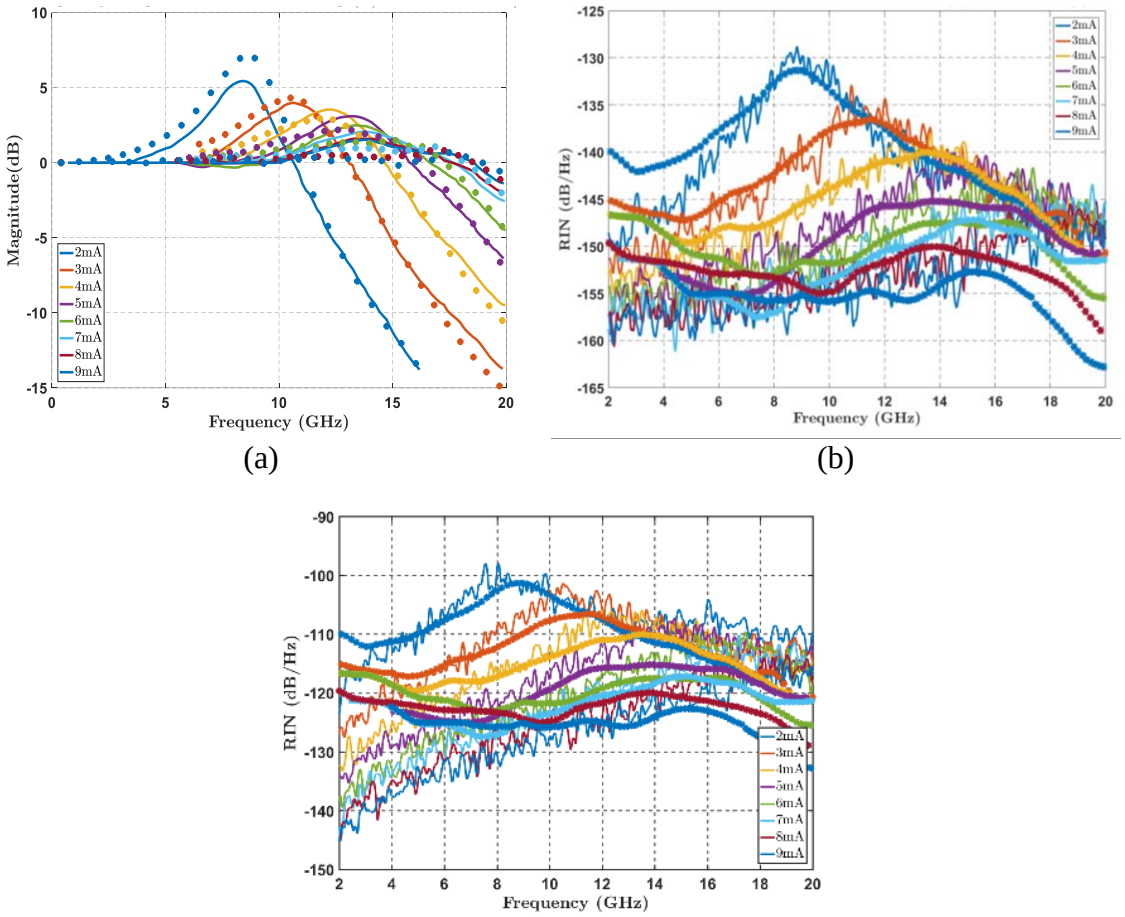

(a) (b)

(c)

Figure 3. 4 (a) Matching VCSEL B frequency response with VCSEL rate equation parameters using parasitic filter extracted from optimization. Results show excellent agreement over a wide range of bias points. (b) VCSEL rate equation RIN spectra (-) using parameters shown in Table 1 and measured data from VCSEL B (∗). It should be noted that the experimental RIN is higher at lower frequencies due to mode partition noise (MPN) which has not been accounted for in this model. Frequencies above 16GHz also do match due to the hardware limitations (c) VCSEL rate equation RIN spectra (-) using parameters shown in Table 1 and shifted measured data from VCSEL B (∗).

extremely well using a single set of laser parameters shown in Table 3.1. Figures 3.3b shows the expected increasing resonance frequency, damping with increasing current. Figures 3.3b also shows the bias dependent parasitics, primarily caused by heating of the parasitic circuit elements as current increases, but which is rarely modeled in VCSEL rate equations. Deviations from the measured values can be attributed to both experimental

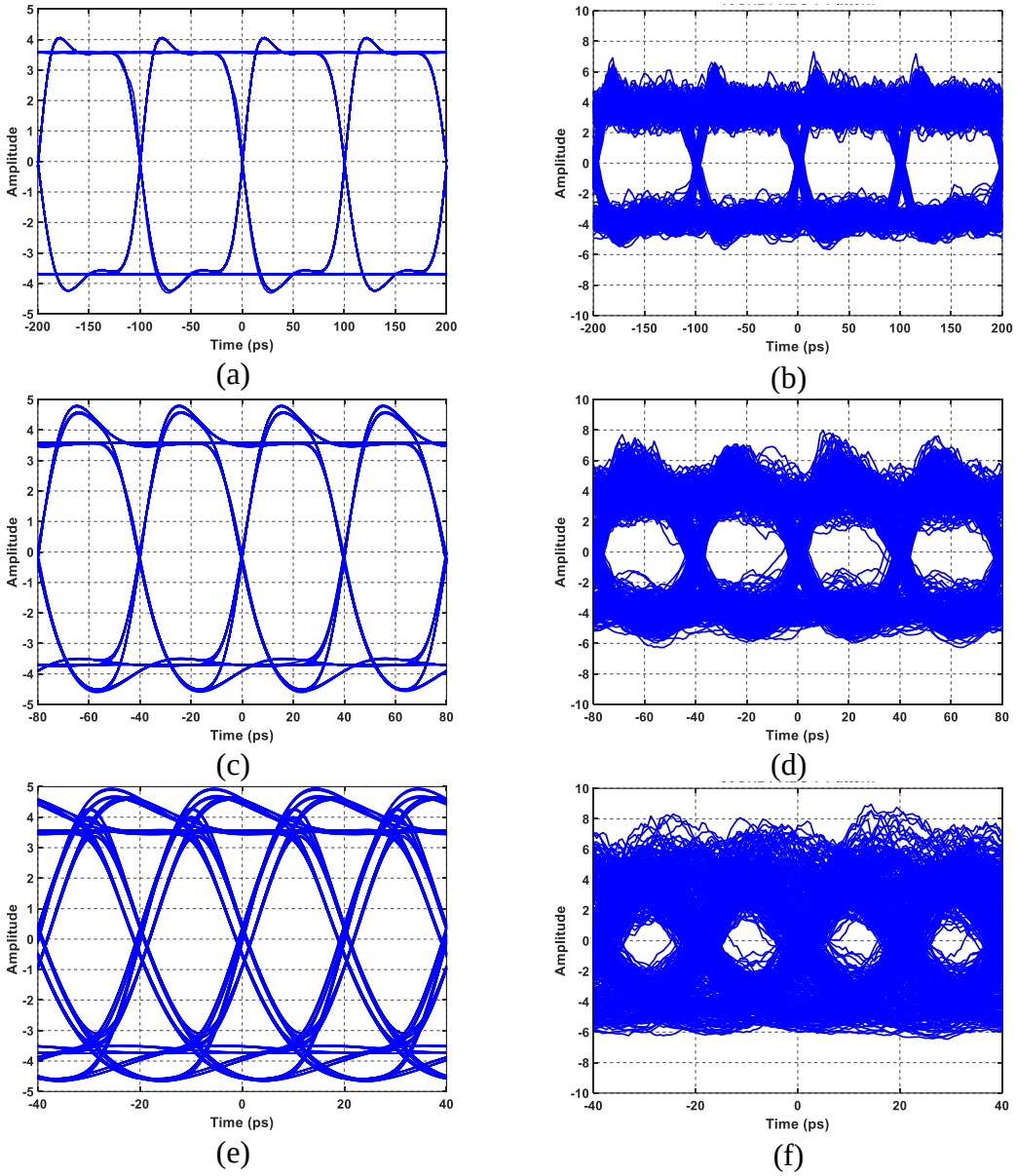

Figure 3. 5 Simulated non-stochastic (a,c,e) and corresponding stochastic (b,d,f) laser rate equations of a (a,b)10G PRBS pattern, (c,d)25G PRBS pattern, and (e,f)50G PRBS pattern. Non-stochastic eye diagrams show ISI effects as we move toward high speeds. For the stochastic case, though the average bit levels 0 and 1 stay constant, it is swamped by noise at higher bit rates. Though Fig. 3.4e shows symmetric average bit levels 0 and 1, the effects of level dependent RIN can be seen clearly seen in Fig 3.4f. Here we see bit level 1 having higher noise deviations than bit 0.

uncertainties, the lack of multiple modes and the simplistic view of the parasitic circuit. From figure 3.3c we can acquire the commonly used figure of merit, the k-parameter to be ~0.2ns. Figure 3.4b shows good agreement between simulated and experimentally measured RIN. It should be noted that the experimental RIN is higher at lower frequencies due to MPN which is not accounted for in this model. Frequencies above 16GHz also do not match due to the hardware limitations as noted here [62]. To easily view the bias dependent RIN in an eye diagram, the measured RIN data from VCSEL B was artificially shifted up by 30dB as shown in Fig 3.4c. Figure 3.5 includes the simulated non stochastic and stochastic VCSEL rate equations using parameters from VCSEL C. The non-stochastic rate equations clearly show that the ISI effects become evident as the VCSEL is driven faster. Since intensity noise is relative to the optical power there should be more noise experienced at higher levels. Most models simplistically add a constant average noise to the entire signal. However, as seen from the stochastics eye diagrams in Fig. 3.5 our model adds level-dependent noise. Parameter extraction results for VCSEL D are shown in Fig

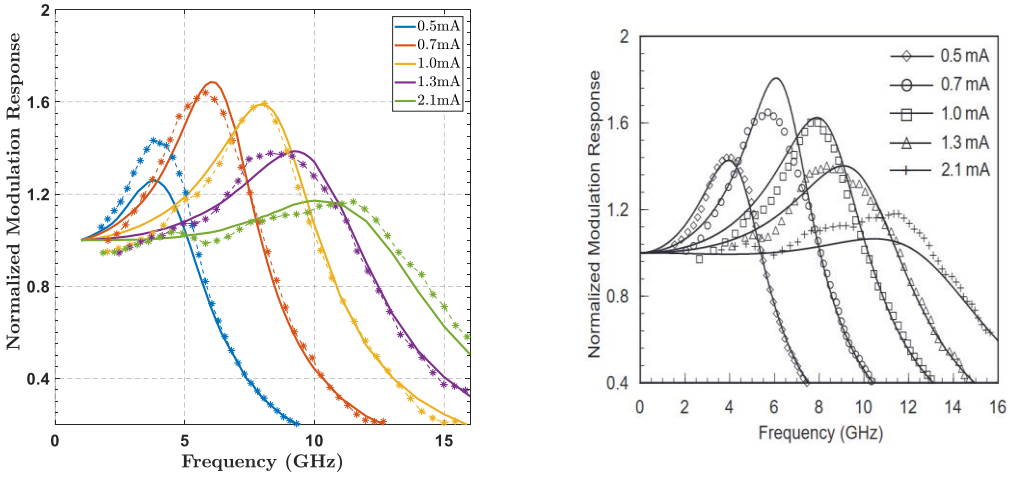

(a) (b)

Figure 3. 6 Parameter extraction results using (a) our method vs (b) method described in [53]

3.6a. Here we show that our parameter extraction methodology is just as effective at capturing the small signal frequency response over multiple bias currents as similar methods yet is also able to account for RIN.

3.4 Enhanced Parameter Extraction

While the previous section introduced our joint parameter extraction methodology, the method was capable of optimizing only a single cost function. While the additive sum of the mean squared error (MSE) of both RIN and modulation response can be used, it still required one to set weights and normalization factors. Depending on the data, the set of weight and normalization factors could greatly influence the fitting process. In the following sections, we begin by discussing single objective $H(\omega)$-only and $RIN(\omega)$-only parameter extraction approaches and their drawbacks. We demonstrate how parameter extraction using only experimental $H(\omega)$ leads to a poor match between the simulated and experimental RIN spectrum, while parameter extraction based on only $RIN(\omega)$ results in a poor match for the case of $H(\omega)$. We later demonstrate how multi-objective parameter extraction provides an acceptable trade-off by ensuring reasonably close matches between experiments and theory for both $H(\omega)$ and $RIN(\omega)$. Figure 3.7 shows the sequence of steps for our multi-objective approach, where the $H(\omega)$-only and $RIN(\omega)$-only approaches are the left and right branches of the flowchart. The experimental $H(\omega)$ and $RIN(\omega)$ employed in this section were presented in [62]. Parameter extraction results in multiple acceptable solutions that satisfy the parameter bounds as the cost function has multiple local minimums. Multi-objective optimization allows us to objectively select these minimums by sorting a diverse set of solutions which allows for good approximations between both

sets of data. Therefore, a multi-objective optimization process would be an extremely beneficial tool for parameter extraction. If successful, multiple sets of data, each describing a certain laser characteristic can be used to extract and validate laser performance.

Furthermore, here we will use laser parameters in terms of densities since they are more intuitive than numbers. Therefore, we will introduce the density rate equations along without multi objective algorithm in order to give meaningful results which can be used to

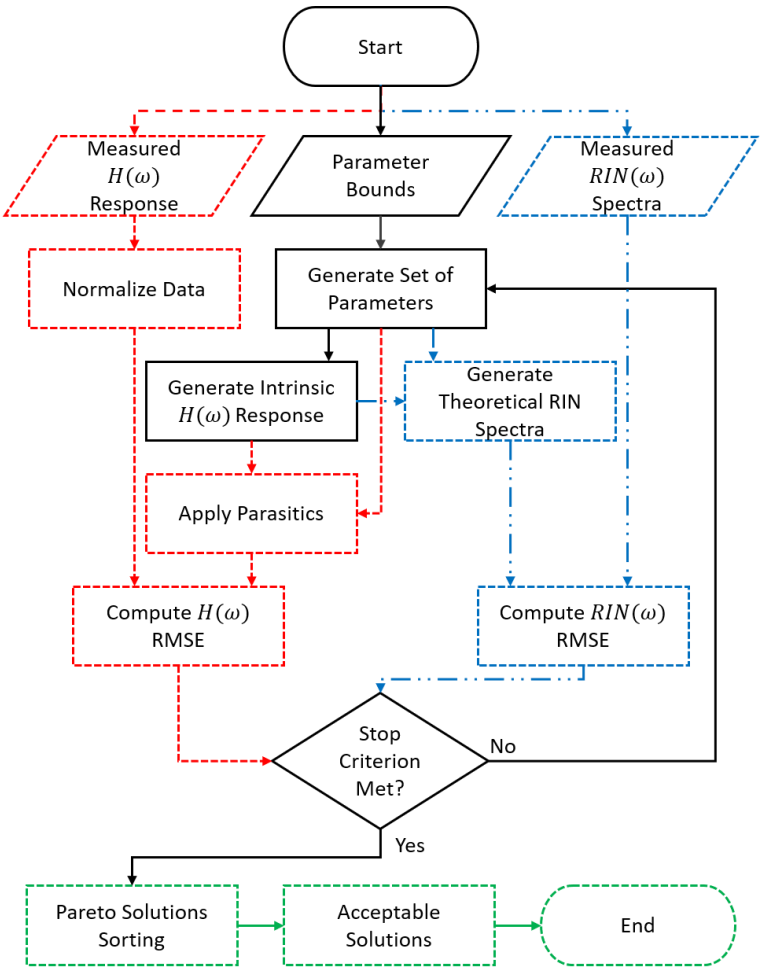

Figure 3. 7 Flowchart for parameter extraction using experimentally measured modulation response $H(\omega)$ and/or the RIN spectrum $RIN(\omega)$. $H(\omega)$-only parameter extraction can be computed by using only the $H(\omega)$ MSE. $RIN(\omega)$-only parameter extraction can be computed by using only the $RIN(\omega)$ MSE. Note that all blocks are needed for multi-objective parameter extraction

optimize laser design. The following equations in terms of N and S now represent the carrier and photon density, respectively.

$$\frac{dN}{dt} = \frac{\eta_i I}{qV} - \frac{N}{\tau_n} - GS + F_N(t) \tag{3.40}$$

$$\frac{dS}{dt} = -\frac{S}{\tau_p} + \Gamma\frac{\beta N}{\tau_n} + \Gamma GS + F_P(t) \tag{3.42}$$

Here we introduce a new variable, Γ, the confinement factor which is defined as the ratio of the active region volume V of the carrier reservoir to the mode volume V_p of the photon reservoir. Furthermore, we removed I_{off} in order to follow the conventional rate equation form of (2.1). In reality, I_{off} is not part of the standard rate equations since the threshold current arises implicitly from a DC solution of the rate equations.

We again model the optical gain G as a linear function of the carrier density.

$$G = \frac{g(N - N_0)}{1 + \epsilon S} \tag{3.43}$$

where g is the linear gain coefficient, ϵ is the gain compression coefficient and N_o the carrier density at transparency.

Here we introduce two new terms to quantify gain. Material and modal gain which are defined as:

$$Material\ Gain = \frac{G}{v_g} \tag{3.44}$$

$$\text{Modal Gain} = \Gamma * \text{Material Gain} \tag{3.45}$$

where v_g is the group velocity.

Bias dependent VCSEL parasitics are accounted through a third differential equation, as before by using (3.4).

The linearized intrinsic small signal frequency response $H_{laser}(\omega)$ is then characterized by the resonance frequency ω_R and damping γ, which are defined in terms of laser rate equation parameters.

$$H_{laser}(\omega) = \frac{\omega_R^2}{\omega_R^2 - \omega^2 + j\gamma\omega} \tag{3.46}$$

where:

$$\omega_R^2 \approx \frac{S}{\tau_p}\frac{g_o}{1+\epsilon S} \tag{3.47}$$

$$\gamma = \tau_p\left[1 + \frac{\Gamma\epsilon(N-N_o)}{1+\epsilon S}\right]\omega_R^2 + \frac{1}{\tau_n} + \frac{\Gamma\beta N}{\tau_n S} \tag{3.48}$$

We again incorporate the effects of parasitics by including a single pole low pass filter $H_{parasitic}(\omega)$:

$$H_{parasitic}(\omega) = \frac{\omega_{3dB}}{\omega_{3dB} + j\omega} \tag{3.49}$$

$$H_{sim}(\omega) = H_{laser}(\omega)H_{parasitic}(\omega) \tag{3.50}$$

Langevin noise sources are now defined as:

$$\langle F_S F_S \rangle = 2\Gamma \frac{\beta NS}{\tau_N}\left[1 + \frac{1}{SV_p}\right] \tag{3.51}$$

$$\langle F_S F_N \rangle = -\left(2\frac{\beta NS}{\tau_N}\left[1 + \frac{1}{2V_p S}\right] - \frac{GS}{V_p}\right) \tag{3.52}$$

$$\langle F_N F_N \rangle = \frac{2}{\Gamma}\frac{\beta NS}{\tau_N}\left[1 + \frac{1}{2V_p S}\right] - \frac{GS}{V} + \frac{\eta_i (I + I_o)}{qV^2} \tag{3.53}$$

The photon carrier density and RIN are defined in (3.33) and (3.35). The threshold current is computed from the carrier rate equation at steady state and with the assumption that there is an absence of photons. Therefore, we can calculate the threshold current given a set of laser parameters:

$$I_{th} = \left(\frac{qV}{\eta_i}\right)\left(\frac{N_{th}}{\tau_n}\right) \tag{3.54}$$

where N_{th} is the threshold carrier density, which is dependent on N_o and gain such that at steady state: $N(I > I_{th}) = N_{th}$ due to gain clamping.

In this section V = 2.4x10^{-12} cm^3 and V_p = 0.628x10^{-10} cm^3. Threshold current was set as a constraint to 0.5mA. All experimental measurements were within the linear regime of the laser's LI curve in order to minimize thermal effects.

3.4.1 Single-Objective Parameter Extraction Drawbacks – Bandwidth

Parameter extraction from measured $H(\omega)$ has been done in many ways [57]-[59]. In this paper, we linearize the non-stochastic rate equations (i.e., with no Langevin noise sources) through the same differential analysis approach introduced in chapter 2. The linearized

intrinsic small signal frequency response $H_{laser}(\omega)$ is characterized by the resonance frequency ω_R and damping γ, which are defined in terms of laser parameters.

The response $H_{sim}(\omega)$ is matched to the experimentally measured $H(\omega)$. The device and parasitic parameters are extracted by minimizing the mean square error (MSE). $H(\omega)$-only parameter extraction has also been done by others using the subtraction method [33]. This approach is not used by us since it does not directly extract bias dependent parasitics.

Results shown in Fig. 3.8a show a good match between the simulated $H_{sim}(\omega)$ and the experimental $H(\omega)$ at multiple bias currents. Unfortunately, as we see in Fig. 3.8b, the RIN characteristics are not accounted for. This is in part because the subset of parameters from the rate equation parameters that have a greater effect on $H(\omega)$ is not the same as the subset having greater impact on RIN.

Table 3. 2 VCSEL Parameters and Typical Values

Laser Parameters	**Bounds**	**BW Only**	**RIN Only**
carrier lifetime (ns) τ_n	1 – 10	10	2.5
photon lifetime (ps) τ_p	1 – 8	2.9	5.6
gain coeff (cm^3/s) g	$1x10^{-7}$ – $1x10^{-4}$	$3.0x10^{-5}$	$2.6x10^{-5}$
spont. emission coeff. β	$1x10^{-7}$ – $1x10^{-1}$	$6.9x10^{-2}$	$9.2x10^{-5}$
gain compression. coeff.(cm^3) ϵ	$1x10^{-19}$ – $1x10^{-15}$	$6.5x10^{-17}$	$2.7x10^{-17}$
carrier density at transparency (cm^{-3}) N_o	$1x10^{18}$ – $1x10^{19}$	$8.9x10^{18}$	$2.1x10^{18}$
calculated material gain (cm^{-1})	refer to [10]	2083	1107
calculated modal gain (cm^{-1})	refer to [10]	79	42

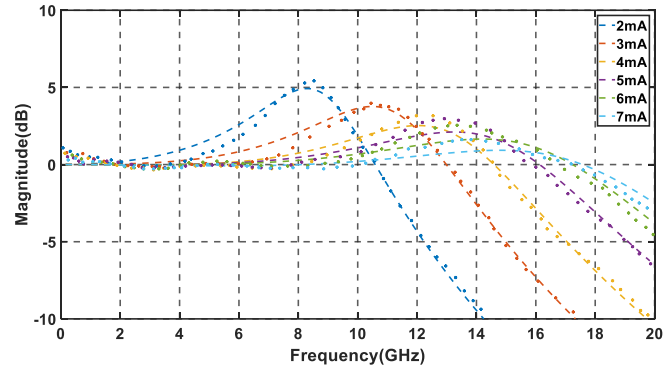

(a)

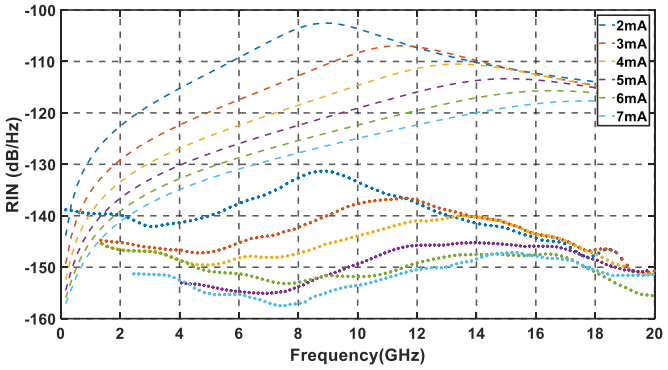

(b)

Figure 3. 8 Comparison between experimental (∗) and simulation using laser parameters extracted using $H(\omega)$ alone (-). The simulated frequency response (a) accurately predicts the experimental observation over a large bias however the RIN(w) (b) simulation significantly overestimates the experimental observation over all bias conditions.

The contour plots of the RMSE versus chosen pairs of parameters reveal which parameters strongly impact $H(\omega)$, Fig. 3.9a-d. The other parameters are fixed to the $H(\omega)$ optimized values listed in Table 3.2. Contours of constant RMSE are indicated. Figure 3a shows the RMSE for a range of spontaneous emission coefficients and photon lifetimes. While spontaneous emission strongly and directly affects RIN, Fig. 3.9a shows that the RMSE for $H(\omega)$ is not strongly dependent on the spontaneous emission coefficient. The RMSE does exhibit a minimum at large spontaneous emission coefficient that are likely unrealistic. Figure 3.9b and 3.9d shows the RMSE when one of the two parameters that is varied has a moderate impact on the bandwidth, while the other has a stronger impact. It

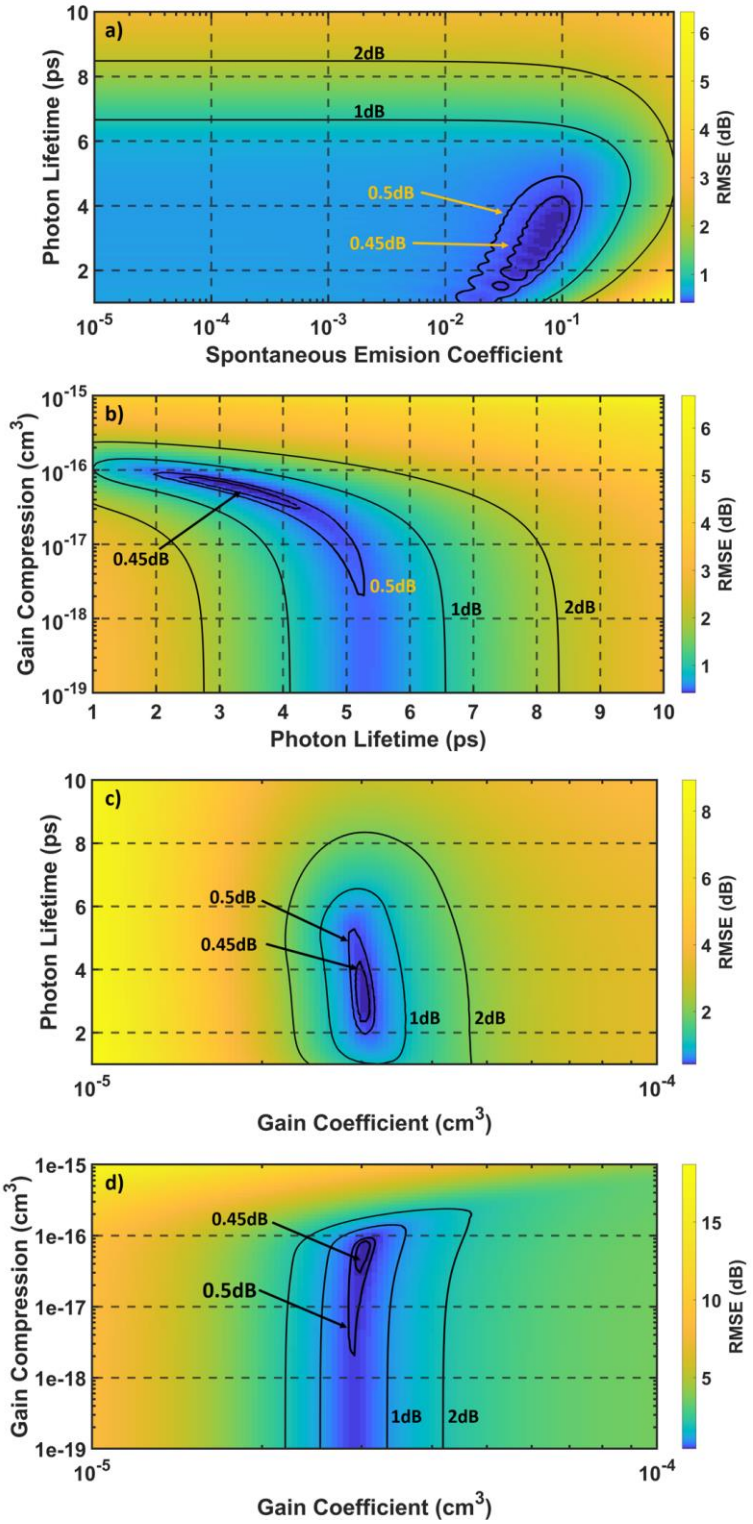

Figure 3. 9 Contour plots of the root mean squared error (RMSE) between simulated and measured $H(\omega)$ for various device parameters. Overestimation of the spontaneous emission coefficient when using $H(\omega)$-only leads to the very high inaccuracies as shown in the RIN spectra in Fig. 3.8b.

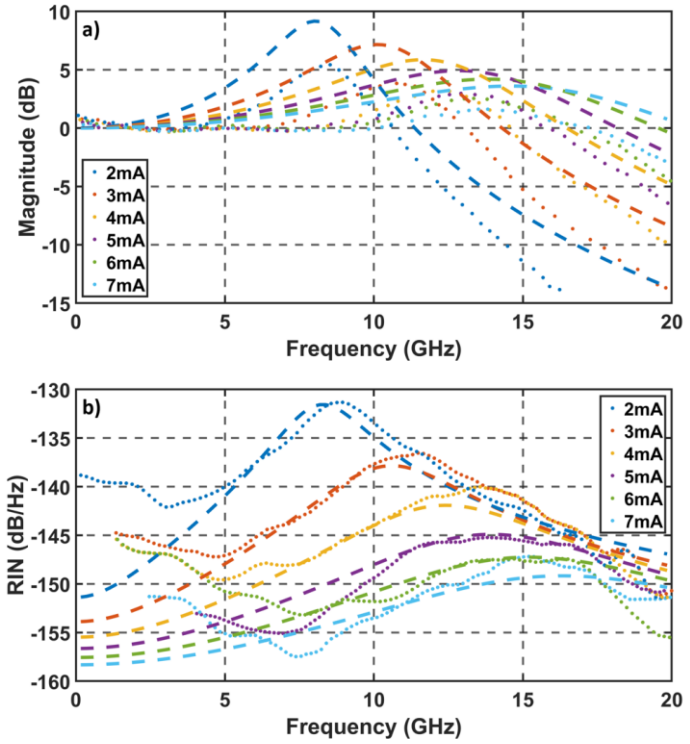

Figure 3. 10 Comparison between experimental (∗) and simulation (-) when laser parameters are extracted using $RIN(\omega)$ alone. Parameter extraction through RIN does cannot extract parasitic elements. Note that resonant frequencies do not match at higher bias currents and therefore, cannot be corrected by a simple low pass RC filter.

can be seen from Fig. 3.9b and 3.9d that varying gain compression has an impact at very low values. Fig. 3.9c shows the results when both parameters have near equal impact on the bandwidth. Multiple local minima in our overall search space may leave a simple gradient-based optimizer stuck in a local minimum. A global optimization method is therefore recommended when extracting such parameters.

3.4.2 Single-Objective Parameter Extraction Drawbacks – RIN

While parameter extraction based on $H(\omega)$ ensures an accurate incorporation of ISI, the noise sources also need to be realistically calibrated. Parameter extraction based on measured RIN spectra is less common, primarily due to the high sensitivity and precision

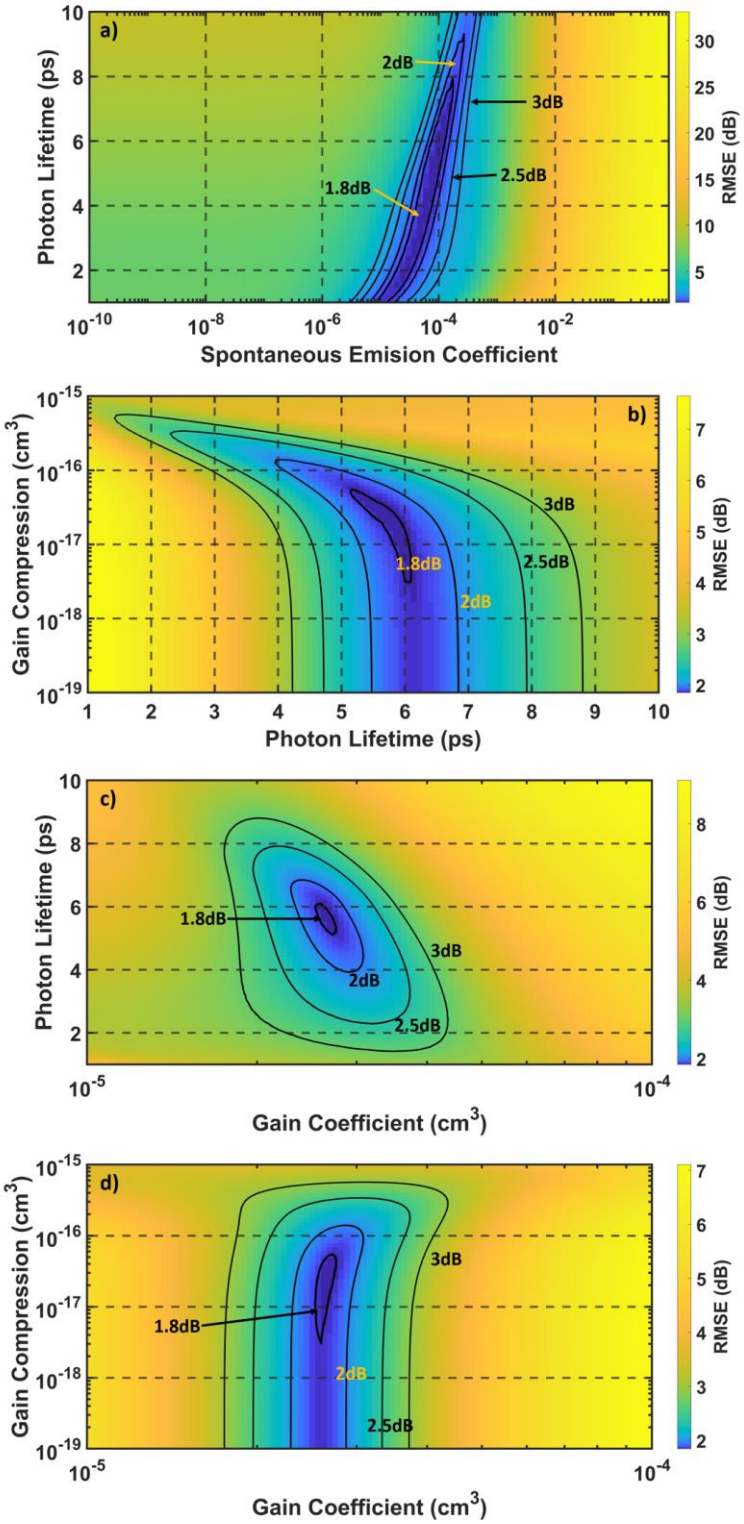

Figure 3. 11 Impact of various device parameters on the $RIN(\omega)$ RMSE. $RIN(\omega)$ RMSE is typically higher than $H(\omega)$ RMSE due to higher sensitivity of RIN. Highly dependent noise parameters such as the spontaneous emission are shown to have conflicting minimum RMSE values with those reported in Fig. 3.9.

Table 3. 3 Measured vs. Simulated RIN

Current (mA)	Measured RIN (dB/Hz)	Simulated RIN (dB/Hz)
2	-137.6	-138.3
3	-141.6	-142.8
4	-144.3	-146.0
5	-148.2	-148.5
6	-149.4	-150.5
7	-151.1	-152.2

required in RIN measurement. Here we treat the total RIN as the sum of the RIN of each transverse mode of a multimode laser. The single mode model therefore represents an effective mode that which includes the aggregate behavior of all modes. For accurate parameter extraction in single and multimode models, mode dependent losses should be minimized as low frequency RIN is largely affected by spatial effects rather than the intrinsic VCSEL properties themselves [17]. If the link has significant mode dependent loss the single mode model may be evaluated after this loss occurs.

We extract the device parameters by minimizing the $RIN(\omega)$ RMSE between the measured $RIN_{exp}(\omega)$ and simulated $RIN_{sim}(\omega)$ of (15). It can be seen from Fig. 3.10a and 3.10b that this leads to a good match between the experimental and simulated RIN spectra, while the match is poor for the small signal frequency response. Deviations between measured and simulated RIN do appear at low frequencies. Yet a single mode model is still capable of modeling RIN since:

- RIN is generally lower at lower frequencies which does not contribute to a large fraction of the average RIN

- The resonance frequency and the high frequency roll-off are well simulated which are often the dominant sources of RIN

The second feature is further demonstrated by Table 3.3 which integrates the RIN spectrum to 20 GHz. The impact of the laser parameters on the $RIN(\omega)$ RMSE was studied by varying two parameters at a time, Fig. 3.11a-d. We now see the impact that spontaneous emission coefficient has on the $RIN(\omega)$ MSE. Comparing Fig. 3.9a with Fig. 3.11a we see that the optimum combinations of the spontaneous emission coefficient and photon lifetime is different when using H(ω)-only and RIN(ω)-only approaches. This demonstrates the requirement for multi-objective parameter extraction.

3.4.3 Multi-Objective Optimization

Having demonstrated the limitations of the single-objective parameter extraction approaches, we present a multi-objective parameter extraction technique using the method depicted in Fig. 3.7. Multi-objective optimization allows us to identify the optimum solution from a diverse set of potential solutions. This ensures a good match for both the small signal frequency response and RIN data. Optimization implies that there is a cost function or a set of cost functions that can be minimized. An intuitive way to capture the effects of both $RIN(\omega)$ and $H(\omega)$ is to generate a composite MSE cost function that is a weighted sum of the two MSE cost functions of the single objective approaches. In this section we define this approach as joint optimization. However, the optimal solution in this scenario would depend on the actual weights assigned to the individual MSEs or RMSEs. Searching for a set of weights that visually leads to an optimum solution is both a tedious

Table 3. 4 VCSEL Parameters and Typical Values

Laser Parameters	**Bounds**	**Multi-Obj.**	**Joint Opt.**
carrier lifetime (ns) τ_n	1 – 10	4.2	3.8
photon lifetime (ps) τ_p	1 – 8	3.8	3.5
gain coeff (cm^3/s) g	$1x10^{-7}$ – $1x10^{-4}$	$3.1x10^{-5}$	$3.1x10^{-5}$
spont. emission coeff. β	$1x10^{-7}$ – $1x10^{-1}$	$8.1x10^{-2}$	$6.3x10^{-5}$
gain compression. coeff.(cm^3) ϵ	$1x10^{-19}$ – $1x10^{-15}$	$1.1x10^{-16}$	$7.9x10^{-17}$
carrier density at transparency (cm^{-3}) N_o	$1x10^{18}$ – $1x10^{19}$	$3.7x10^{18}$	$3.1x10^{18}$
calculated material gain (cm^{-1})	refer to [10]	1644	1780
calculated modal gain (cm^{-1})	refer to [10]	62	68

and time-consuming process. On the other hand, multi-objective optimization does not inherently rely on weights. Instead, it gives a set of near-optimal solutions, which can subsequently be sorted. The multi-objective optimization problem is set up as follows [64],[65]:

- **Variable:** X is a multi-dimensional vector of VCSEL parameters. It is a potential solution and a point in a multidimensional hyperspace.
- **Objectives:**
  - f_1: Minimize $H(\omega)$ MSE
  - f_2: Minimize $RIN(\omega)$ MSE
- **Constraints:**
  - Realistic bounds on the laser parameter values (Table 3.4)

The algorithm starts with an initial random population of N=200 candidate solutions and then generates successive generations. Each time a parent population of N is used to generate an offspring population of N solutions using the typical genetic operators like selection, crossover and mutation [64],[65]. The algorithm starts with an initial random

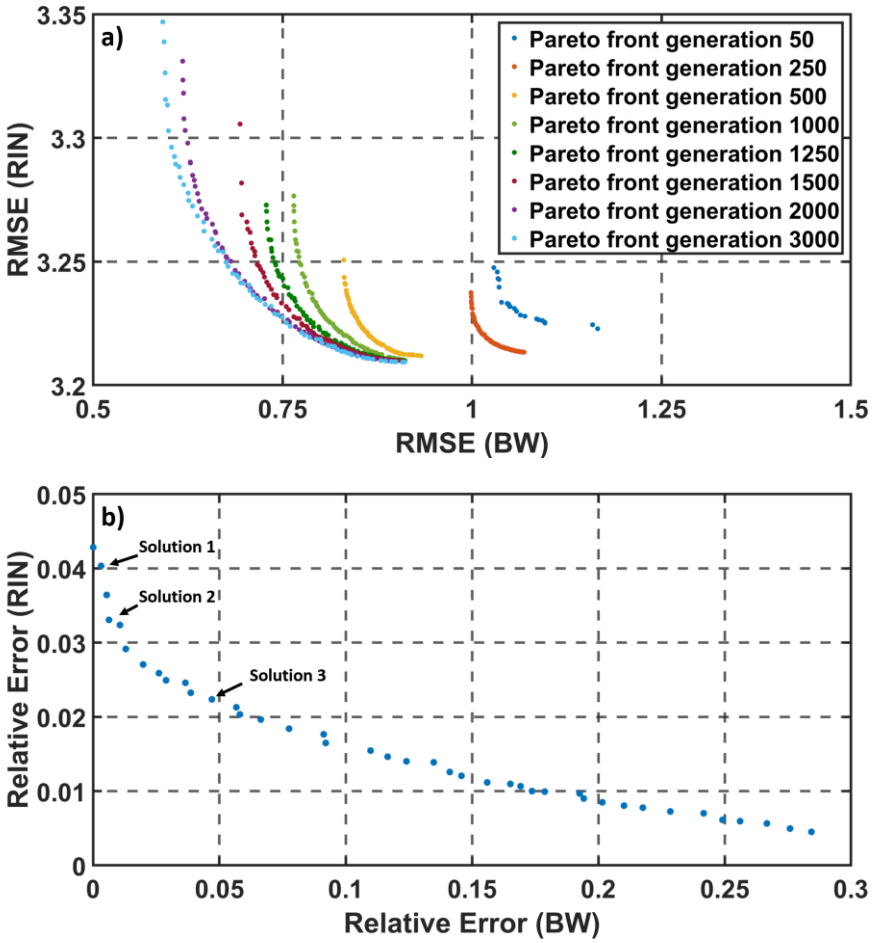

Figure 3. 12 (a) evolution of first pareto front between $RIN(\omega)$ RMSE in dB and $H(\omega)$ RMSE in dB for specific generations, (b) pareto front generation 3000 plotted as the relative error, which is relative to the minimum error found in (a). Plot is focused to show greater detailed around chosen solutions. Selected points indicate solutions in Table 3.5.

Table 3. 5 Multi-Objective Candidate Solutions

Laser Parameters	**Solution 1**	**Solution 2**	**Solution 3**
τ_n (ns)	4.27	4.29	4.24
τ_p (ps)	3.78	3.78	3.80
g (cm^{-3})	3.08×10^{-5}	3.08×10^{-5}	3.02×10^{-5}
β	9.40×10^{-5}	8.10×10^{-5}	8.09×10^{-5}
ϵ (cm^3)	1.09×10^{-16}	1.07×10^{-16}	1.08×10^{-16}
N_o (cm^{-3})	3.63×10^{18}	3.67×10^{18}	3.69×10^{18}

parent population of N=200 candidate solutions having VCSEL parameters drawn from a uniform probability distribution within the specified bounds. This parent population is then used to generate an offspring population of size N through selection, crossover mutation and elite preservation [64]. Selection is a process in which candidate solutions with lower-than-average RMSEs are chosen with a higher probability for generating the next generation through mutation and crossover. Crossover is the process in which two selected candidate solutions, called parents, are combined to generate a child candidate solution. The child candidate solution has VCSEL parameters which are a weighted average of the parent's parameters. Some of the VCSEL parameters of the generated child candidate solution are then perturbed for preserving and introducing diversity, while still satisfying the parameter bounds. Finally, elite preservation is the process of preserving some of the better candidate solutions from the parent to the offspring generation. The offspring population is included with the parent population and the best N solutions are chosen from the 2N candidates. This is achieved by using non-domination Pareto fronts. A non-domination Pareto front is a set of solutions which do not dominate each other. Two possible solutions do not dominate each other if going from one solution to the other trade-

offs one objective with the other. Once the first non-domination Pareto front is identified then the points in this front are removed from consideration and the process is repeated to get the second non-domination Pareto front. This process is repeated until we have N points which have been classified into some Pareto front from the 2N candidates. In the last front, not all points can be chosen because of the hard limit of N points. In such a scenario, a diversity operator called crowding distance is computed for the points on this last Pareto front. The higher the crowding distance of a solution, the higher is its distance from other solutions. The solutions with maximum crowding distance are chosen from this last Pareto front. This maintains diversity in the population. The chosen N points then become the parent population for the next round of optimization.

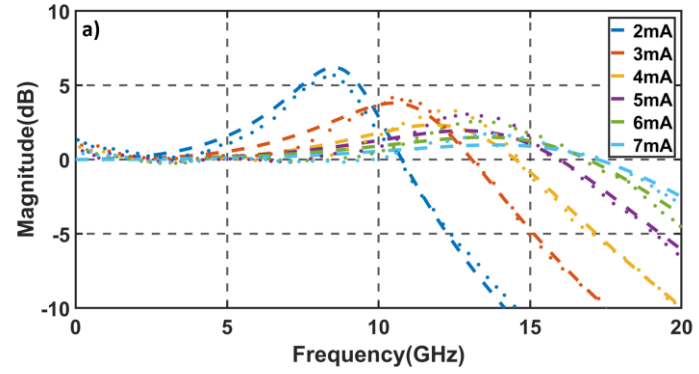

(a)

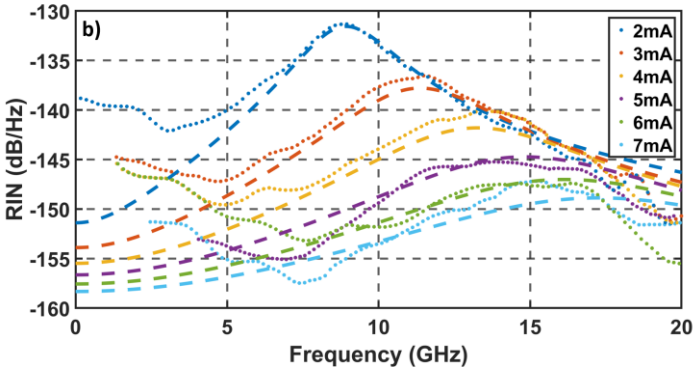

(b)

Figure 3. 13 Match between experimental (∗) and simulation (-) when laser parameters are extracted using multi-objective optimization. Good match between experimental and simulated results are expected.

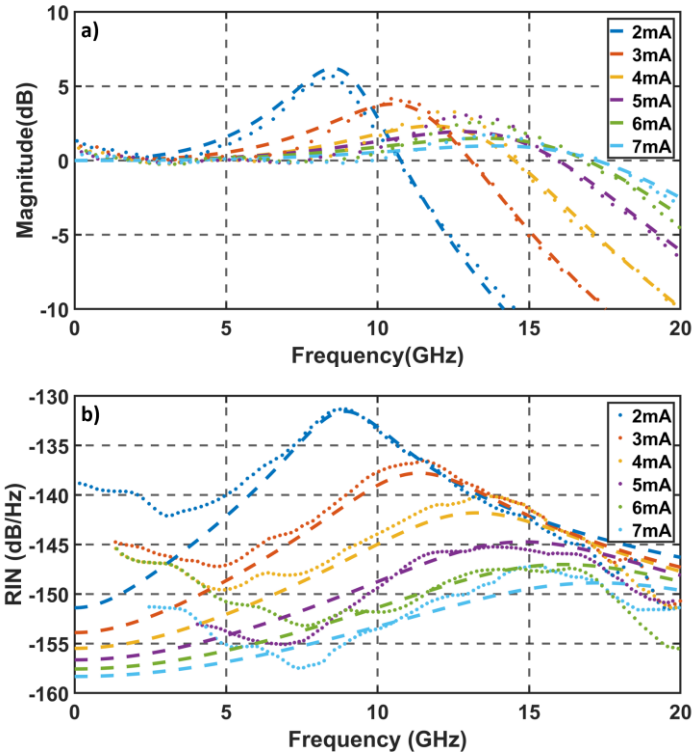

Figure 3. 14 Comparison between experimental (∗) and simulation (-) when laser parameters are extracted using scatter search gradient decent optimization. Good match between experimental and simulated results are expected.

3.4.4 Multi-Objective Parameter Extraction Results

The evolution of the first non-domination Pareto front over the generations is shown in Fig. 3.12a. The first non-domination Pareto front after the algorithm stops is the Pareto-optimal set of solutions. We can see that the RIN RMSE is much larger than the BW RMSE, making a summation of the two a biased metric. Figure 3.12b shows the $RIN(\omega)$ RMSE and $H(\omega)$ RMSE in relative terms to their minimum value from all the solutions on the Pareto optimal front. We then choose the solution that minimizes the total relative MSE, where the total relative RMSE is defined as the sum of the *relative* $RIN(\omega)$ RMSE and the relative $H(\omega)$ RMSE. The extracted parameters are noted in Table 3.4 under the multi-objective column. Figure 3.13 depicts a good match between simulated and experimental

results using the solution selected from the Pareto-optimal front. This solution ensured that we could reasonably minimize $RIN(\omega)$ RMSE and $H(\omega)$ RMSE without having to significantly trade-off one against the other. Table 3.5 depicts three candidate solutions on the pareto front of Fig. 3.12b, where solution 2 has the minimum total relative RMSE. These solutions are acceptable and have similar laser parameter values. As we move rightwards from the selected solution, the resulting candidate solution provides a closer RIN spectrum match at the cost of BW match and a similar but opposite trend is experienced when we move leftwards. We note that the solutions on the Pareto-optimal front have a larger RMSE than the RMSE attained using the $RIN(\omega)$-only or $H(\omega)$-only approaches. This is expected since solutions using the single objective approach optimizes one of the RMSEs without giving any regard to the other RMSE and therefore would not be on the optimal Pareto front. It should be noted that all the extracted parameters are well within the bounds and agree with previously reported values [66],[67].

3.4.5 Multi-Objective and Joint Optimization Approaches

Multi-objective genetic optimization algorithms are heuristic algorithms. Therefore, the global minimum is not always guaranteed. Hence, we test it against a gradient based, joint optimization algorithm which guarantees convergence to a minimum value. In joint optimization the multiple objectives would have to be weighted and combined into a single overall objective. If one of the objectives is difficult to minimize, then allowing automatic weight optimization may lead to the lowest weight allowed by the bounds being often chosen for that challenging objective. Therefore, this weight optimization must be done manually by trying different values till the user is satisfied with the results, leading to an on average longer computation time. We use the joint optimization technique to validate

the efficient multi-objective approach. We optimize using various combinations of weights and parameters and then identify the best solution. Since it is not possible to predict apriori which weights would lead to the best solutions, a wide spread of weights was chosen for the various trials of the joint optimization. Figure 3.14 depicts the optimized solution with results nearly identical to those found using the multi objective method. Table 3.4 shows that the multi-objective optimization gives a similar solution to that obtained by the exhaustive joint optimization approach and therefore verifies that our genetic algorithm approach converges to a reasonable set of values that is most likely close to the optimum solution.

3.4.6 Advantages of the Multi-Objective Approach

To further emphasize the need for parameter optimization using both $H(\omega)$ and $RIN(\omega)$ measurements, we compare our results using two well-established figures of merit. The K-factor relates the damping factor (γ) to the resonance frequency (f_R) [23],[39],[66]-[68]:

$$\gamma = K f_R^2 + \gamma_o \tag{3.55}$$

where γ_o is the damping factor offset and the laser's maximum intrinsic bandwidth f_{3dB} is:

$$f_{3dB,max} = \frac{2\pi\sqrt{2}}{K} \tag{3.56}$$

Typically, the VCSEL parameters are extracted using only bandwidth measurements. However, the small signal response is known to be limited by the parasitic

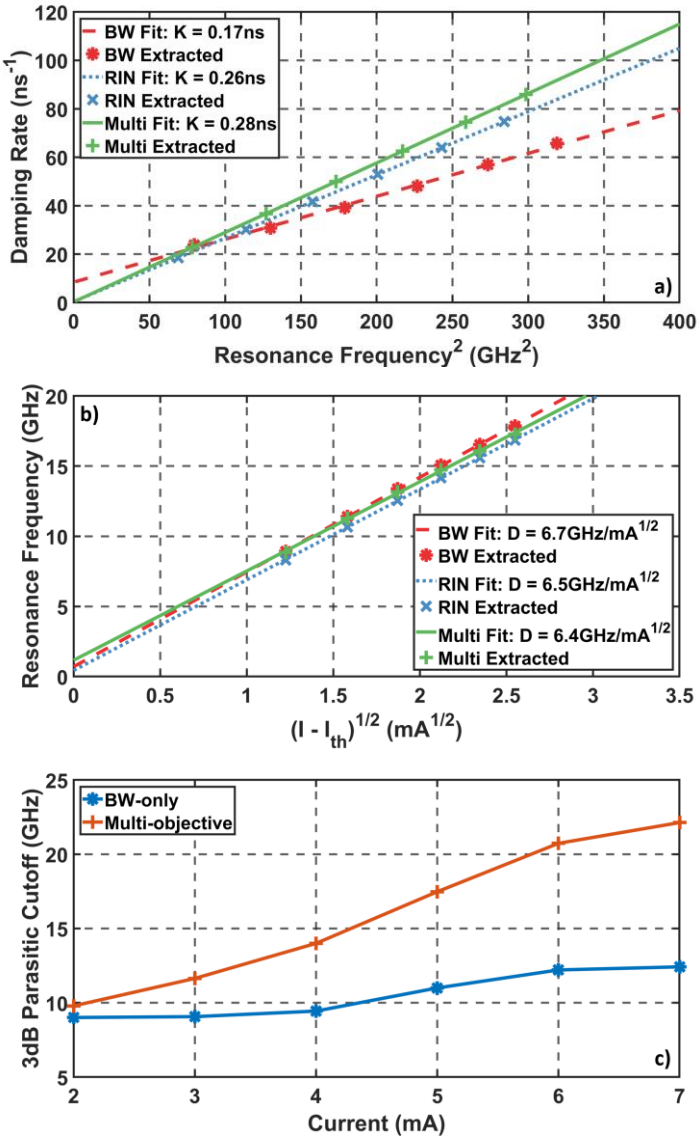

Figure 3. 15 (a) K-factor from extracted resonance frequency (b) D-factor from extracted resonance frequency (c) -3dB parasitic frequency cutoff for BW-only and multi-objective parameter extraction.

response of the device. Therefore, RIN measurements would offer the great advantage of calculating γ and f_R with greater accuracy, since these measurements are not influenced by electrical parasitics. Unfortunately, RIN measurements involve detecting low signal levels and hence have higher error sensitivities. Thus, accurately obtaining the γ - f_R^2 curve using only RIN measurements is challenging. Parameter extraction using both $H(\omega)$ and RIN measurements leverages both types of measurements and allows for what we believe

to be a more accurate representation of the K-parameter. Figure 3.15a shows the extracted γ - f_R^2 points and the line of best fit. As Table 3.6 shows, $H(\omega)$-only and $RIN(\omega)$-only parameter extraction results differ by a large amount leading to a 20GHz difference in the maximum f_{3dB} intrinsic bandwidth.

To achieve the highest possible overall bandwidth, we must carefully account for the interaction between the intrinsic and extrinsic factors. Though the K-factor sets the highest achievable intrinsic 3dB response, extrinsic effects from self-heating and electrical parasitics limit the overall small-signal bandwidth. To minimize (to an extent) the impact self-heating and electrical parasitics found in VCSELs, it is necessary for the resonance frequency to increase at high rate with drive current. This translates into a high D-factor requirement, where the D parameter is formulated as [69]:

$$D = \frac{f_R}{\sqrt{I_{drive} - I_{th}}} \tag{3.57}$$

The D-factor quantifies the rate at which the resonance frequency increases with current. Resonance frequency is dominated by extrinsic factors at high bias currents. Therefore, the D-factor must be evaluated at low currents, where both thermal effects and gain compression are negligible. Figure 3.15b depicts the cases shown in Table 3.6.

Table 3. 6 K and D factors

	K-factor	**D-factor**	$f_{3dB,max}$
$H(\omega)$-only	0.17 ns	6.7 GHz/mA$^{1/2}$	52.2 GHz
$RIN(\omega)$-only	0.26 ns	6.5 GHz/mA$^{1/2}$	34.2 GHz
Multi-objective	0.28 ns	6.4 GHz/mA$^{1/2}$	31.7 GHz

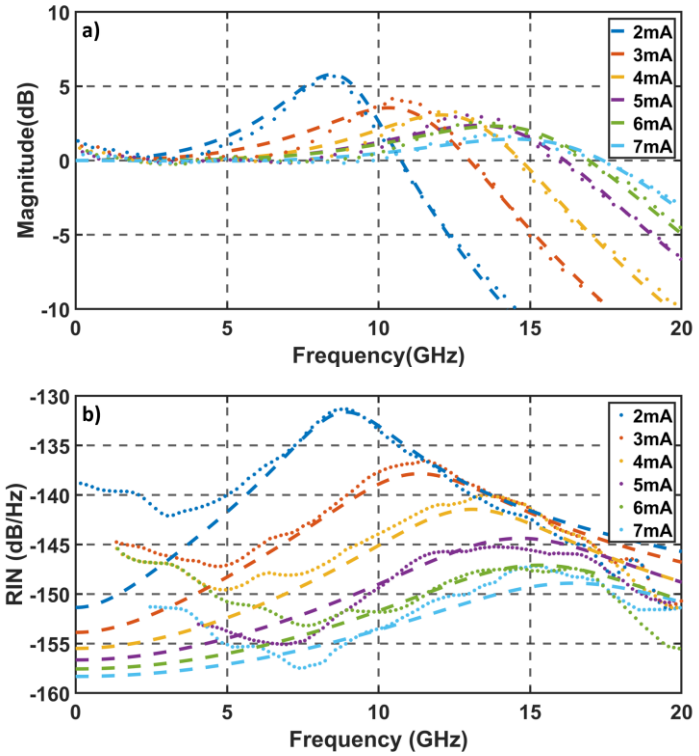

Figure 3. 16 Comparison between experimental (∗) and simulation (-) when laser parameters are extracted using low, middle and high currents. A better though small improvement between experimental and simulated results is achieved.

It can be seen from Fig. 3.15c that the parasitic bandwidth computed by the $H(\omega)$-only approach is low, unlike the multi-objective approach. The $H(\omega)$-only approach overestimates the intrinsic bandwidth which leads to a low K-factor and hence requires a low parasitic bandwidth to match the measured overall bandwidth. This can also be seen from Table 3.6. On the other hand, the multi-objective approach leverages both $H(\omega)$and $RIN(\omega)$ measurements to estimate the intrinsic bandwidth more accurately and which for this example, yields a higher parasitic bandwidth.

3.4.7 Temperature Dependence

Fig 3.16 shows the response of extracting parameters using a pair of close bias currents. Table 3.7 summarizes the results. The extracted parameters correspond to performance at

Table 3. 7 Grouped Parameter Extraction

Laser Parameters	**2mA-3mA**	**4mA-5mA**	**6mA-7mA**
Carrier lifetime(ns) τ_n	3.1	4.8	4.29
Photon lifetime (ps) τ_p	3.2	3.4	2.64
Gain (cm^{-3}) g	$3.1x10^{-5}$	$2.9x10^{-5}$	$2.7x10^{-5}$
Spont. emission coeff. β	$6.6x10^{-5}$	$4.5x10^{-5}$	$2.3x10^{-5}$
gain compression. coeff. (cm^3) ϵ	$1.1x10^{-16}$	$5.47x10^{-17}$	$6.8x10^{-16}$
carrier density at transparency (cm^{-3}) N_o	$2.5x10^{18}$	$4.1x10^{18}$	$3.51x10^{18}$

various bias points and hence to different junction temperatures. The extracted parameters therefore account for these changes. However, the match between the experimental and simulated modulation response as well as RIN for these three sets done separately is similar to the match obtained by optimizing all six bias currents together.

We therefore believe that over the chosen current range, thermal variations do not dominate device performance, and that an accurate parameter extraction can be achieved without explicitly needing to account for such variations, as indicated by the agreement between the single fit and the 3-set fit. Nevertheless, laser parameters that are a function of input current/temperature can be included to increase accuracy.

CHAPTER 4

MULTIMODE VCSEL MODEL

In this chapter we expand on our previous single mode laser rate equation. Though single mode rate equations have been shown capable of characterizing multimode lasers, they are still incapable of fully characterizing noise and bandwidth limitations when laser modes are launched into optical fiber. In the following sections we will present a stochastic multimode vertical cavity surface emitting laser model aimed at optimizing optical links. A generalized linearization method will be presented and applied to commercially available multimode VCSELs. The model, coupled with our parameter extraction method, has been found to accurately simulate experimental results from 2 VCSEL designs, and depicts VCSEL transverse mode noise effects that are increasingly important in high-speed PAM-4 VCSEL links. Recent experimental findings have found that noise correlations among VCSELs having both positive and negative correlations [2],[70]-[72]. Therefore, a model with at least 3 modes is required to investigate the probable cause of this phenomena.

In order to accurately represent commercial grade VCSELs, multimode models are necessary as mode partition noise, relative intensity noise and inter/intra modal dispersion become the dominant VCSEL link impairments. Furthermore, the development of few mode VCSELs [73]-[75] has emphasized the need for accurate multimode models as the frequency dependence of noise and modulation response can greatly affect the performance in high-speed optical links. Here we present the theory basis of our multimode model as well as our parameter extraction methodology. Additionally, through simulations we show

that the interaction between the spatial filtering and the positive /negative mode noise correlations is the fundamental cause of exponential RIN peaking at low frequencies.

4.1 Multimode Laser Rate Equations

VCSEL laser dynamics can be modeled by a set of coupled rate equations. This set describes the relations between the carrier density N, and the separate photon densities S_m for each mode, m. The set of multimode mode density laser rate equations are [23]:

$$\frac{dN}{dt} = \frac{\eta_i I_{out}}{qV} - \frac{N}{\tau_n} - \sum\nolimits_m v_{gm} G_m S_m + F_N(t) \tag{4.1}$$

$$\frac{dS_m}{dt} = -\frac{S_m}{\tau_{pm}} + \Gamma_m R'_{spm} + \Gamma_m v_{gm} G_m S_m + F_{Sm}(t) \tag{4.2}$$

where η_i is the injection efficiency, q the electron charge, τ_n, τ_{pm} are the carrier lifetime and photon lifetime respectively, v_{gm} is the group velocity, Γ_m the confinement factor defined as the ratio of the active region volume V of the carrier reservoir to the m^{th} mode volume V_{pm} of the photon reservoir. Here, R'_{spm} is the fraction of the spontaneous emission that lases into the m^{th} mode of interest:

$$R'_{spm} = \frac{v_{gm} G_m n_{spm}}{V_{pm}} \tag{4.3}$$

where n_{spm} is the population inversion factor. While the spontaneous emission coefficient β commonly found in laser rate equations is not explicitly defined but can be derived for each mode [23]:

$$\beta_m = \frac{R'_{spm}}{R_{sp}} = \frac{\Gamma_m v_{gm} G_m n_{spm}}{\eta_i \eta_r I/q} \tag{4.4}$$

R_{sp} is the spontaneous recombination rate, while η_r is the radiative efficiency. The gain-carrier density relation in a quantum well experienced by each mode is approximated by a logarithmic 3 term approximation, which has been found to better approximate gain at over a wider range of carrier densities [23]:

$$G_m = \frac{g_o}{1 + \sum_n \epsilon_{nm} S_n} ln\left(\frac{N + N_s}{N_s + N_t}\right) \tag{4.5}$$

here N_t is carrier density at transparency and N_s is a linearity parameter used to determine the shape of the gain. Note that the $1/(1 + \sum_n \epsilon_{nm} S_n)$ term in the equation represents the phenomenological characterization of the nonlinear damping caused by such effects as carrier heating and spectral hole burning. ϵ_{nm} represents the gain saturation/compression which will be thoroughly investigated in section 4.2.4. Though more advanced models have been presented in literature to account for structural differences due to more advanced structures, we show that this model can capture the important characteristics found in directly modulated VCSELs.

Whereas equations 1 and 2 only account for the intrinsic response of the laser. Bias dependent VCSEL parasitics are accounted through a third differential equation, which filters the effective drive current I_{drive} by using a low pass filter of bandwidth ω_{3dB}.

$$\frac{dI}{dt} = \omega_{3dB}(I_{drive} - I) \tag{4.6}$$

Thermal effects, like the roll-over in the LI curve, have not been incorporated. However thermal effects can be incorporated by using an additional differential equation that captures the junction temperature which is dependent on the drive current and ambient temperature [21].

4.2 Linearization of Multimode Laser Rate Equations

As stated previously in Chapter 2, for an accurate and computationally efficient representation of both the small signal frequency response and RIN spectrum, we must first generate a linear set of equations in which to optimize. These equations should capture the laser rate equation dynamics under small signal representations. This section will first introduce the derivation of the BW and RIN spectrum for a multimode VCSEL with a single carrier reservoir using the differential analysis method.

The differential analysis method was discussed in great detail in Chapter 2. Some steps will therefore be omitted in this analysis.

The differential transforms of the laser rate equations (4.1) and (4.2) are as follows:

$$d\left[\frac{dN}{dt}\right] = \frac{\eta_i}{qV} dI - \gamma_{NN} dN - \sum\nolimits_m \gamma_{NS_m} dS_m \tag{4.7}$$

$$d\left[\frac{dS_m}{dt}\right] = \gamma_{S_m N} - \sum\nolimits_n \gamma_{S_m S_n} dS_n \tag{4.8}$$

where,

$$\gamma_{NN} = \frac{1}{\tau_n} + \sum\nolimits_m v_{gm} S_m \alpha_m \tag{4.9}$$

$$\gamma_{NS_m} = v_{gm}G_m - \sum\nolimits_n v_{gm}S_m\alpha_{nm} \tag{4.10}$$

$$\gamma_{S_mN} = \frac{\Gamma_m v_{gm} n_{spm}}{V_{pm}}\alpha_m - \Gamma_m v_{gm}S_m\alpha_m \tag{4.11}$$

$$\gamma_{S_mS_m} = \frac{1}{\tau_{p_m}} - \Gamma_m v_{gm}G_m + \Gamma_m v_{gm}\alpha_{mk}\left(\frac{n_{spm}}{V_p} + S_m\right) \tag{4.12}$$

$$\gamma_{S_mS_n}|_{m\neq n} = \frac{\Gamma_m v_{gm} n_{spm}}{V_{pm}}\alpha_{nm} + \Gamma_m v_{gm}S_m\alpha_{nm} \tag{4.13}$$

here, parameters such as γ_{NS_m} define the effect on N caused by changes in S_m. The rate coefficients γ_{NN}, γ_{NS_m}, γ_{S_mN}, $\gamma_{S_mS_m}$ and $\gamma_{S_mS_n}|_{m\neq n}$ were introduced in section 3.2. γ_{NN} corresponds to the differential carrier lifetime, γ_{NS_m} the gain experienced in each mode, γ_{S_mN} the differential lifetime of the carriers, and $\gamma_{S_mS_m}$ the effective photon lifetime, respectively. Furthermore, the introduction of these rate coefficients allows us to represent the differential rate equations in a more compact form:

The α parameters encapsulate the gain variation dG_m which can be expanded by assuming that it is affected by both the carrier and photon density variations:

$$dG_m = \alpha_m dN - \sum\nolimits_n \alpha_{nm}\, dS_n \tag{4.14}$$

and defined by their partial derivatives

$$\alpha_m = \frac{\partial G_m}{\partial N} \quad , \quad \alpha_{nm} = -\frac{\partial G_m}{\partial S_n} \tag{4.15}$$

4.2.1 Multimode Small Signal Frequency Response

The rate coefficients defined in the previous section give us a convenient and compact form to represent differential rate equations. Analogous to the single mode case, we assume no Langevin noise sources, the small signal current modulation solutions are assumed to be in the form $dI(t) = I'e^{j\omega t}, dN(t) = N'e^{j\omega t}, dS_m(t) = S'_m e^{j\omega t}$ by then setting $d/dt \to j\omega$ we obtain

$$\begin{bmatrix} \gamma_{NN} + j\omega & \gamma_{NS_1} & \cdots & \gamma_{NS_m} \\ -\gamma_{S_1N} & \gamma_{S_1S_1} + j\omega & \cdots & \gamma_{S_1S_m} \\ \vdots & \vdots & \ddots & \vdots \\ -\gamma_{S_mN} & \gamma_{S_mS_1} & \cdots & \gamma_{S_mS_m} + j\omega \end{bmatrix} \begin{bmatrix} N' \\ S'_1 \\ \vdots \\ S'_m \end{bmatrix} = \frac{\eta_i I'}{qV} \begin{bmatrix} 1 \\ 0 \\ \vdots \\ 0 \end{bmatrix} \tag{4.16}$$

Cramer's solution will lead to a solution in the form of

$$S'_m(\omega) = C_m H_m(\omega) \tag{4.17}$$

here C_m is a scaling factor. The normalized intrinsic response of the system will then be:

$$H_{laser}(\omega) = \frac{\sum_m S'_m(\omega)}{\sum_m S'_m(0)} \tag{4.18}$$

Note that unlike the single mode approximation in chapter 2, the C_m coefficient is important for multimode linearization as power levels among modes may differ. The complete response of the system being:

$$H_{total}(\omega) = H_{laser}(\omega) H_{parasitic}(\omega) \tag{4.19}$$

Furthermore, the power in each mode can be calculated as

$$P_m = \eta_o h \upsilon_m \frac{S_m V_{pm}}{\tau_{pm}} \tag{4.20}$$

here, η_o is the optical efficiency, h is Plank's constant, and υ_m is the free space frequency.

4.2.2 Multimode Spectral Densities

Linearization of the laser noise spectral density follows a similar structure as the previous section but now assumes no current modulation, which leads to:

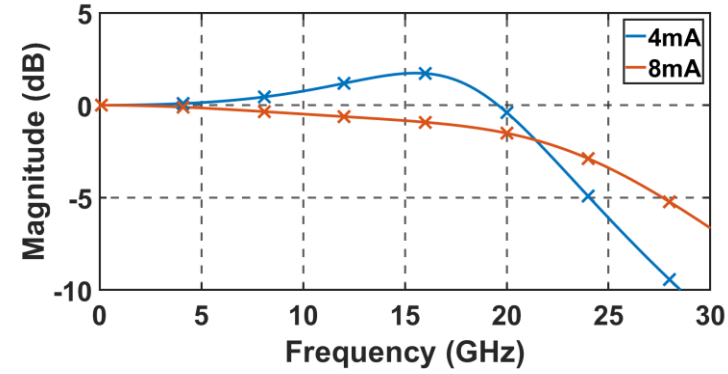

(a)

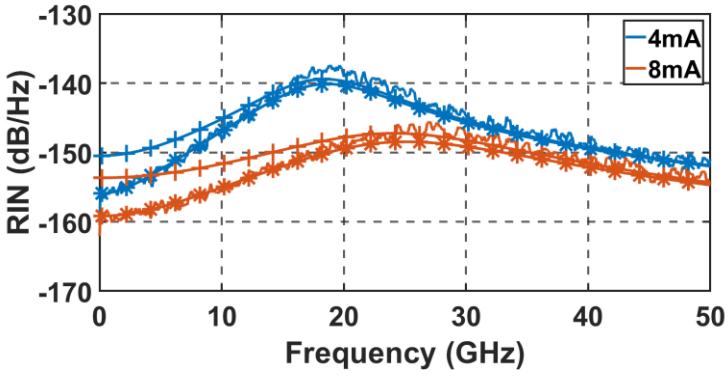

(b)

Figure 4. 1 a) Example S21 between simulated (-) and linearized (x) response using VCSEL parameters from Table 1. b) Example RIN spectrum comparing simulated response with cross correlations (-) vs linearized response with cross correlations (∗) and RIN spectrum without cross correlations (+). RIN spectrum without cross correlations deviates from theory as we move to lower frequencies.

Table 4. 1 VCSEL Parameters

Laser Parameters	**VCSEL A (TEST VCSEL)**
injection efficiency η_i	0.7
photon lifetime (ps) $[\tau_{p1}, \tau_{p2}, \tau_{p3}] = \tau_p$	3
gain coeff (cm^{-1}/s) g_o	$3x10^4$
carrier lifetime (ns) τ_n	2.5
gain linearity parameter (cm^{-3}) N_s	$3x10^{18}$
carrier density at transparency (cm^{-3}) N_{tr}	$1x10^{18}$
gain comp. coeff. (cm^3) $[\epsilon_{11}, \epsilon_{22}, \epsilon_{33}] = \epsilon$	$4x10^{-16}$
mode volume (cm^3) $[V_{p1}, V_{p2}, V_{p3}] = V_p$	$[0.63,0.63,0.63]\ x10^{-10}$

$$\begin{bmatrix} \gamma_{NN} + j\omega & \gamma_{NS_1} & \cdots & \gamma_{NS_m} \\ -\gamma_{S_1N} & \gamma_{S_1S_1} + j\omega & \cdots & \gamma_{S_1S_m} \\ \vdots & \vdots & \ddots & \vdots \\ -\gamma_{S_mN} & \gamma_{S_mS_1} & \cdots & \gamma_{S_mS_m} + j\omega \end{bmatrix} \begin{bmatrix} N' \\ S'_1 \\ \vdots \\ S'_m \end{bmatrix} = \begin{bmatrix} F_n(\omega) \\ F_{S_1}(\omega) \\ \vdots \\ F_{S_m}(\omega) \end{bmatrix} \tag{4.21}$$

Solutions for each mode can be solved using Cramer's rule.

Photon spectral density is now defined as:

$$\boldsymbol{S_m} = \frac{1}{2\pi} \int \langle P'_m(\omega) P'_m(\omega') \rangle \, d\omega' \tag{4.22}$$

and the total spectral density

$$\boldsymbol{S_{total}} = \frac{1}{2\pi} \int \langle \sum_m P'_m(\omega) \sum_m P'_m(\omega') \rangle \, d\omega' \tag{4.23}$$

For accurate and enhanced laser parameter extraction we must create a set of Langevin noise sources which account for all particle transitions between carrier and photon reservoirs. Langevin noise source spectral densities have been added to the model through the addition of the following correlations:

$$\langle F_i F_j \rangle = \frac{1}{2\pi} \int \langle F_i(\omega) F_j(\omega')^* \rangle \tag{4.24}$$

and are defined as

$$\langle F_N F_N \rangle = \frac{\eta_i I}{qV^2} + \sum\nolimits_m 2R'_{spm} S_m - \sum\nolimits_m \frac{v_{gm} G_m S_m}{V} \tag{4.25}$$

$$\langle F_N F_{S_m} \rangle = -2R'_{spm} S_m + \frac{v_{gm} G_m S_m}{V_{pm}} \tag{4.26}$$

$$\langle F_{S_m} F_{S_m} \rangle = 2\Gamma_m R'_{spm} S_m \tag{4.27}$$

$$\langle F_{S_m} F_{S_n} \rangle|_{m \neq n} = 0 \tag{4.28}$$

RIN can now be defined as:

$$RIN(\omega) = 10 \log_{10} \left(2 \frac{\boldsymbol{S}_{total}(\omega)}{(\sum_m P_m)^2} \right) \tag{4.29}$$

Finally, the threshold current can be derived from the carrier rate equation assuming an absence of photons:

$$I_{threshold} = \frac{qV}{\eta_i} \frac{N}{\tau_n} \approx \frac{qV}{\eta_i} \frac{N_{tr}}{\tau_n} \tag{4.30}$$

In this study we relied on previous measurements and existing literature to employ a V = 2.4x10^{-12} cm^3, n_{spm} = 1.5 for all modes, and $\lambda_{1,2,3}$= 850, 850.5, 851nm respectively. The group velocity v_{gm} was calculated to be 8.19x10^9 cm/s for all modes near 850nm by using the Sellmeyer equation for a pure GaAs compound. Table 4.1 shows a general set of laser

parameters VCSELs which corresponds to a threshold current of 0.5mA. Figure 4.1 shows the:

- Frequency response with a -3dB bandwidth of ~23GHz at 8mA
- The corresponding RIN spectrums using parameters from Table 4.1.

4.2.3 Mode Noise Correlations

While the existence of MPN and RIN in VCSELs has been measured and modeled in the past [76]-[82]. Recent experiments have found positive and negative correlations between the noise of dominant modes. In this section we expand on our previous work and create a 3 mode VCSEL model which can simulate the positive and negative noise correlations found in this paper [2]. These effects will be generated through the gain compression term defined in (4.5).

It is important to note that the autocorrelations in (4.25) and (4.27) should always stay positive, while the cross correlation (4.26) should always stay negative. Therefore, to accurately represent the noise correlations, we have defined the following set of time domain Langevin noise sources:

$$F_N(t) = -\varphi \sum\nolimits_k \sqrt{\frac{|\langle F_N F_{Sk}\rangle|}{\Delta t}}\, \boldsymbol{X}_k + \sqrt{\frac{F_N F_N}{\Delta t} - \varphi^2 \sum\nolimits_k \frac{|\langle F_N F_{Sk}\rangle|}{\Delta t}}\, \boldsymbol{X}_{max+1} \qquad (4.31)$$

$$F_{Sm}(t) = -\frac{1}{\varphi}\sqrt{\frac{|\langle F_N F_{Sm}\rangle|}{\Delta t}}\, \boldsymbol{X}_m + \sqrt{\frac{F_{Sm} F_{Sm}}{\Delta t} - \frac{1}{\varphi^2}\frac{|\langle F_N F_{Sm}\rangle|}{\Delta t}}\, \boldsymbol{X}_{m+max+1} \qquad (4.32)$$

Here, φ is a constant that prevents the radicand in (4.32) from becoming negative while still maintaining the correlations defined in (4.25) - (4.28). $\boldsymbol{X}$ is a random variable with a gaussian distribution, and Δt represents the time between sampling points. The term max in the (4.31), (4.32) represents the numerical maximum number of modes, for a 3-mode model $max = 3$. We would also like to note that previous VCSEL models approximate (4.31) and (4.32). Though still highly useful, these models have slightly deviated from theory for a given set of parameters as depicted in Fig 4.1b. Without the cross correlations a different set of laser parameters would be needed to model such lasers. We believe that (4.31) and (4.32) with the added cross-correlation terms improve the accuracy of our laser model, especially if one wishes to extract self-consistent laser parameters.

To determine the main cause of the VCSEL mode cross correlations we systematically set Langevin noise sources to zero until cross correlations disappeared. Using these methods, we can establish that the main noise contributions which accounts for MPN and RIN come from the $F_{Sm}(t)$ terms of the laser rate equation. One can further conclude that MPN originates at the photon level, and that the carrier pool acts as a medium in which these photons interact, primarily through hole burning. If we approximate the photon Langevin noise term:

$$F_{Sm}(t) \approx \sqrt{\frac{\langle F_{S_m} F_{S_m} \rangle}{\Delta t}} \approx \sqrt{2\Gamma_{\mathrm{m}} \frac{v_{gm} G_m n_{spm}}{V_{pm} \Delta t} S_m} \tag{4.33}$$

We conclude that the photon Langevin noise sources are dependent on G_m and S_m. Since G_m can be directly controlled using laser rate equation parameters which are defined in

(4.5). As a reminder, the $1/(1+\sum_n \epsilon_{nm} S_n)$ term in (4.5) represents carrier heating and spectral hole burning which has been identified to be the primary cause of MPN [78].

Note that for now, we have made the following assumptions in our model: $V_{p1} = V_{p2} = V_{p3}$, and $\tau_{p1} = \tau_{p2} = \tau_{p3}$. We also use the same gain coefficient and population inversion factor for each mode. Here, we also assume that there is no interaction between the modes and therefore set $\epsilon_{mn}|_{m\neq n} = 0$. Since we have assumed no mode-to-mode interaction, we can set all $\epsilon_{mn}|_{m=n} = \epsilon$. We will later review these interactions when we focus on noise correlations. For now, these assumptions will allow us to have the same output power, frequency response and RIN spectrum from each mode.

4.2.4 Gain Compression Impact on Mode Noise Correlations

The 3-mode gain compression matrix is:

$$\epsilon_{mn} = \begin{bmatrix} \epsilon_{11} & \epsilon_{21} & \epsilon_{31} \\ \epsilon_{12} & \epsilon_{22} & \epsilon_{32} \\ \epsilon_{13} & \epsilon_{22} & \epsilon_{33} \end{bmatrix} \tag{4.34}$$

Where each row affects the gain of the nth mode. Here diagonal elements represent self-saturation, while nondiagonal elements represent cross-saturation. Setting non diagonal terms to zero, implies zero interaction or zero coupling between the modes via the photon reservoirs. Thus, we start with a diagonal gain compression matrix. In reality, the gain compression of one mode could affect the gain of another mode. For example in VCSELs, it has been shown that the overlap and hence the cross-saturation between adjacent modes is much greater than non-adjacent modes [2],[78] which leads to the recently measured positive mode noise correlations.

To ensure the overall VCSEL dynamics are unaltered, equation (4.5) must produce the same amount of gain before and after our transformation. If the power between all modes are equal a simple transformation such as

$$\epsilon_{mn} = \begin{bmatrix} \epsilon(1-x) & x\epsilon & 0 \\ x\epsilon & \epsilon(1-2x) & x\epsilon \\ 0 & x\epsilon & \epsilon(1-x) \end{bmatrix} \tag{4.35}$$

is sufficient. Here x is a value between 0 and 0.5 such that all elements remain non-negative.

While we do not claim that this is the only solution, (4.35) does have features which we would like to take advantage of. For one, this matrix is symmetric, meaning saturation in mode 1 due to mode 2 is the same as the saturation in mode 2 due to mode 1. Furthermore, all rows sum up to ϵ and therefore each mode experiences the same gain saturation before and after the transformation. For now, gain saturation factors ϵ_{13} and ϵ_{31} are set to zero indicating that there is little to no saturation between these non-adjacent modes. It should be noted that here mode 1 saturates itself and mode 2. Mode 2 saturates itself, mode 1 and mode 3. While mode 3 saturates itself and mode 2. Therefore, the saturation of mode 2 by mode 1 and 3 must be accounted for through the -$2x$ term in ϵ_{22}.

In these calculations ϵ is again set to $4\text{x}10^{-16}$. Figure 4.2a (4mA) and 4.3a (8mA) show the cross correlations when x = 0. Here, negative noise correlations are experienced between all mode noise combinations, which follows previously assumed behavior for the longitudinal modes found in edge emitting lasers. Figure 4.2b, c and Fig 4.3b, c shows the VCSELs cross correlations when the VCSEL experiences cross gain saturation. Here we

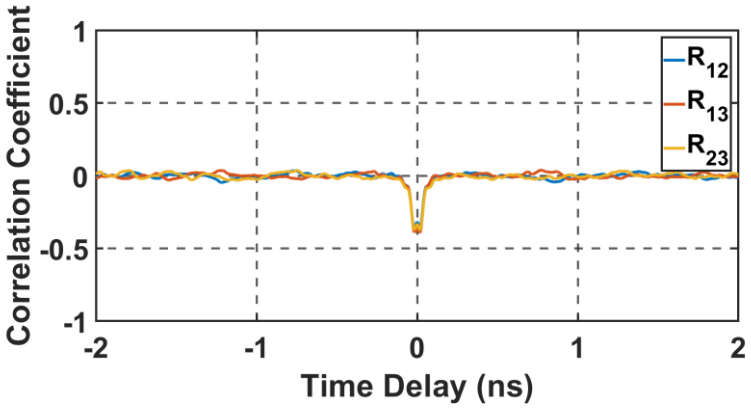

(a)

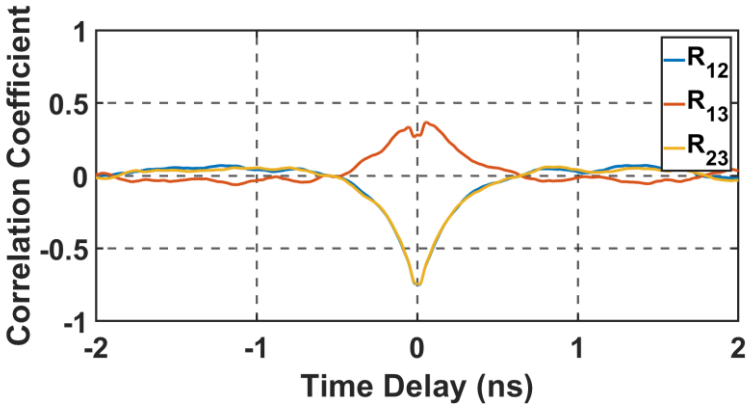

(b)

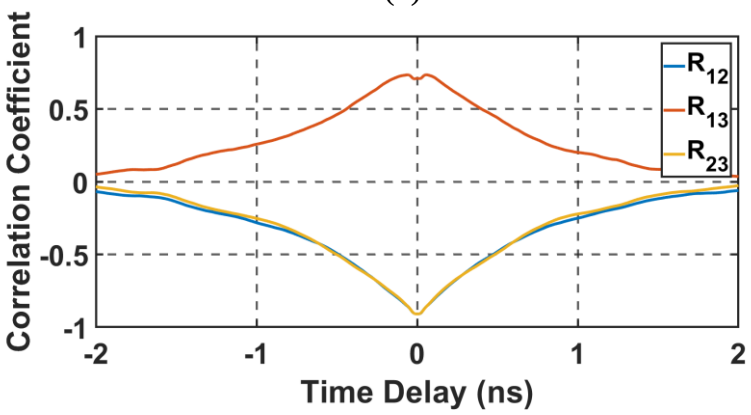

(c)

Figure 4. 2 Cross correlations at 4mA for a) x=0 b) x=0.28 c) x=0.32. The magnitude of the correlation coefficient and time correlation is seen to increase with increasing cross correlation.

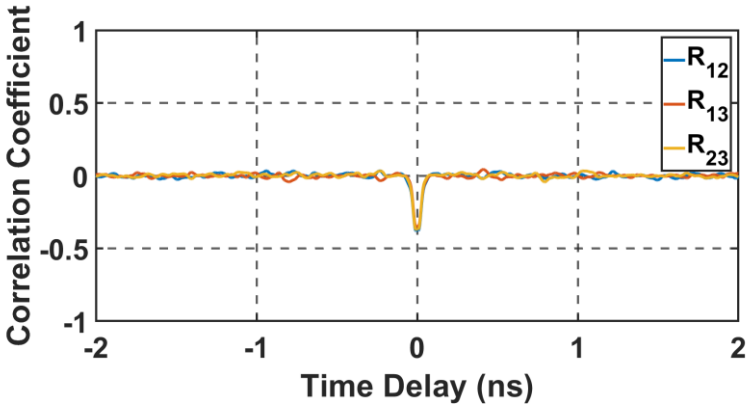

(a)

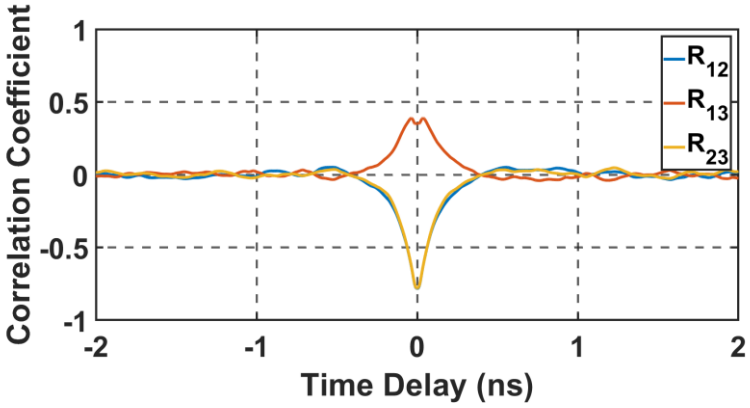

(b)

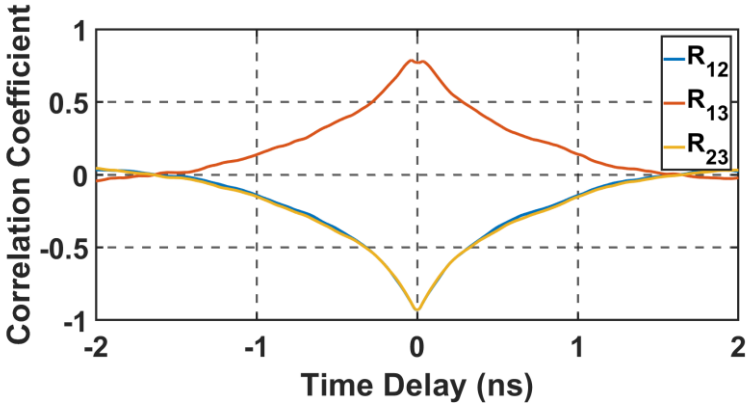

(c)

Figure 4. 3 Cross correlations at 8mA for a) x=0 b) x=0.28 c) x=0.32. The magnitude of the correlation coefficient and time correlation is seen to increase with increasing cross correlation.

see that the lack of cross saturation between modes 1 and 3, leads to a positive noise correlation between modes 1 and 3. As the mode experiences higher and higher gain saturation, the correlation time with other modes is increased. This can be explained by the

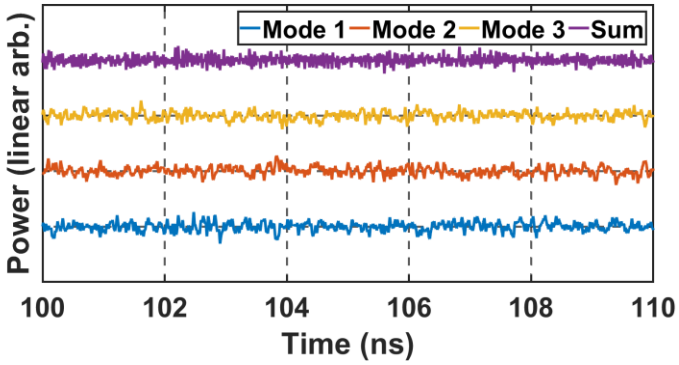

(a)

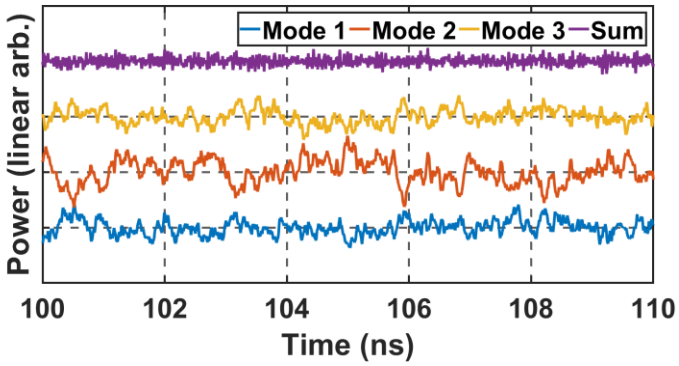

(b)

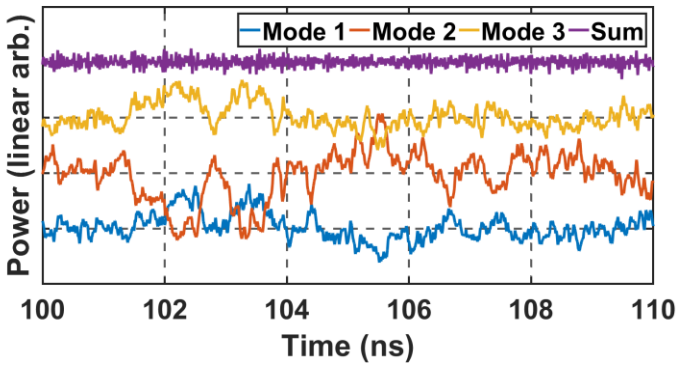

(c)

Figure 4. 4 Temporal output from stochastic rate equation at 8mA when a) x=0 b) x=0.28 c) x=0.32. Modes have been artificially shifted for clarity. Note that even though individual modes are noisy, as long as all power is captured, total noise in system is constant. Temporal output is taken starting after 100ns, long after any possible transient effects can take place.

fact that as the mode experiences more gain saturation it takes longer for the saturated mode to react to changes from other modes which elongates the correlation time. One can also note that the correlation times are longer at lower bias current conditions. This is likely due to the spontaneous emission into the lasing mode being a larger fraction of the total power at lower bias currents.

Since the main cause of gain saturation is the overlap in optical modes within the laser cavity, we have computed the overlap integrals between the LP_{01}, LP_{11} and LP_{21} modes which correspond to the first 3 transverse modes (modes 1, 2, 3 respectively) for a 6-micron VCSEL aperture. These overlaps, also known as coupling efficiency, are formulated as

$$\eta_c = \frac{|\int E_1^* E_2 dA|^2}{\int |E_1|^2 dA \int |E_2|^2 dA} \tag{4.36}$$

where, E_1 and E_2 are the complex electric fields of the optical mode.

Using (4.36) we found that the coupling efficiency between mode 1 and 2 to be 0.26, between mode 1 and 3 was found to be 0.04. and between mode 2 and 3 the coupling efficiency was 0.27. These values are similar to those plotted in Fig 4.2b, c and Fig 4.3 b, c. Therefore, a new gain compression matrix can be generated:

$$\epsilon_{mn} = \begin{bmatrix} 0.70\epsilon & 0.26(\bar{S_1}/\bar{S_2})\epsilon & 0.04(\bar{S_1}/\bar{S_3})\epsilon \\ 0.26(\bar{S_2}/\bar{S_1})\epsilon & 0.47\epsilon & 0.27(\bar{S_2}/\bar{S_3})\epsilon \\ 0.04(\bar{S_3}/\bar{S_1})\epsilon & 0.27(\bar{S_3}/\bar{S_2})\epsilon & 0.69\epsilon \end{bmatrix} \tag{4.37}$$

where the fractions $(\bar{S_1}/\bar{S_2})$, $(\bar{S_1}/\bar{S_3})$, … are steady state values for a given current and are used to account for the different photon densities encountered between modes. When all

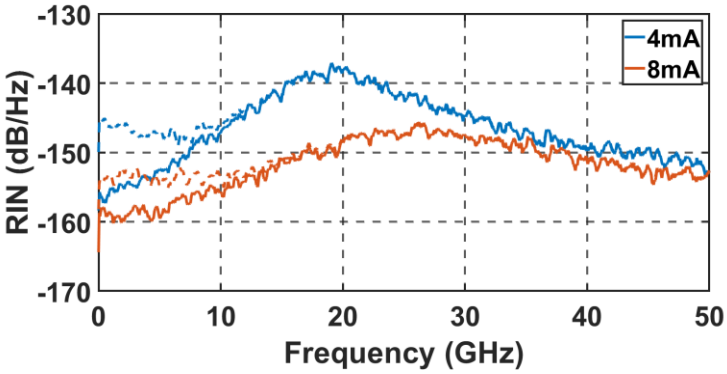

(a)

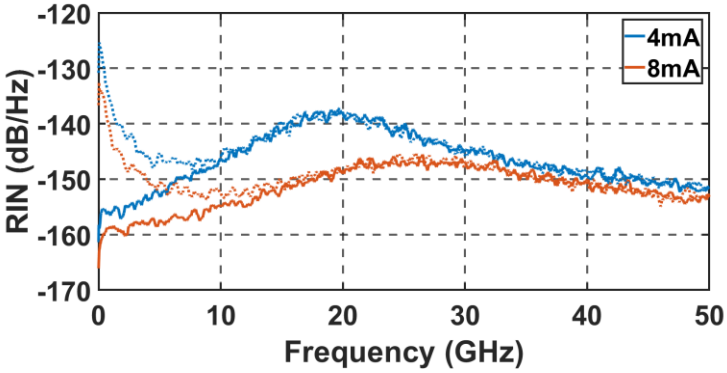

(b)

Figure 4. 5 RIN spectrum when no spatial filtering is present (-) and the same spatial filtering (- -) is applied. For the case of a) only negative mode noise correlations and b) positive/negative correlations. Both spatial filtering and positive and negative noise correlations between modes need to be present in order for it to cause near exponential RIN peaking at low frequencies as seen in (b). Therefore, these correlations must be included in existing models for accurate noise simulations.

modes have equal photon densities (4.37) simplifies to (4.35). Note that since we have assumed the VCSEL structure in (4.37). These values may have to be slightly tuned in order to accurately model the RIN spectrum after launching modes into the fiber for a given VCSEL.

4.3 Parameter Extraction for Multimode Laser Rate Equations

Parameter extraction using $H(\omega)$ has been done in the past [8-10]. Yet these models seldom go past a single mode. To the best of our knowledge this is the first-time parameter

Table 4. 2 VCSEL Parameters and Typical Values

Laser Parameters	**Bounds**	**VCSEL B**	**VCSEL C**
η_i (unitless)	0.5 – 1	0.75	0.96
$[\tau_{p1}, \tau_{p2}, \tau_{p3}] = \tau_p$ (ps)	1 – 8	3.96	4.95
g_o (cm^{-1}/s)	1x10^3 – 5x10^4	3.62x10^4	6.06x10^3
τ_n (ns)	1 – 5	1.95	1.41
N_s (cm^{-3})	1x10^{17} – 5x10^{18}	4.77x10^{18}	5.64x10^{17}
N_{tr} (cm^{-3})	1x10^{17} – 5x10^{18}	2.13x10^{18}	1.53x10^{18}
$[\epsilon_{11}, \epsilon_{22}, \epsilon_{33}] = \epsilon$ (cm^3)	1x10^{-19} – 1x10^{-15}	4.75x10^{-16}	3.61x10^{-17}
$[V_{p1}, V_{p2}, V_{p3}]$ (cm^3)	0.6x10^{-10} – 0.8x10^{-10}	[0.64,0.61,0.64] x10^{-10}	[0.62,0.61,0.62] x10^{-10}

extraction has been executed for three mode VCSEL. In addition, we use both small signal and noise characteristics to further improve our set of extracted parameters.

In this section we extract parameters using measurements of a multimode VCSEL from Nvidia (previously Mellanox) and a multimode VCSEL from Chalmers which we will refer to as VCSEL B and VCSEL C respectively. The Nvidia VCSEL under test is part of a 1x4 VCSEL array designed for use in high-speed data communication parallel applications. The 28Gbaud 850nm GaAs/InGaAs QW VCSELs were measured to have a bandwidth of ~26.5GHz at 9mA (Fig. 4.2a), with a measured thermal roll over near 13mA. More information about the Chalmers VCSEL can be found here [62].

Figure 4.8 shows the sequence of steps in our optimization approach which fits (19) and (29) to measured experimental data. Parameter extraction using a multimode model contains many more parameters than those of single mode models, making fitting both bandwidth and noise spectra difficult. Additionally, the increase in laser parameters

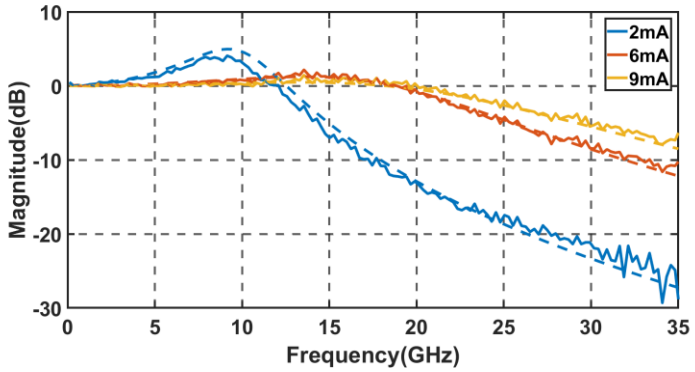

(a)

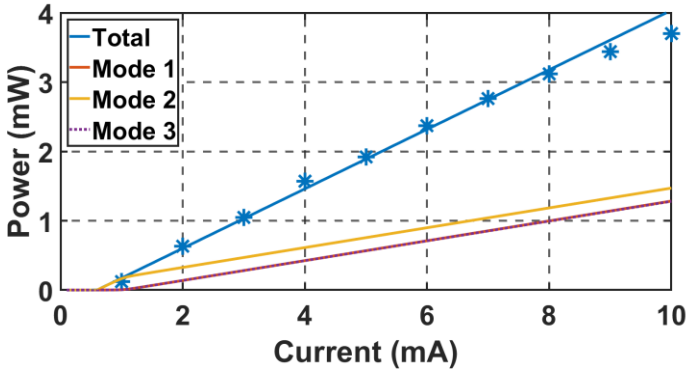

(b)

Figure 4. 6 VCSEL A: Comparison between measured (solid) and simulation (dotted) for b) LI curve, experimental data is shown as blue dots.

increases the already multiple local minima in the search space. This unfortunately reduces the probability of extracting meaningful laser parameters. For example, a very low photon lifetime can be compensated by a rather high photon volume. Both values might be extremes while still being able to fit to experimental data. Therefore, we must constrain certain parameters to find a set of parameters we can manage. Note that our parameter extraction method is a two-stage process. We initially use a global optimization technique to find multiple solutions in our search space, these solutions are constrained such that all photon lifetime, photon mode volumes and gain saturations are equal. We then remove these constraints and use a gradient decent approach optimization technique under a subset

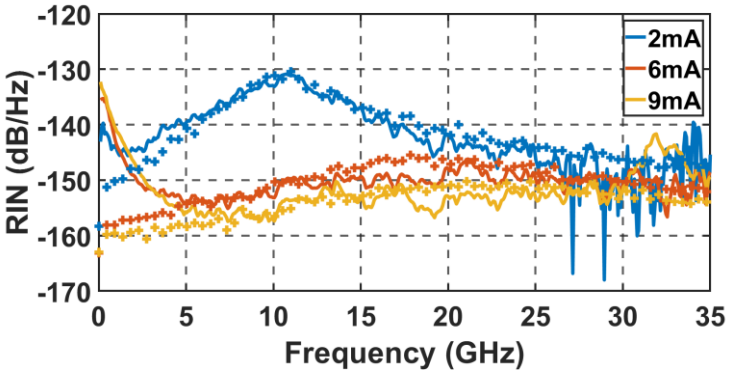

(a)

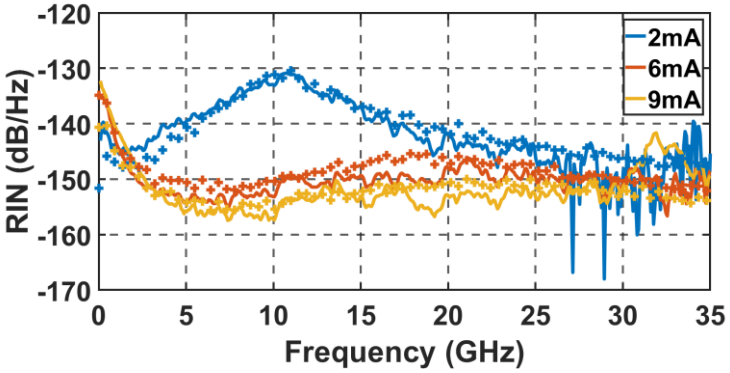

(b)

Figure 4. 7 VCSEL A: Comparison between measured (solid) and simulation (dotted) for a) RIN w/o spatial filtering b) RIN w/ spatial filtering and positive/negative correlations.

of acceptable solutions. This allows the optimization technique to better fit VCSEL parameters having slightly different photon lifetimes, and volumes.

The photon lifetime of all modes is assumed to be equal, $\tau_{p1}, \tau_{p2}, \tau_{p3} = \tau_p$ in stage 1 of the parameter extraction method because it largely depends on the physical structure of the laser. The small wavelength separation of transverse modes also allows us to assume that the group velocity and population inversion factor for all modes are the same in stage 1. Finally, in stage 1, of our parameter extraction methodology, we also assume that there is no interaction between the modes and therefore set $\epsilon_{mn}|_{m\neq n} = 0$. Since we have assumed no mode-to-mode interaction, we can set all $\epsilon_{mn}|_{m=n} = \epsilon$. In reality, the gain

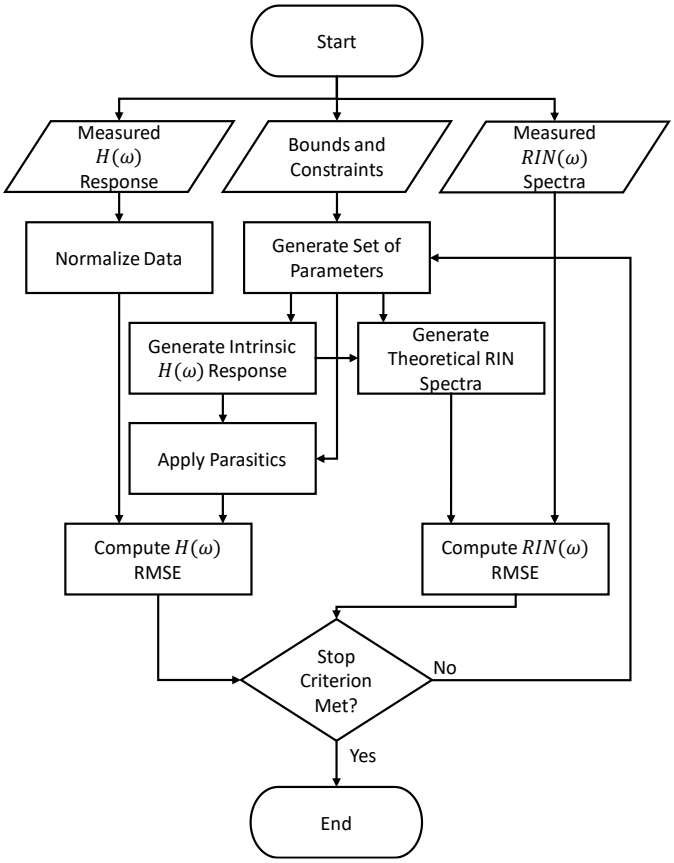

Figure 4. 8 Flowchart for parameter extraction using $H(\omega)$ and/or $RIN(\omega)$.

compression of one mode might affect the gain experienced by another mode (intermodal gain compression). Parameters to be optimized are all depicted in Table 4.2, along with their bounds and final set of extracted parameters. Note that using our assumptions, and by using existing literature, only 8 out of the 30 laser parameters are required for optimization.

4.3.1 Parameter Extraction Results

Our extraction method was applied on 2 different VCSELs. Figure 4.6a and 4.7a shows agreement between simulated and experimental BW and RIN data for VCSEL B. Our simulation agrees with our experimental data for Fig 4.6a at all frequencies measured. Yet, there still seems to be a large discrepancy at low frequencies in our RIN simulations, Fig

4.7a. It should be noted that the experimental RIN is higher at lower frequencies due to mode partition noise (MPN) and spatial filtering which are yet to been accounted for in this model. We assume that spatial filtering primarily occurs when the higher order VCSEL modes couple into the fiber. The total coupling efficiency between the VCSEL and fiber modes is generally around 90%. We mimic this by scaling the output power of the 3rd mode by some factor k. To effectively decrease the total power of the VCSEL by 90% we have had to scale down the power in the 3rd mode by 30%. Figure 4.7c depicts the frequency response after this spatial filtering has been accounted for. We would like to note that this change would also affect the small signal response of the VCSELs but in our simulations it shifted the magnitude of the small frequency response down by 0.1 dB at 4mA and 0.04 dB at 8mA. This is still well within any measurement error.

Figure 4.6db shows the light-current curve for VCSEL B. After extraction is complete, we can extract η_o= 0.39 for a differential quantum efficiency of 0.29, which is well within the range supported by literature [23]. This equation is:

$$\eta_d = \eta_i \eta_o = \frac{q}{hv} \frac{dP_{total}}{dI} \tag{4.38}$$

where P_{total} is the sum all modes.

An identical process was used to match the simulated and experimental data for VCSEL C. Figure 4.9 shows these results. The low frequency mismatch in RIN can be corrected by accounting for spatial filtering using the same method as for VCSEL B.

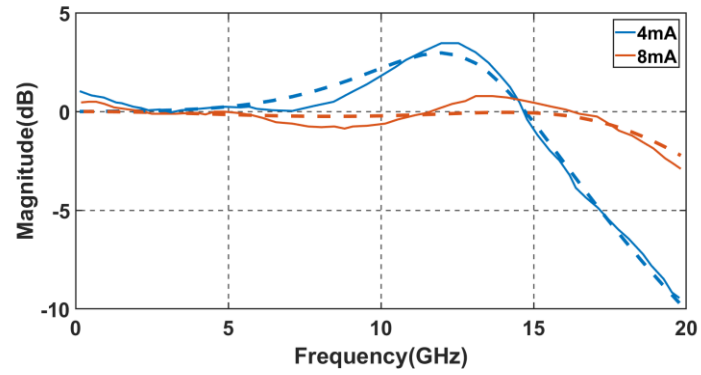

(a)

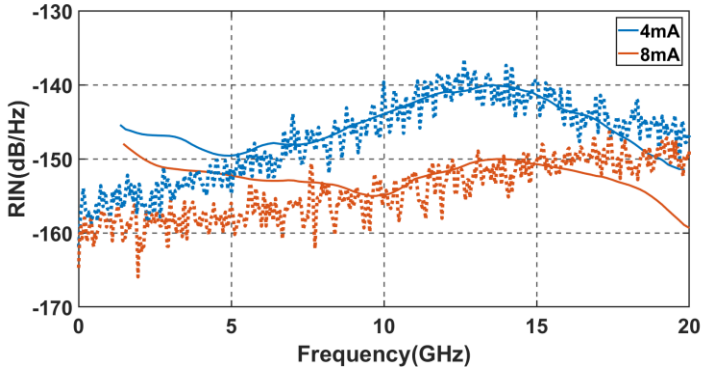

(b)

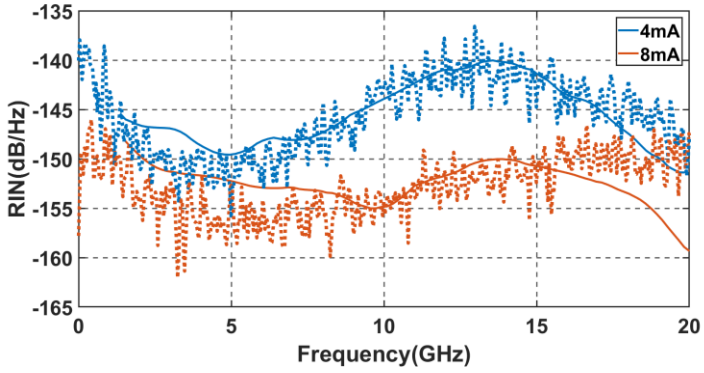

(c)

Figure 4. 9 VCSEL C: Comparison between measured (solid) and simulation (dotted) for a) small signal frequency response b) RIN w/o spatial filtering c) RIN w/ spatial filtering.

4.4 Spatially Independent VCSEL Rate Equations

While the rate equations introduced in section 4.1 can handle a wide range of VCSEL structures, they lack the inherent mode shapes of the multimode VCSEL. To achieve greater accuracy especially when launching light through fiber, the model should account for the spatial characteristics of high speed VCSELs, specifically the transverse mode operation and spatial hole burning. As detailed in previous sections, spatial hole burning effects have a large influence on the characteristics of semiconductor lasers. This is in due in part by carrier density depletion at locations where the mode intensity is large. This effect reduces the gain distribution for the lasing mode causing an increase in threshold gain. While many comprehensive spatially dependent VCSEL models exist, they tend to be computationally expensive. This makes spatially dependent laser models unsuitable for link level simulations that require many symbols for accurate noise and ISI assessment.

In this section we present a spatially dependent VCSEL model and parameter extraction technique that accounts for spatial effects such as hole burning and the associated mode competition. This model is capable of supporting multiple transverse modes, while making simplifying assumptions for the carrier and mode profiles. This allows for an accurate model that can be used in the design and simulations of optical links. We validate the robustness of our extraction technique using VCSELs from different manufacturers. We note that RIN can be added in a straightforward fashion as we have previously shown. This would allow accurate simulation of RIN dependence on VCSEL modal decorrelations.

The rate equations used here are a modified version of those described in [18]:

$$\frac{dN_0}{dt} = \frac{\eta_i I_o}{q} - \frac{N_0}{\tau_n} - \sum_k G_{k,N_0} S_k - \frac{I_l}{q} \tag{4.39}$$

$$\frac{dN_j}{dt} = \frac{-\eta_i I_o}{q}\zeta_j - \frac{N_j}{\tau_n}(1 + h_j) - \sum_k G_{k,N_j} S_k \tag{4.40}$$

$$\frac{dS_k}{dt} = -\frac{S_k}{\tau_{pk}} + \frac{\beta_k}{\tau_n}\left[b_0 N_0 - \sum_{i=0}^{\infty} b_i N_i \right] + G_{k,S_k} S_k \tag{4.41}$$

gain is defined by:

$$G_{k,X} = \frac{G_0\left[A_{k,X} N_0 - B_{k,X} N_1 - C_{k,X} N_2 - A_{k,X} N_t\right]}{1 + \sum_m \varepsilon_{\mathrm{km}} S_m} \tag{4.42}$$

Where N_o is a measure of the average carrier profile, N_j for $j = 1,2$ captures the spatial hole burning effects, and S_k for $k = 1,2$ describes the number of photons in the 1st and 2nd mode. These equations do not explicitly demonstrate spatial dependence. However, the parameters ($A_{k,X}, B_{k,X}, C_{k,X}, b_i, h_j$ and ζ_j) implicitly account for the VCSEL's spatial dependence. The parameters $A_{k,X}, B_{k,X}, C_{k,X}$ are the overlap integrals between the gain profiles and VCSEL transverse mode profiles. We assume LP mode shapes for the VCSEL transverse mode profiles.

$$\begin{bmatrix} j\omega+\gamma_{N_0N_0} & -\gamma_{N_0N_1} & -\gamma_{N_0N_2} & \gamma_{N_0S_1} & \gamma_{N_0S_2} \\ -\gamma_{N_1N_0} & j\omega+\gamma_{N_1N_1} & \gamma_{N_1N_2} & -\gamma_{N_0S_1} & -\gamma_{N_1S_2} \\ -\gamma_{N_2N_0} & \gamma_{N_2N_1} & j\omega+\gamma_{N_2N_2} & -\gamma_{N_2S_1} & -\gamma_{N_2S_2} \\ -\gamma_{S_1N_0} & \gamma_{S_1N_1} & \gamma_{S_1N_2} & j\omega+\gamma_{S_1S_1} & \gamma_{S_1S_2} \\ -\gamma_{S_2N_0} & \gamma_{S_2N_1} & \gamma_{S_2N_2} & \gamma_{S_2S_1} & j\omega+\gamma_{S_2S_2} \end{bmatrix} \begin{bmatrix} N_0' \\ N_1' \\ N_2' \\ S_1' \\ S_2' \end{bmatrix} = \frac{\eta_i I_0'}{q} \begin{bmatrix} 1 \\ -\zeta_1 \\ -\zeta_2 \\ 0 \\ 0 \end{bmatrix} \tag{4.43}$$

The modulation response of the individual modes is found by solving Eqn. (4.43) as a system of linear equations and obtaining the small signal photon spectral densities $S_1'(\omega)$ and $S_2'(\omega)$. Note that each γ_{XX} found in Eqn (4.43) is obtained by linearizing the differential rate equations and computing the coefficients of $N_o', N_1', N_2', S_1', S_2'$ in terms of the laser rate parameters as well as the steady state current, carrier, and photon values. These values are unique to the rate equation used.

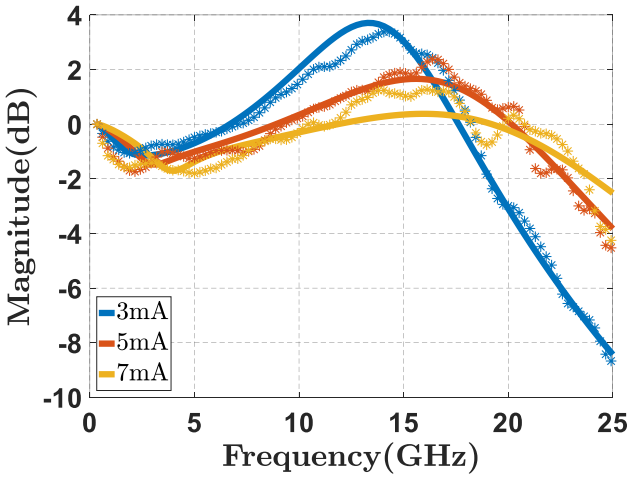

(a)

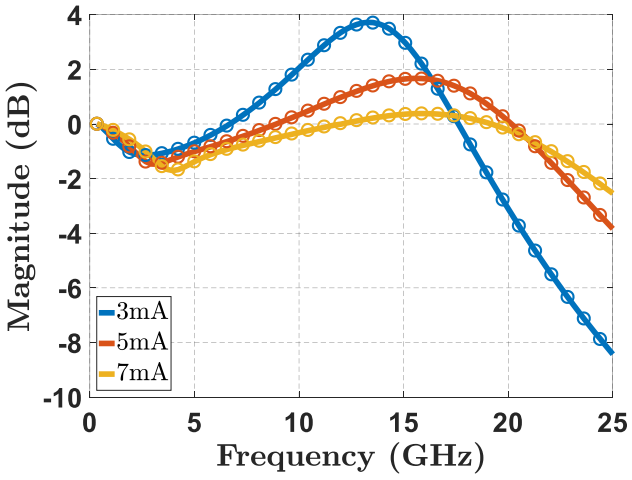

(b)

Figure 4. 10 Frequency Response Curves for VCSEL D, experimental data was captured in our lab (a) Experimental $(*)$ vs. Theoretical linearized $(-)$ response (b) Theoretical linearized $(-)$ vs. Simulated (o) response

Table 4. 3 VCSEL Parameters

Description	**VCSEL D**	**VCSEL E**
Injection efficiency,η_i	1	1
Spont. emission factors,$[\beta_1, \beta_2]$	[1x10^{-3},5x10^{-2}]	[10.57x10^{-3},1x10^{-3}]
Carrier lifetime (ns),τ_n	2.2	0.5
Photon lifetime (ps),$[\tau_{p1}\ \tau_{p2}]$	[1,1]	[4.1,3.6]
Gain (s^{-1}),G_0	4.2x10^5	4.4x10^5
Gain sat.,$[\varepsilon_{11}, \varepsilon_{12}, \varepsilon_{21}, \varepsilon_{22}]$ x10^{-6}	[20,2.2,20,1.9]	[0.5,3.08,2.9,5.0]
Precomputed values		
Current distribution,$[\zeta_1, \zeta_2]$	[0,0]	[0,0]
Diffusion factors,$[h_1, h_2]$	[5.0,16.76]	[5.0,16.76]
Int. spont. emission,$[b_0, b_1, b_2]$	[1,0,0]	[1,0,0]
$[A_{1,N_0} B_{1,N_0} C_{1,N_0}]; [A_{2,N_0} B_{2,N_0} C_{2,N_0}]$	[1,0.37,-0.0018];[1,0.12,-0.16]	
$[A_{1,N_1} B_{1,N_1} C_{1,N_1}]; [A_{2,N_1} B_{2,N_1} C_{2,N_1}]$	[2.34,1.81,0.62];[0.76,0.77,-0.085]	
$[A_{1,N_2} B_{1,N_2} C_{1,N_2}]; [A_{2,N_2} B_{2,N_2} C_{2,N_2}]$	[-0.028,1.125,1.704];[-1.83,-0.15,0.948]	
$[A_{1,S_1} B_{1,S_1} C_{1,S_1}]$	[1,0.37,-0.0018]	
$[A_{2,S_2} B_{2,S_2} C_{2,S_2}]$	[1,0.12,-0.16]	

The composite frequency response is:

$$H_{total}(\omega) = \left| \frac{S_1'(\omega) + S_2'(\omega)}{S_1'(0) + S_2'(0)} \right| \tag{4.44}$$

$H_{total}(\omega)$ is iteratively optimized using the MMSE algorithm to obtain a close match with the measured data for multiple bias points simultaneously. Table 4.3 lists the rate equation parameters extracted by our technique for two example VCSELs.

Figure 4. 10a depicts the frequency response of the linearized VCSEL rate equations using the extracted parameters of Table 4.3. Results closely match the experimentally measured frequency response. Figure 4.11 shows a possible configuration of the

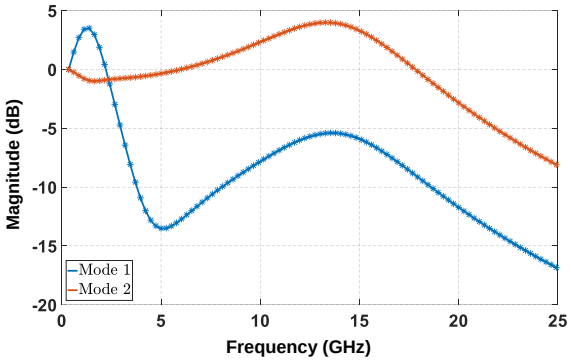

(a)

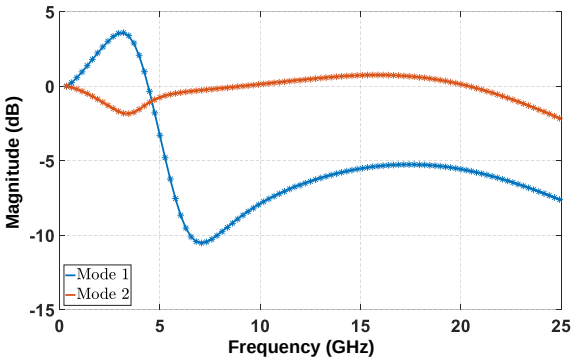

(b)

Figure 4. 11 Normalized frequency response for each mode at (a) 3mA and (b) 7mA

normalized frequency response for the each VCSEL mode. We then employed these extracted parameters in the differential VCSEL rate equations. Figure 4.10b shows that the frequency response obtained from the differential VCSEL rate equations agrees with that

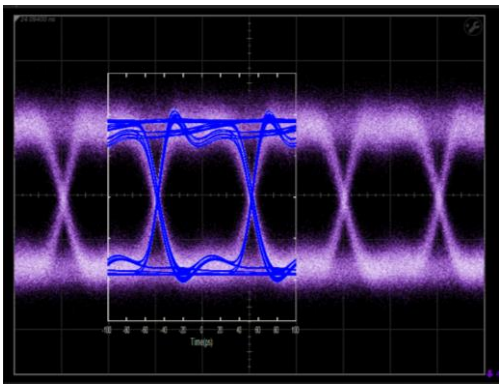

(a)

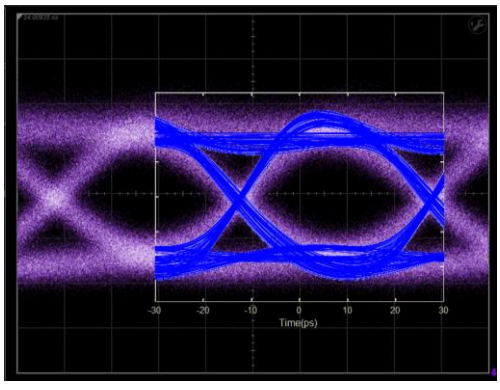

(b)

Figure 4. 12 Experimentally measured (purple) and simulated (blue) (a) 10G PRBS-7 eye diagram and (b) 25G PRBS-7 eye diagram using a single set of rate equation parameters.

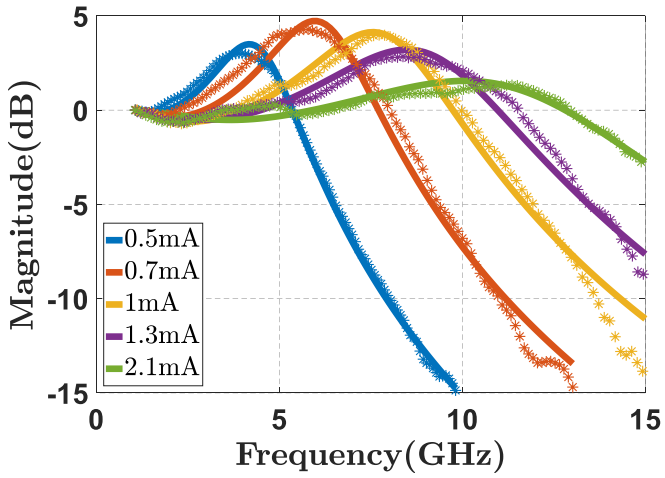

Figure 4. 13 Experimental (∗) vs. Simulated (−) response for VCSEL E at multiple bias currents

obtained from the linearized VCSEL rate equations. Figures 4.12a and 4.12b show that our parameter extraction technique accurately reproduces experimentally measured eye diagrams.

In order to show the robustness of our parameter extraction technique we employed it on frequency response data of a VCSEL found in literature. Results are depicted in Fig. 4.13 and show considerable improvement when compared to the single mode case depicted in Fig. 3.6.

CHAPTER 5

CHARACTERIZATION AND SIMULATION OF HIGH SPEED VCSEL OPTICAL LINKS

As the need for bandwidth increases in short range optical communications, the need for fast, and cost-effective solutions has become more apparent. Electrical signaling has rapidly been replaced by optical means. Optics is ever replacing many electrical links, as cost, power dissipation and space become more important. Low-cost vertical cavity surface emitting lasers (VCSELs) and multimode fiber (MMF) optimized for the 850 nm wavelength is used in many of the short reach links today. These fibers are designed to reduce the impact of intersymbol interference (ISI) and therefore help extend both reach and speed in our system. Most commercial products available on the market today are 1-10Gbps links with 25, 50 and 100Gbps VCSEL based interconnects becoming widely available. With increasing bitrates, an OOK non-return-to-zero (NRZ) modulation is severely limited by the spread of a signal in time because the propagation of the optical signal through the fiber is not the same for all modes. As we begin to push VCSEL bandwidths over 30GHz, it is clear that smaller VCSEL apertures are needed. These small aperture VCSELs generally lase in only 3 modes and are more resilient to fiber modal effects. Unfortunately, they generally output less power, which is needed when pushing towards 100G error free PAM-2 links.

Another proposed way is through pulse amplitude modulation (PAM). Modulation formats such as subcarrier modulation are possible, but the complexity of the modulator, demodulator and laser driver add higher cost and higher power consumption which is

highly undesirable in tightly packed data centers [2]. PAM-4 not only increases spectral efficiency but offers low complexity when compared to other multilevel modulation formats. Previous chapters established models and parameter extraction algorithms. These models are capable of extracting parameters that conform to both noise and bandwidth measurements. The next logical step would be to test these models against optical link experiments. Higher modulation formats like PAM4 reduce VCSEL bandwidth requirements but have greater sensitivity to RIN. Today's communication standards include the use of error correction in order to operate error free at higher BER standards. This is where our model would be useful. Higher VCSEL speeds and modulation formats require some form of pre compensation or channel equalization. A VCSEL model needs the flexibility of being able to cater to these types of systems while being flexible and simple enough to be integrated in system level models. In this chapter we test our models against experimental results and propose possible methods to achieve higher baudrates.

5.1 Characterization of Optical and Electrical Components

For assessment of VCSEL intrinsic and extrinsic performance, accurate VCSEL characterization procedures are required. In this section we will discuss the experimental procedures, including the test setup required to generate accurate S-parameter characterization of electrical and optical components. Furthermore, our RIN measurement setup will be described. Many measurements are characterized through more than one method, to verify accuracy and establish possible measurement uncertainties and limitations. These measurements will then be used for accurate replication of PAM-2 and PAM-4 eye diagrams.

5.1.1 O/E Characterization

While many models simply model optical detector/receivers as a low pass filter, fasters data rates and the move to PAM-4 require accurate characterization of the O/E bandwidth. For accurate characterization of the O/E bandwidth two setups as shown in Fig 5.1 were constructed. Figure 5.1a depicts Setup #1 which measured the O/E response using an Agilent 8517B VNA, an 852nm single frequency laser, and an EOSpace 40GHz MZM. In Setup #2 the O/E was characterized by a Keysight AWG (M8196A) and Scope (Keysight DCA-X) pair. Figure 5.1b depicts Setup #2, here we first measured the electrical channel

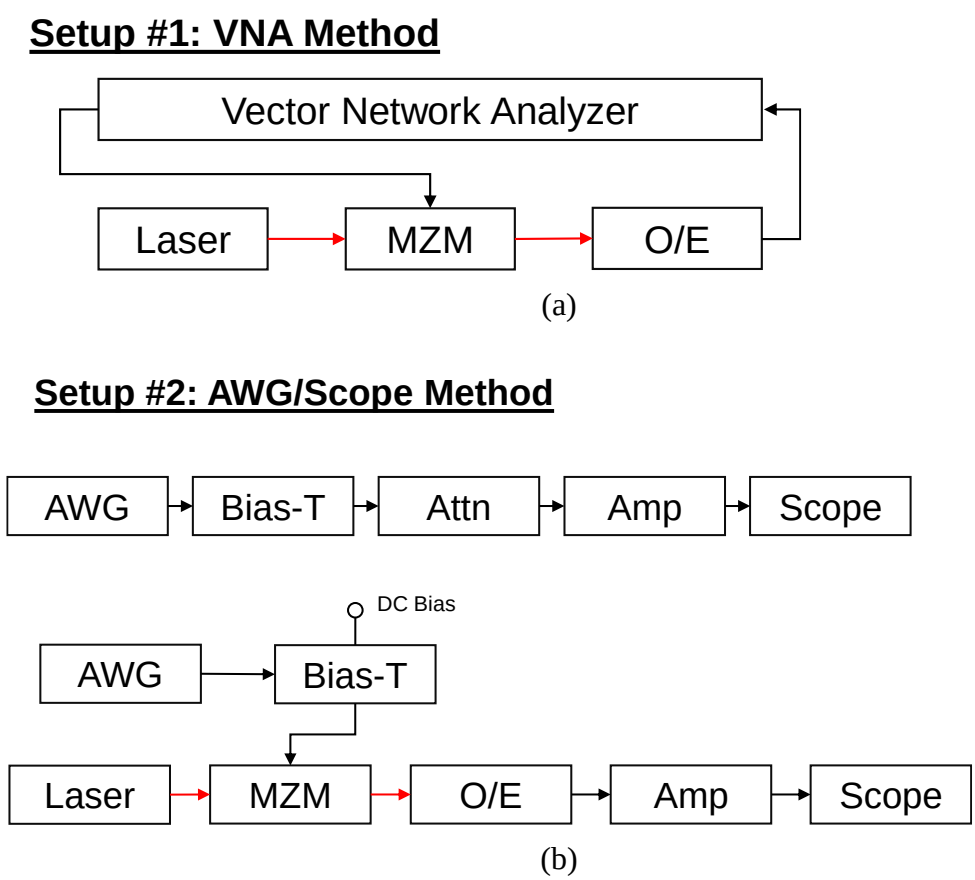

Figure 5. 1 Setups used to measure small signal frequency response of O/E components using (a) VNA and (b) AWG/Scope pair. Optical paths depicted in red. Electrical paths depicted in black.

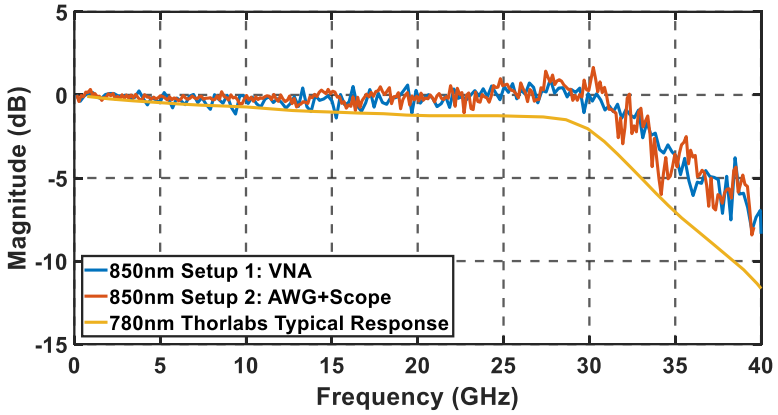

Figure 5. 2 Small signal frequency response measurement results using the VNA and AWG/Scope Pair. Both measurements are self-consistent. Use of the typical response will lead to overcompensation of link impairments and introduce effects that are inherent to the intrinsic or extrinsic VCSEL response.

components which consist of the Bias-T, and Amp. The optical components were then inserted into the link after the Bias-T. The response of the initially measured electrical channel was removed. Note that in setup #2 the higher noise floor of the scope requires the use of an amp after the photodiode. A 10dB 60Ghz attenuator was placed before the amp to stay within the scope's maximum peak to peak voltage. Results for the O/E is shown in Fig 5.2. As shown, the performance for both O/E components is higher than the typical performance. Figure 5.2 also shows that that both methods are consistent with each other.

5.1.2 S-Parameter Experimental Setup

After accurate measurement of all electrical and optical components in our system, we were now able to accurately extract the VCSEL's extrinsic frequency response. We note that

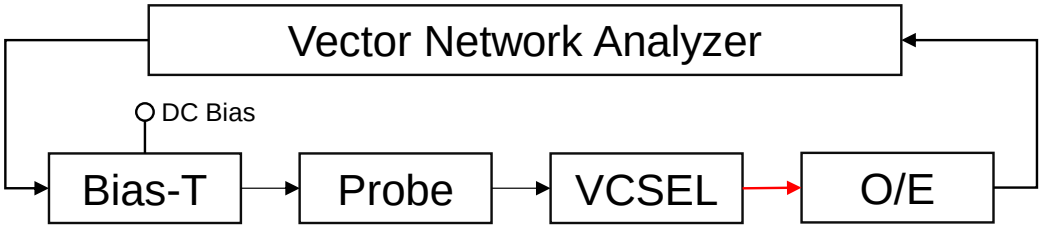

Figure 5. 3 Test setup for measurement of VCSEL scattering parameters

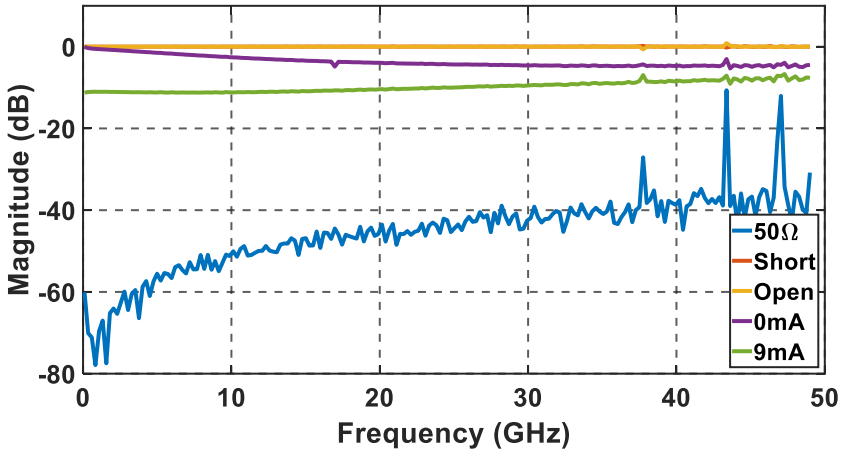

(a)

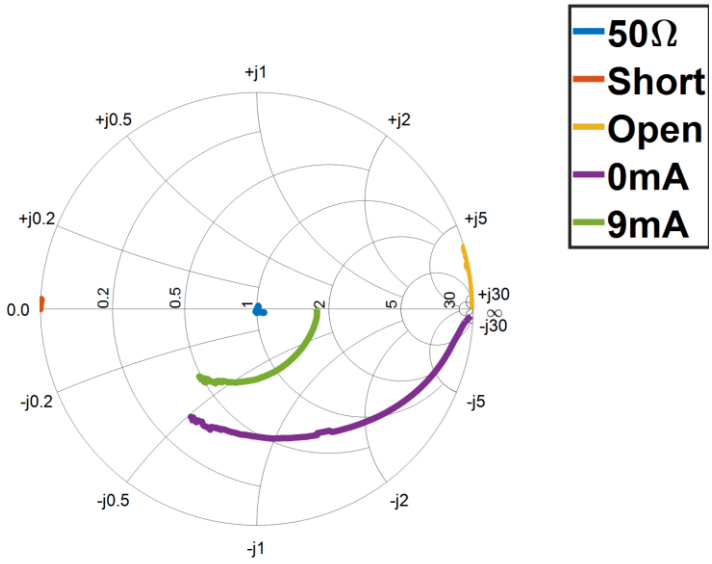

(b)

Figure 5. 4 S_{11} calibration measurements represented in (a) magnitude/cartesian and (b) Smith Chart/polar format. 50Ω load represented as a center dot in the smith chart corresponds to almost no reflections in the magnitude response. Spikes in the magnitude response at frequencies over 40GHz are systematic errors which are difficult to remove and must be corrected when analysing data

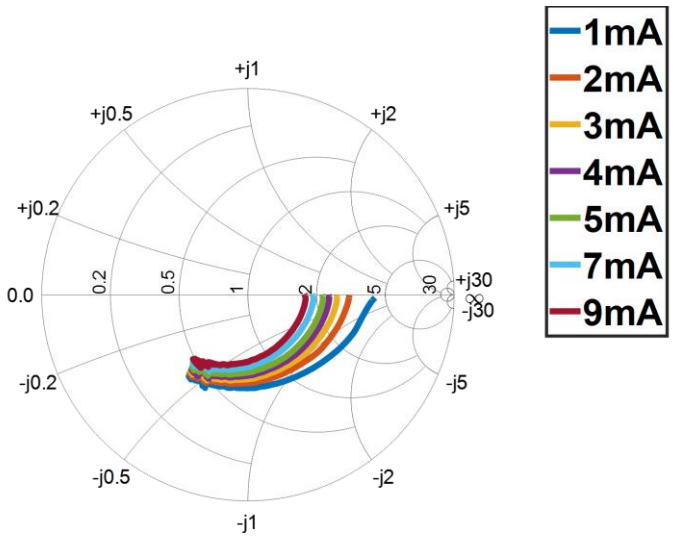

Figure 5. 5 S_{11} response for VCSEL bias of 1-10mA. Frequency response taken from 100MHz – 49.9GHz. Smith chart is normalized to 50Ω. At lower frequencies impedance is real, at higher frequencies capacitance effects from the junction dominate pushing response into the capacitive region.

here we differentiate between the VCSEL's extrinsic response which includes parasitics and the VCSEL's intrinsic response which does not. Figure 5.3 depicts our VCSEL S-parameter setup. By calibrating both the S_{11} and S_{21} which is important to reduce systematic errors we can capture both the small signal frequency response and the reflection coefficients at multiple bias currents, which is necessary for accurate laser parameter extraction and simulation. Small signal frequency response measurements using this setup have already been shown in Fig 4.8 and 4.11. Though a major source of bandwidth limitations is captured by modelling the small signal frequency response, it has been well established that a major source of extrinsic bandwidth limitations arises from the parasitics caused by the capacitance and resistance from the Bragg mirrors, the oxide layer and the active area. Therefore, it is of upmost important to capture the VCSEL's S_{11} response to extract the parasitic response. This not only allows for better extraction of laser rate equation parameters. For one, the parasitic VCSEL response is no longer assumed to be a

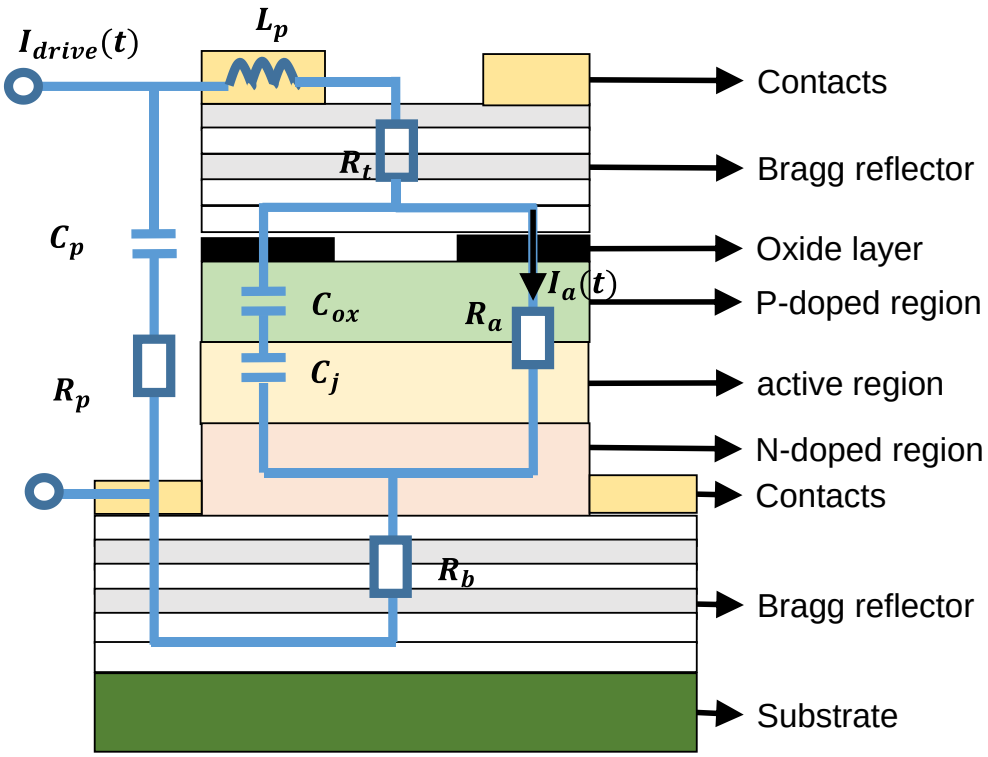

Figure 5. 6 Parasitic circuit chosen to model S_{11} response. Here C_p is the shunt capacitance due to capacitance build up between contacts, R_p is the shunt resistance due to the contact pad loss. L_p is due to inductance from contacts. R_m is resistance due to the top and bottom Bragg mirrors such that $R_m = R_t + R_b$. Here, R_a is the resistance of active region and C_a models the oxide layer and active layer capacitance such that $C_a^{-1} = C_{ox}^{-1} + C_j^{-1}$.

simple 1st order lowpass filter. Secondly, the parasitics allow the end user important knowledge into how parasitics can be minimized and therefore insight into methods that can reduce such parasitics.

Figure 5.4 shows our initial calibration results which represent the S_{11} parameter as the magnitude of the reflection coefficient in dB and the more commonly known smith chart. From the smith chart we can clearly tell the S_{11} calibration was successful as the short and 50Ω are represented as dots in their respective places. The open circuit here is shown as an arc due to the nonlinear fringing capacitance, electrical length differences and ration loss which are difficult to characterize. Furthermore, two S_{11} VCSEL bias currents

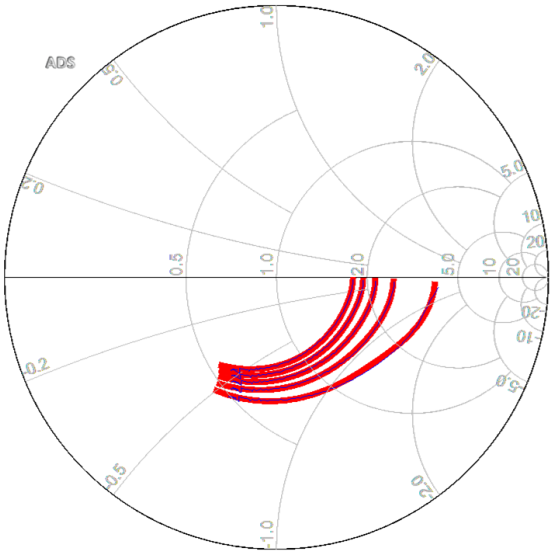

Figure 5. 7 Results of simulated S_{11} response (red) and measured S_{11} response (thin blue) from 1mA – 9mA in 2mA steps. S_{11} response is well characterized by circuit depicted in Fig 5.6.

spanning from 100MHz to 49.9GHz are shown as reference. The fully measured S_{11} response curves for bias current 1-9mA are shown in Fig 5.5.

For extraction of parasitic circuit elements from the measured S_{11} response, a parasitic circuit model must be chosen and fitted to the complex S_{11} response. Here we chose the parasitic circuit depicted in Fig 5.6, based on [83] with an extra shunt resistor as depicted in [84]. Keysight Advanced System Design (ADS) was chosen to model the following circuit and a gradient based decent algorithm was chosen to extract circuit parameters from the measured S_{11} response. Since most high speed VCSELs today are multi-quantum well oxide confined VCSEL, they can be largely represented by a single parasitic structure. In this circuit the top and bottom Bragg reflectors are modeled by R_m.

After parameter extraction of parasitic elements, the active region current used for VCSEL laser rate equations can be expressed in terms of circuit parameters such that:

$$I_a(t) = \frac{I_d e^{j\omega t} Z_{in}}{R_a + R_m - \omega^2 L_p C_a R_a + j\omega\left(C_a R_a R_m + L_p\right)} \tag{5.1}$$

Here, $I_a(t)$ is the time varying current flowing through R_a and I_d is the time varying input drive current. If working with voltages the voltage source is assumed to have a series resistance of 50 Ω. The input impedance is:

$$Z_{in}(\omega) = \left[\left(\frac{1}{j\omega C_p} + R_p\right)^{-1} + \left(j\omega L_p + R_m + \frac{1}{j\omega C_a + 1/R_a}\right)^{-1}\right]^{-1} \tag{5.2}$$

The S_{11} response, otherwise known as the reflection coefficient Γ, is calculated by:

$$\Gamma = \frac{Z_{in} - Z_0}{Z_{in} + Z_0}$$

Furthermore, since VCSEL parasitics change as the laser cavity, and Bragg mirrors heat up, it is important to capture these effects at multiple bias currents to determine bias/thermal dependent parasitic effects. This model in conjunction with the laser rate equation model would create a comprehensive VCSEL model able to simulate the extrinsic and intrinsic properties of a large number of semiconductor lasers.

By setting $t = 0$ and dividing (5.1) by I_d we plot the small signal frequency response of the parasitic circuit such that:

$$H(\omega) = \frac{I_a}{I_d} = \frac{Z_{in}}{R_a + R_m - \omega^2 L_p C_a R_a + j\omega\left(C_a R_a R_m + L_p\right)} \tag{5.3}$$

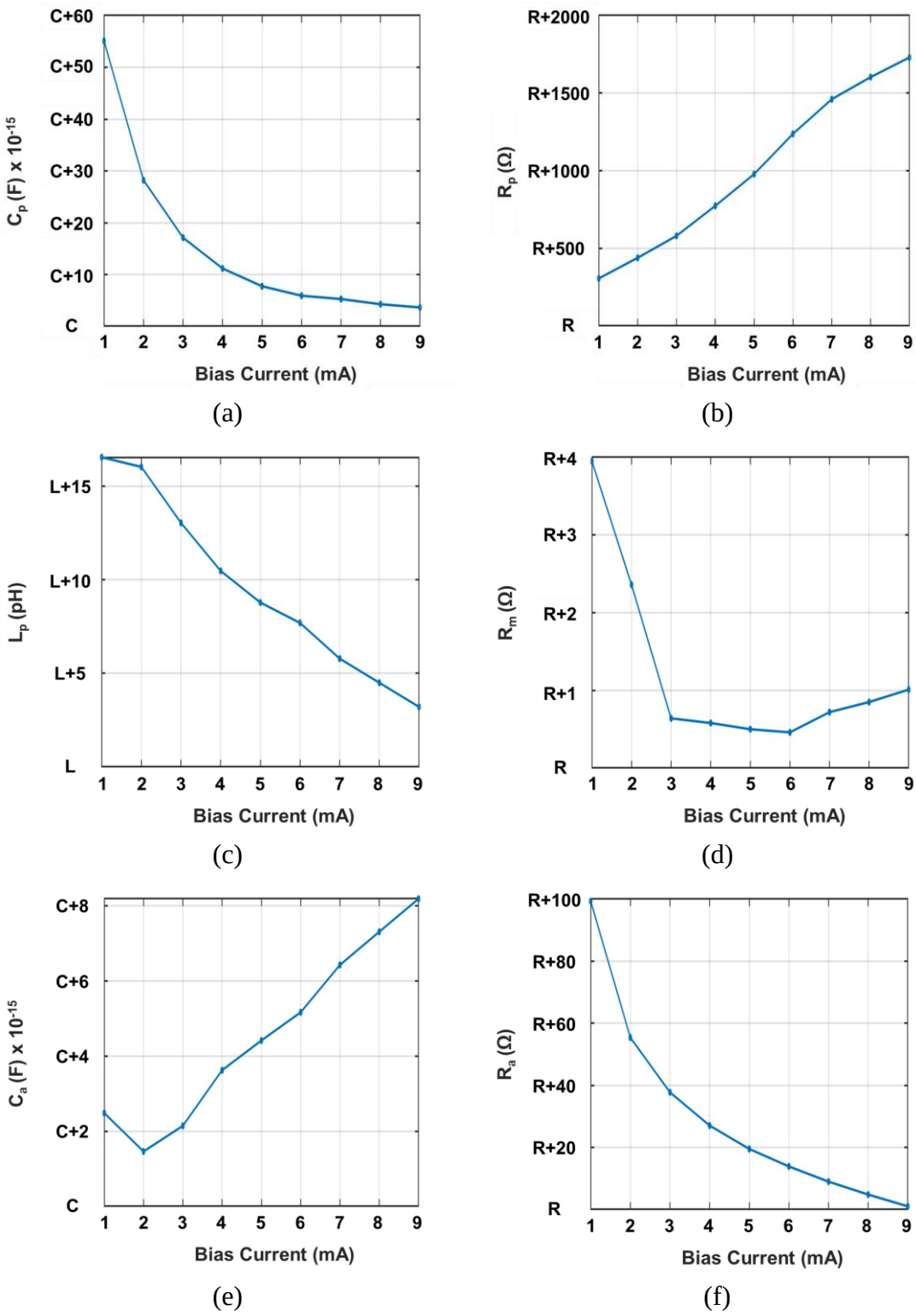

Figure 5. 8 Parasitic circuit parameter extraction results. Highly bias/temperature dependent parasitics can be easily identified from plots. These variations are highly correlated to the parasitic frequencies extracted from our rate equation models from Chapters 3 and 4.

Figure 5.7 shows the results of our parasitic circuit parameter extraction for currents between 1mA to 9mA and frequencies spanning from 100MHz to 40GHz. Figure 5.8 shows the range of extracted values. We note that the smith chart shows that VCSEL's characteristic impedance at low frequencies is real. This impedance includes the resistance of the metal contacts, Bragg mirrors, and p-n junction. As frequencies increase the junction capacitance and the curves move toward the capacitance region of the Smith chart, this increases capacitance in the junction which eventually dominates and leads to reduced junction impedance. The bias dependence of impedance changes the effective amplitude of the PAM-4 current applied to the active region, while the frequency dependence of the impedance results in filtering effects, especially at low bias currents.

Figure 5.8 shows the variations of the parasitic elements extracted from our circuit. While these trends have been widely shown, it is important to note the general magnitude

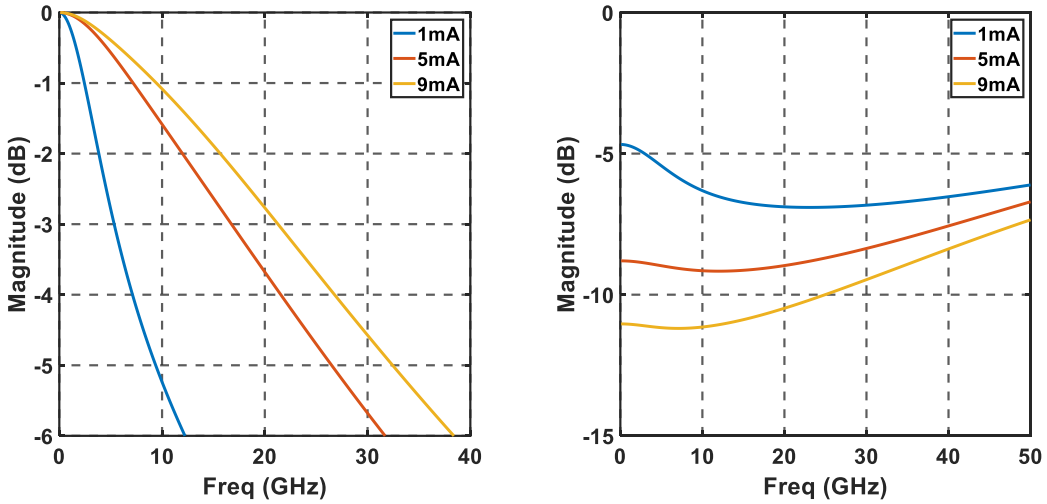

(a) (b)

Figure 5. 9 (a) Parasitic frequency response and (b) return loss magnitude at 1, 5 and 9mA using extracted parasitic circuit parameters. As bias currents increase parasitic limitations decrease and return loss improves. The parasitic bandwidth has a 3-dB bandwidth of around 20GHz further emphasizing the need for reduction of parasitic elements in order to improve VCSEL bandwidth response.

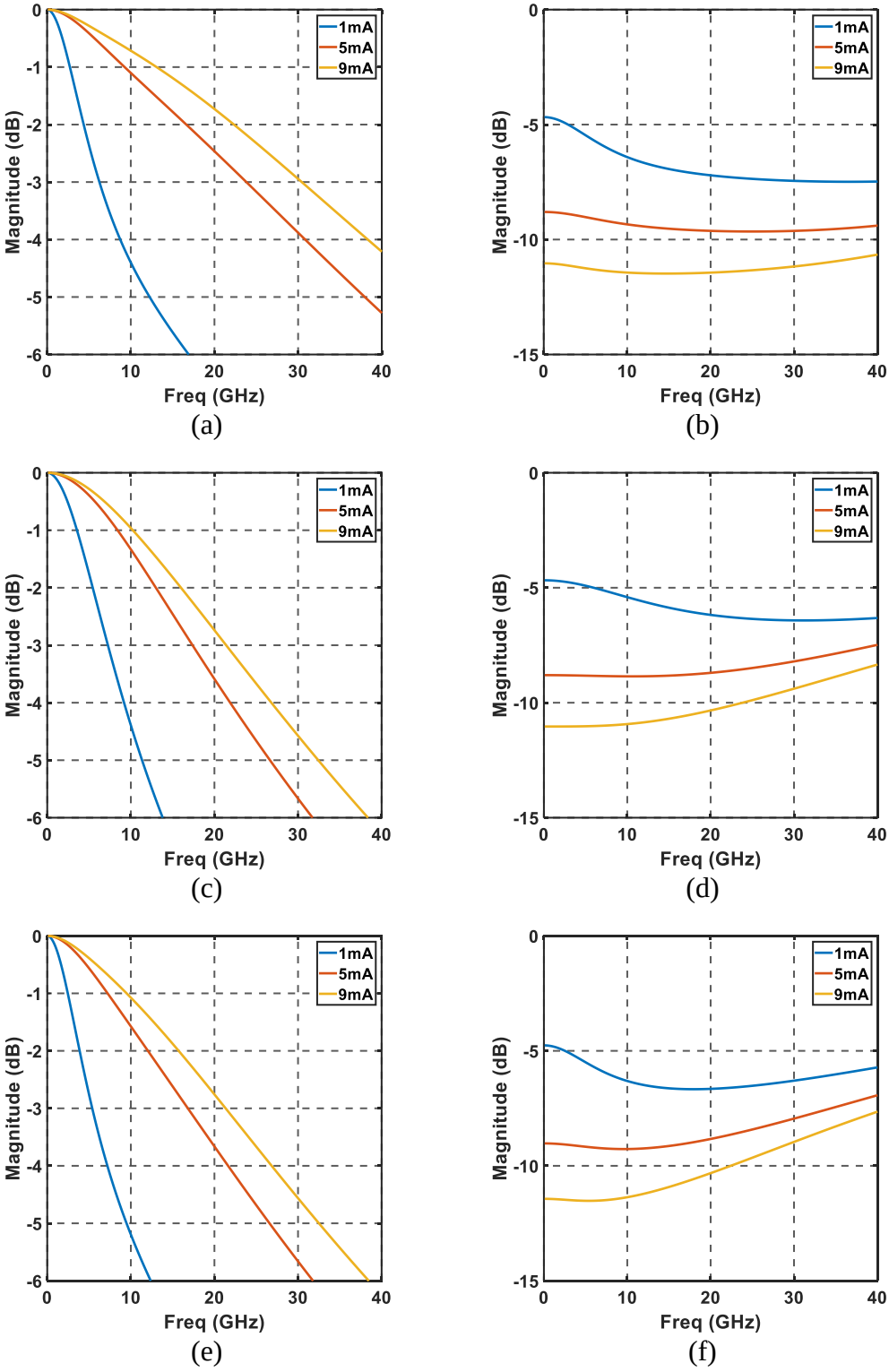

Figure 5. 10 Parasitic/S_{11} response after reduction of only (a)/(b) active area capacitance Ca by 30% through possible addition of tapered oxide layers, (c)/(d) pad capacitance by 50% Cp by reducing pad size/thickness, and (e)/(f) Bragg mirror resistance by 30% by using graded Bragg mirror designs.

in which these devices operate, especially their effects on the small signal frequency response. At high currents we see that the Bragg mirror resistance R_m and pad capacitance C_p are not as sensitive to current variations. Furthermore, the resistance, R_a, of the active area and oxide layer decreases with increasing current, while the capacitance C_a increases with increasing current. The small increase of the active area capacitance is primarily due to diffusion current and its dependence on the diffusion capacitance of the junction.

Figure 5.9 illustrates the impact of the various parasitic circuit elements on the S_{21} and S_{11} response. We would like to note that these parasitic bandwidths are similar to those extracted using our single and multimode parameter extraction methods with no apriori knowledge of the parasitic elements. Furthermore, we see that as we move to lower currents, the parasitic filter response deviates from the simple single pole lowpass filter. VCSELs at lower bias currents and/or higher extinction ratios, it is imperative that one accurately capture and models the parasitic effects at these low and high currents. Figure

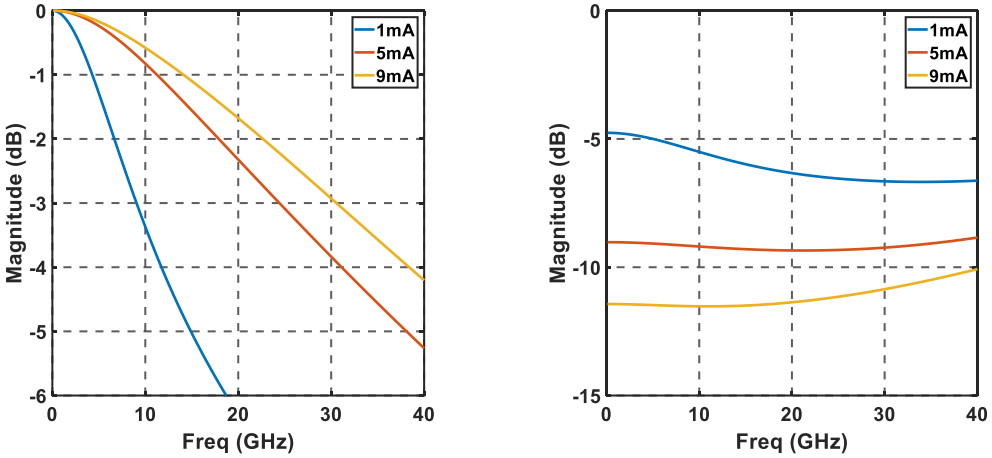

(a) (b)

Figure 5. 11 Parasitic (a) and S_{11} (b) response when Ca is reduced by 30%, C_p by 50%, R_m by 30%. Parasitic frequencies at higher currents will be reduced, and low bias parasitic frequencies have been pushed to ~10GHz. This may allow for faster VCSEL data rates with higher extinction ratios.

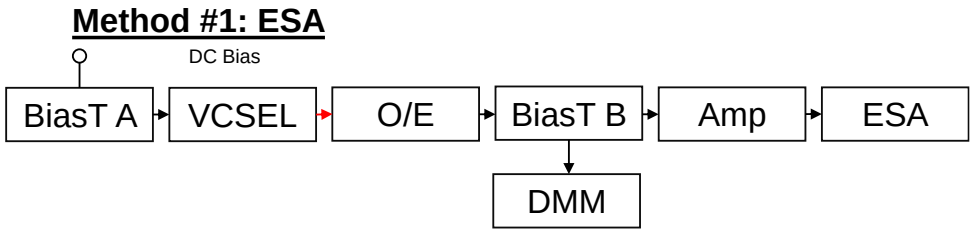

(a)

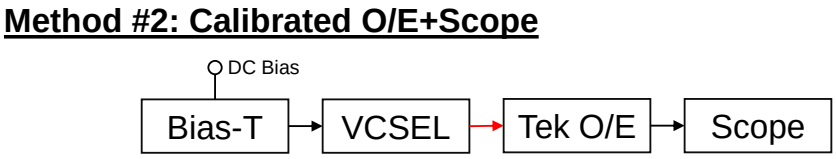

(b)

Figure 5. 12 RIN measurement setups for characterization of laser noise. Capture of VCSEL spectrum using an ESA(a) as well as the average RIN parameters through the use of a calibrated O/E and scope pair (b) provides self-consistency and further enables accurate representation of data. Optical domain paths depicted in red.

5.10 depicts the dependence of the parasitic frequency at low and high bias currents and its effect on various reductions of parasitic circuit elements. Figure 5.10a depicts a reduction of the active and oxide region are by 30%, as we have previously stated the diffusion capacitance here is small and contributes very little. Therefore, most of the capacitance is associated with the oxide layer. A reduction in the oxide layer capacitance can be achieved through thicker oxide layers or by increasing the number of oxide layers. This will help push parasitic limitations past 30GHz. While the addition of tapered oxide layers would increase the resistance in our model, this effect has been shown to be negligible [68].

5.1.3 RIN Experimental Setup

For characterization of VCSEL noise properties, bias dependent RIN measurements are needed, and RIN effects must be captured in our models. Figure 5.12 depicts two laser RIN characterization setups. Method 1 uses a bias-t with a 50ohm load on the RF port. Here

our O/E is the Thorlabs with a frequency response shown in Fig 5.2. The O/E was loaded with a bias-t in order to measure current out of the detector. The amp in this system was used to increase our sensitivity by amplifying RIN to a level above the noise floor of the ESA. Before any RIN measurements the noise of the system was measured without any input light. This background noise was then used to remove noise that is not inherent to the VCSEL itself. RIN can then be calculated as the ratio of the mean square optical intensity noise in a 1-Hz bandwidth $\langle \Delta P^2 \rangle$, divided by the average optical power, P, such that:

$$\mathrm{RIN} = \frac{\langle \Delta P^2 \rangle}{P^2}\ \mathrm{dB/Hz} \tag{5.4}$$

Since the ratio of the optical powers squared is equivalent to the ratio of the electrical power measured by the ESA and/or power meter, RIN can be calculated in terms of electrical power which can be easily measured:

$$\mathrm{RIN} = \frac{N_{\mathrm{electrical}}}{P_{\mathrm{electrical}}}\mathrm{dB/Hz} \tag{5.5}$$

Here $N_{\mathrm{electrical}}$ is the ESA photocurrent's power spectral density, and $P_{\mathrm{electrical}}$ is the average power of the photocurrent. In order to capture only the laser noise, removal of thermal, system noise and shot noise is required. Therefore, the laser intensity noise, N_L, is calculated by subtracting the values of thermal, N_{th}, and shot noise, N_{shot}, for the measured system noise, N_{sys}:

$$N_L = N_{\mathrm{sys}} - N_{\mathrm{shot}} - N_{\mathrm{th}} \tag{5.6}$$

Therefore, RIN can be calculated as:

$$RIN_{\text{laser}} = \frac{N_L}{P_{\text{electrical}}} \tag{5.7}$$

Or can be calculated in more easily measured units of optical power:

$$RIN_{\text{laser}} = \frac{N_{\text{sys}}}{P_{\text{electrical}}} - \frac{N_{\text{th}}}{R_L\left(P_{\text{opt}}\Re\right)^2} - \frac{2q}{P_{\text{opt}}\Re} \tag{5.8}$$

Here, $\Re$ is again defined as the responsivity, when an amplifier is used, the responsivity in volts/watt, $\Re_v$, is required, such that it is measured from the reference plane after the amp:

$$\Re_{\text{amp}} = \frac{\Re_v}{R_L G_v} \tag{5.9}$$

Here, G_v is the electrical gain of the amplifier.

Table 5. 1 Average RIN Parameter (0-33GHz)

Current (mA)	ESA RIN (dB/Hz)	Scope RIN (dB/Hz)	Discrepancy (dB)
1	-126.8	-128.0	1.2
2	-137.1	-138.1	1
3	-137.8	-141.1	3.3
4	-142.2	-143.7	1.5
5	-145.8	-145.2	0.6
6	-140.9	-144.8	3.9
7	-147.1	-145.8	1.3
8	-146.5	-148.7	2.2
9	-147.8	-147.4	0.4

Measured data using this method has been previously shown in Fig 4.8. Note that in (5.8), both the system and thermal noise terms are frequency dependent. In our experiments (5.8) is used mainly used when calculating intensity noise as a function of frequency through method 1 of Fig 5.12a. When measuring intensity noise through method 2, only the average RIN parameter can be extracted. RIN using these methods is calculated using (5.4). The measured RIN and the discrepancies in these two systems are compared in Table 5.1. As shown, these two systems measure RIN within a similar range. A maximum discrepancy of 3.9dB and an average discrepancy of 1.7dB is observed. This discrepancy is likely due to the RIN peaking observed in the spectra of Fig. 4.8 and further explained in Appendix A. This peaking may likely be filtered out or dampened in the O/E scope setup. Therefore, due to the sensitive nature of RIN and the systematic discrepancy that is likely possible in the O/E+scope setup we believe these discrepancies are within a reasonable range. This discrepancy might be further reduced by knowing the frequency response of the O/E + scope pair.

5.2 Simulation of VCSELs in Optical Links

In this section we will use the single and multimode VCSEL models in conjunction with measured data to simulate VCSELs at multiple operating conditions. We will also study the extrinsic and intrinsic properties of VCSELs and possible ways to achieve extrinsic VCSEL bandwidths past 30GHz. For accurate simulation of VCSEL extrinsic and intrinsic it important to characterize optical link components as done in section 5.1. Measurements capturing the extrinsic VCSEL behavior can then be made by removing any limitation that is not caused by the VCSEL itself. Simulations are then compared to experimentally measured PAM-4 eye diagrams spanning from 26 to 46 Gbaud.

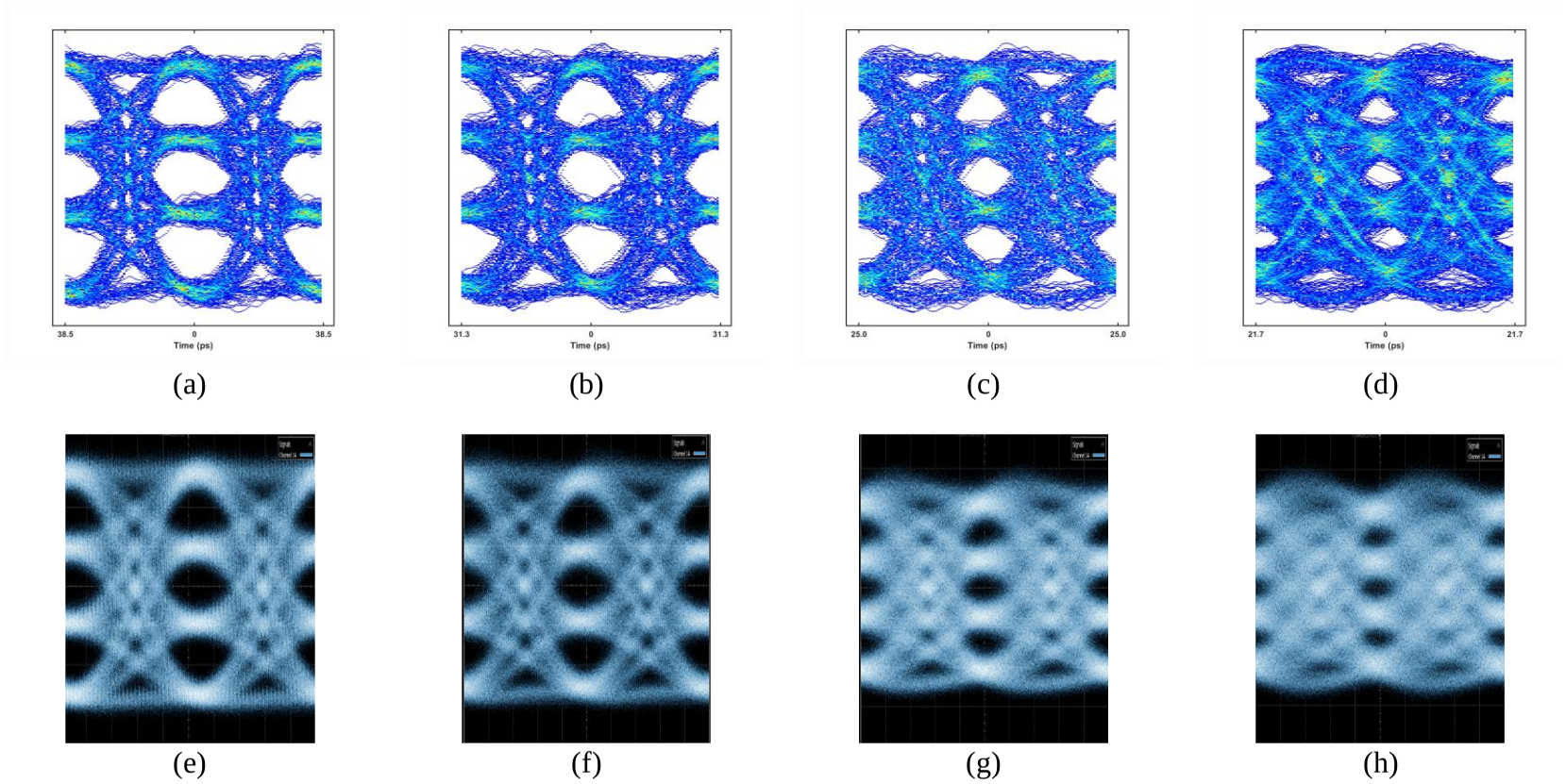

Figure 5. 13 Simulated (a-d) and experimentally measured (e-h) PAM-4 eye diagrams at baudrate/bitrates of (a,e) 26Gbaud/52Gbps, (b,f) 32Gbaud/64Gbps, (c,g) 40Gbaud/80Gbps, (d,h) 46Gbaud/92Gbps. Simulated data accurately captures laser dynamics at multiple bit rates using a singleset of laser rate equations and bias dependent parasitics previously discussed.

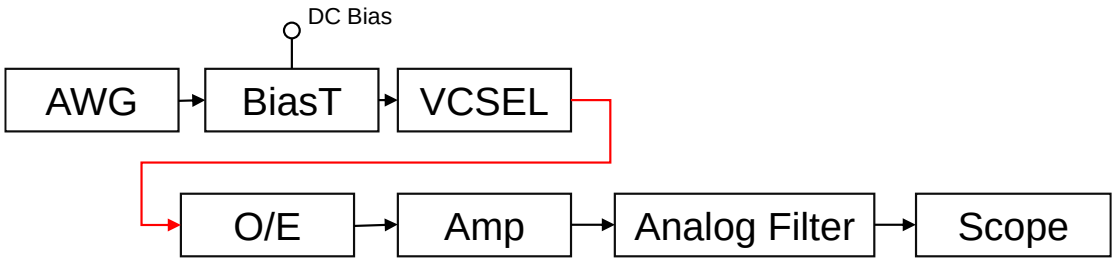

Figure 5. 14 Experimental setup used to measure eye diagrams

Figure 5.13 shows simulated and experimentally measured PAM-4 eye diagrams at 26, 32, 40, and 46 Gbaud, which correspond to bitrates of 52, 64, 80, and 92 Gbps respectively. Eye diagrams here were taken using the setup depicted in Fig. 5.14. It can be seen from Fig. 5.13 that there is also a good match between the simulated and experimental PAM-4 eyes at a wide range of bitrates. This demonstrates that parameter extraction relying on RIN spectra and modulation responses at multiple bias currents enables accurate simulation of large signal scenarios like PAM-4 modulation. It can also be seen that a single set of laser parameters is reasonably accurate for data rates up to 46 Gbaud, provided both bandwidth and noise characteristics are accurately captured. As we move toward higher

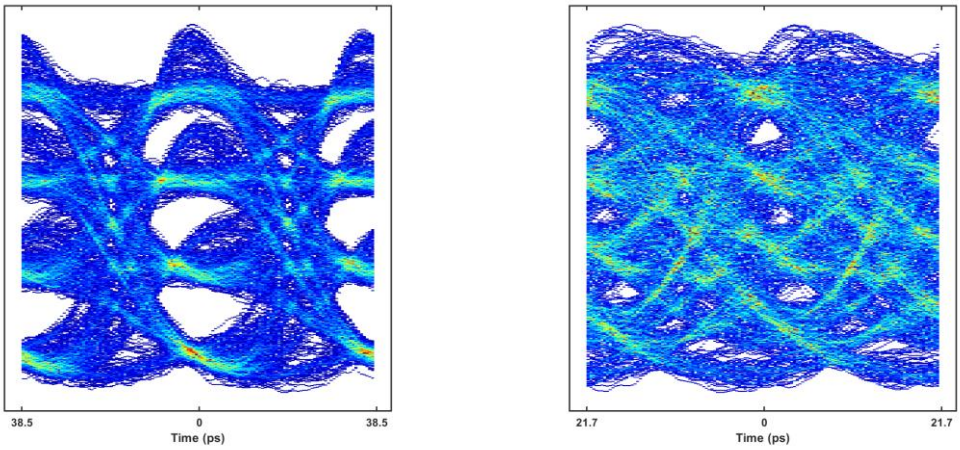

(a) (b)

Figure 5. 15 Simulated eye diagrams with lower bias current at (a) 26Gbaud and (b) 46Gbaud. Overshoots are clearly visible in (a) are due to the resonant peaking in the frequency response as we move toward lower bias currents.

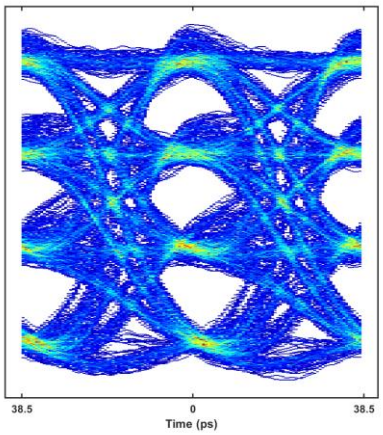

Figure 5. 16 Reduction of overshoots in 26Gbaud eye diagram as seen in Fig. 5.15a is possible by addition of 18GHz lowpass filter

bitrates the eye height of the experimentally measured eye diagrams does decrease, this is primarily due to AWG limitations which has a bandwidth of ~32GHz. Therefore, bitrates above 40GHz will see a small hit in drive amplitude due to the electrical driver limitations which we have not yet captured in our model.

Figure 5.15 demonstrates that our model is able to capture eye skew and overshoots experienced at lower bias currents. Overshoots caused by resonance peaks can be minimized by choosing the appropriate filter as shown in Fug. 5.16. Furthermore, by reducing parasitic impairments as described in section 5.1.2, we showed a -3dB parasitic bandwidth of 30GHz is possible. Eye diagrams at 40, 46, and 52 Gbaud are shown in Fig 5.17 depicting this reduction in parasitic impairments. The effect of this reduction is noticeable and shows that 100Gbps links are possible if VCSEL parasitics are reduced. Minor equalization and low latency FEC would further improve link.

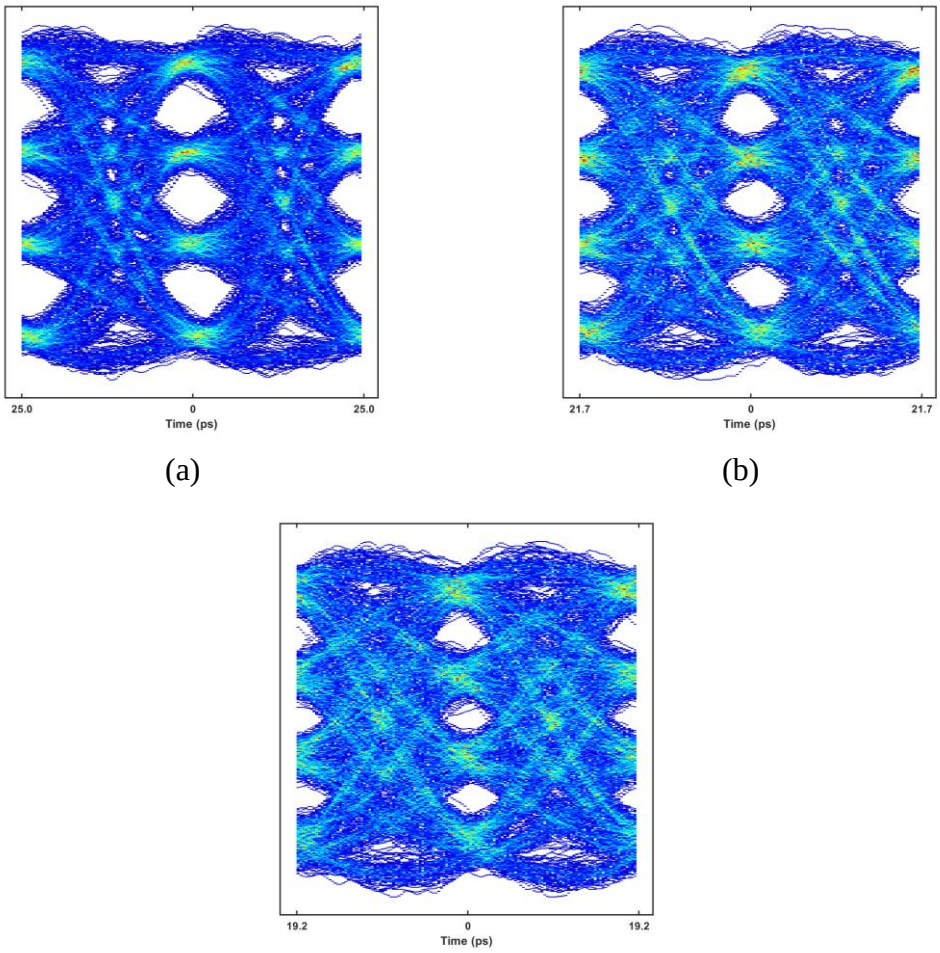

(a) (b)

(c)

Figure 5. 17 Simulated PAM-4 eye diagrams with reduced parasitic impairments at (a) 40Gbaud/80Gbps, (b) 46Gbaud/92Gbps and (c) 52Gbaud/104Gbps.

CHAPTER 6

CONCLUSION

Increasing bitrate requirements in short reach, high-speed VCSEL based optical links have made it necessary to use a physics-based laser model to capture noise and nonlinear effects. The reliability of these models depends on the extent to which they can reproduce experimental results. As we move towards higher speed existing filter-based models are insufficient and rate equation-based modelling is necessary to understand link limitations. For example, as bitrates move past 25Gbaud and as PAM-4 links are becoming widely deployed, simple gaussian approximations are insufficient. Laser parameter extraction tools using such models are both challenging and critical for proper link simulation and optimization. VCSEL deployments are still expanding and replacing traditional electrical copper links due to significantly higher speeds, superior cable management and lower cost. However, RIN, modal dispersion, chromatic dispersion, MPN, VCSEL nonlinearities, and lack of polarization control limit the achievable fiber reach. The use of equalization and multilevel modulation formats in direct detect optical links has made it critical to develop tools capable of accurately simulating noise along with the dynamic and transient properties found in VCSEL optical links.

Laser rate equation-based modelling and the associated parameter extraction have been studied in the past for a range of operating conditions. However, to the best of our knowledge, there exists no parameter extraction methodology that simultaneously captures the spectral characteristics of the frequency response $\left(H(\omega)\right)$ and RIN $\left(RIN(\omega)\right)$ over multiple drive currents for VCSELs or any other directly modulated laser (DML). In

chapter 3 we were able to show that a single set of laser rate equation parameters is able to accurately capture the effective small signal frequency response as well as the RIN spectra over a large range of bias currents. Capturing this is critical for ensuring consistency between experiments and simulation environments, especially for the large voltage/current swings of PAM-4 modulation. Further it is also necessary to optimize VCSEL performance and minimize limitations in various laser designs. Here, we also demonstrated a multi-objective parameter extraction technique that is capable of accurately extracting laser rate equation parameters from experimental data. In chapter 4, we were able to demonstrate a generic parameter extraction methodology for multimode laser rate equations which we applied to VCSELs. Here we showed that RIN at lower frequencies is dominated by the spatial overlap of VCSEL transverse modes and further exacerbated by spatial filtering caused when launching VCSEL modes into fiber modes. Through this extraction process, we demonstrate the bias dependence of the VCSEL parasitics.

The use of equalization, pulse shaping and multilevel modulation formats to achieve higher baud rates in direct detect optical links has made existing VCSEL models insufficient. This is largely due to the fact that equalization and the increasingly popular 50+ Gbps PAM-4 format are RIN sensitive. Furthermore PAM-4 systems typically use transmitter and receiver equalization and operate under reduced SNR owing to the now standard use of FEC. Therefore, the RIN and BW spectrum must be jointly accounted for to accurately model VCSEL limitations. In Chapter 5 showed the extrinsic and intrinsic properties of VCSELs. Here we showed that existing VCSEL designs are limited by parasitics which are mainly dominated by the capacitance of the active area. Furthermore,

we demonstrated by reducing parasitics that existing VCSEL extrinsic behavior can support 100Gbps operation with slight equalization.

As we push toward faster data rates coupled cavity VCSELs have gained traction. Recent publications show small signal response of over 50GHz. While impressive, it is still yet unknown whether the entire bandwidth can be translated to large signal modulation. Rate equation modelling along with parameter extraction would be beneficial in this domain especially since coupled cavity VCSELs have a small signal frequency response which largely deviates from its single cavity counterpart.

APPENDIX A

POLARIZATION NOISE CHARACTERISTICS OF MULTIMODE VCSELS

It has been shown that the optical energy in a VCSEL can move from mode to mode, and switch polarization during an optical pulse, or even randomly in time and temperature. Significant mode competition effects can also be observed in VCSELs as the device is coming to equilibrium and has been classified as mode partition noise (MPN). MPN has been shown to increase RIN through the fiber. Though these effects can be slightly mitigated in fiber, they are becoming a limiting factor as we push for higher speeds. The performance of high-speed VCSEL-MMF links is highly dependent on relative intensity noise (RIN), mode partition noise (MPN) and the preferential coupling of VCSEL modes to fiber modes resulting in a performance difference between the various differential modal delay (DMD) profile tilts of the fiber. Polarization instabilities have previously been studied in VCSELs [85]. Polarization switching is believed to be the main cause of peaking in the RIN spectrum not caused by the intrinsic resonance and bandwidth characteristics of the laser. As PAM-4 becomes more widely used in VCSEL optical links standard RIN is becoming a more important factor in setting up optical links due to its less stringent bandwidth requirements. Therefore, noise fluctuations that were previously not a factor in PAM-2 links are more important due to the eye closure both vertically due to more levels and smaller extinction ratio per eye as well as horizontally due to ISI. Therefore, the cause of RIN peaking is important to address. These RIN peaks can lead to a high increase in

noise if not corrected due to both polarization effects in the fiber as wells as spatial coupling.

In this work we analyze the spectrums from two similar 850nm VCSEL designs. We demonstrate the small signal frequency response and RIN spectrum dependence on bias current. We also demonstrate the dependence on external filtering by showing both orthogonal polarizations. We are able to measure sub-mode frequencies by using the second order diffraction spectrum from the diffraction grating. VCSEL A is characterized by three dominant modes and two RIN spectrum peaks caused by polarization switching in the third mode. VCSEL B is characterized by one dominant transverse mode, yet RIN peaking still occurs at 2 different locations. Therefore, we believe peaking is due to intermode interactions.

In these experiments we use a Yokogawa AQ6370D OSA to determine the polarization of each mode. I general the second order diffraction is an unwanted side effect in an OSA and is classified as a “grating ghost”. For example, if 850 nm light is input the input, a horizontal line at 850 nm on the vertical axis will appear, and the point of intersection on the graph of the line is the displayed wavelength. Furthermore, you will be able to see that besides 850 nm light, a grating ghost appears at 1700 nm. Higher order diffractions can be measured but these require a longer wavelength range source which is not widely available in the market.

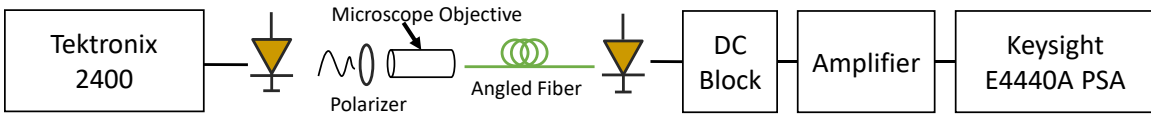

Fig. A.1. Experimental setup: angled fiber was used to mitigate reflections, bandwidth contributions from photodiode, DC block and amplifier were measured and removed using LCA/VNA Keysight module

A.1 Experimental Setup

Experimental setup is depicted in Fig. A.1. Bias current was controlled by a Keithley 2400 source from Tektronix and temperature was controlled with a TEC. Angled fiber was used in order to reduce reflections. A Keysight power spectrum analyzer (PSA) was used for RIN measurements. Contributions from thermal noise, the photodetector, DC block and amplifier were subtracted from the intensity noise spectrum. The Yokogawa AQ6370D was used with a similar setup was used to measure the optical spectrum and second order diffracted spectrum. The Keysight PSA was used to measure the small signal frequency response of the VCSEL. Experiments were tested with a microscope objective and a lensed fiber setup. No notable difference of RIN peaking was seen between the two when the polarizer was not present. Microscope objective was chosen due to ease of use since a polarizer between the VCSEL and lensed fiber would be difficult to adjust without moving the entire setup. All experiment were run at 25C. Polarizer was placed before light was coupled into fiber to avoid any crosstalk between polarizations. Polarization states were found by adjusting the polarizer until max power was reached and then rotating by 90 to

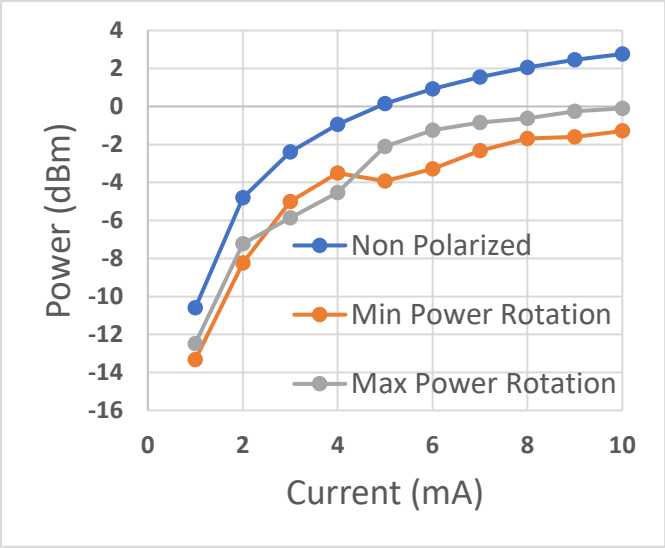

Fig. A.2. LI curve for VCSEL A

achieve the other polarization state. VCSEL A can be described as a multimode VCSEL with 3 high dominant modes, its LI curve with both orthogonal polarizations is shown in Fig. A.2.

B.1 Second Order Diffraction

To increase the resolution of our OSA we used the second order diffraction readings to separate modes. Separation within mode groups an RIN peaking were then used to correlate the cause of RIN peaking. Figure A.3 shows the spectrum from the second order diffraction overlaid on top of the first order diffraction reading. Second order diffraction shows higher attenuation and therefore cannot be used at lower bias currents to analyze modes at powers below a certain power threshold. Our OSA's finest resolution went from 0.02nm to 0.01nm, corresponding to a frequency resolution going from 8GHz to 4GHz at 850nm. This meant that worst case measurement differences between the ESA and OSA would be no more than 2GHz. We found this to be well within our required tolerance for this analysis.

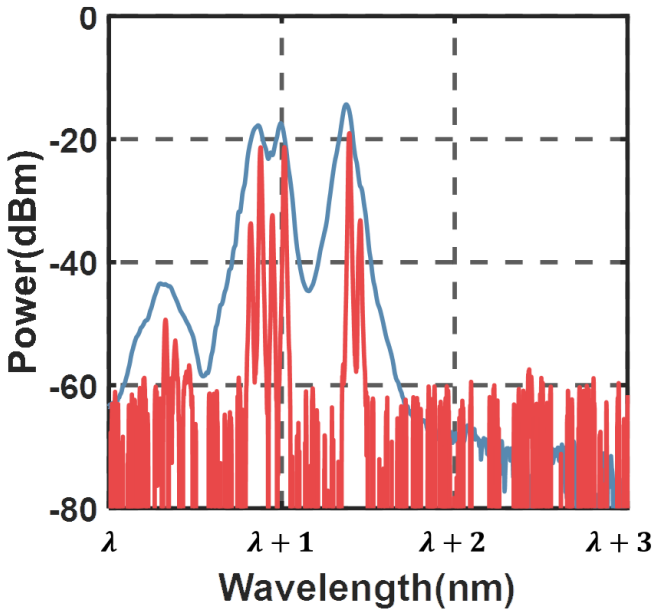

Fig. A.3. 1st order spectrum (blue) vs 2nd order spectrum (red), wavelength at the second order were halved in order to correlate with 1st order spectrum

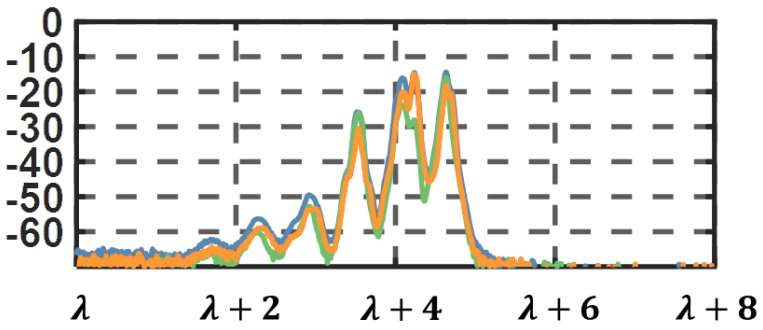

(a)

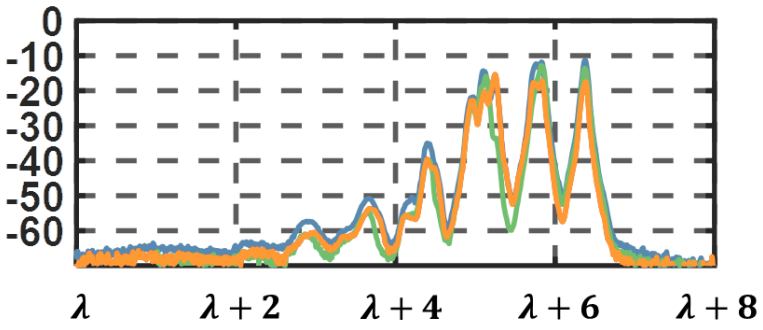

(b)

Fig. A.4 VCSEL A spectrum at (a)2mA and (b)6mA at different polarization states

VCSELs are not designed to emit in a single polarization state. At threshold, all VCSELs will generally lase in a single polarization angle. However, as more modes appear, there is no control on the polarization. Typically, the polarization is along the two orthogonal cleavage planes of the GaAs substrate. In a typical VCSEL operating above threshold, both polarization states are present. Since the polarization is not controlled, it can also randomly switch during normal operation, and even from pulse to pulse. It is therefore critical that there be no polarization selective optics in the VCSEL beam path. Finally, these polarization flips do not typically present problems with operation on multimode fiber optics as the polarization dispersion is negligible for the short distances spans typically deployed.

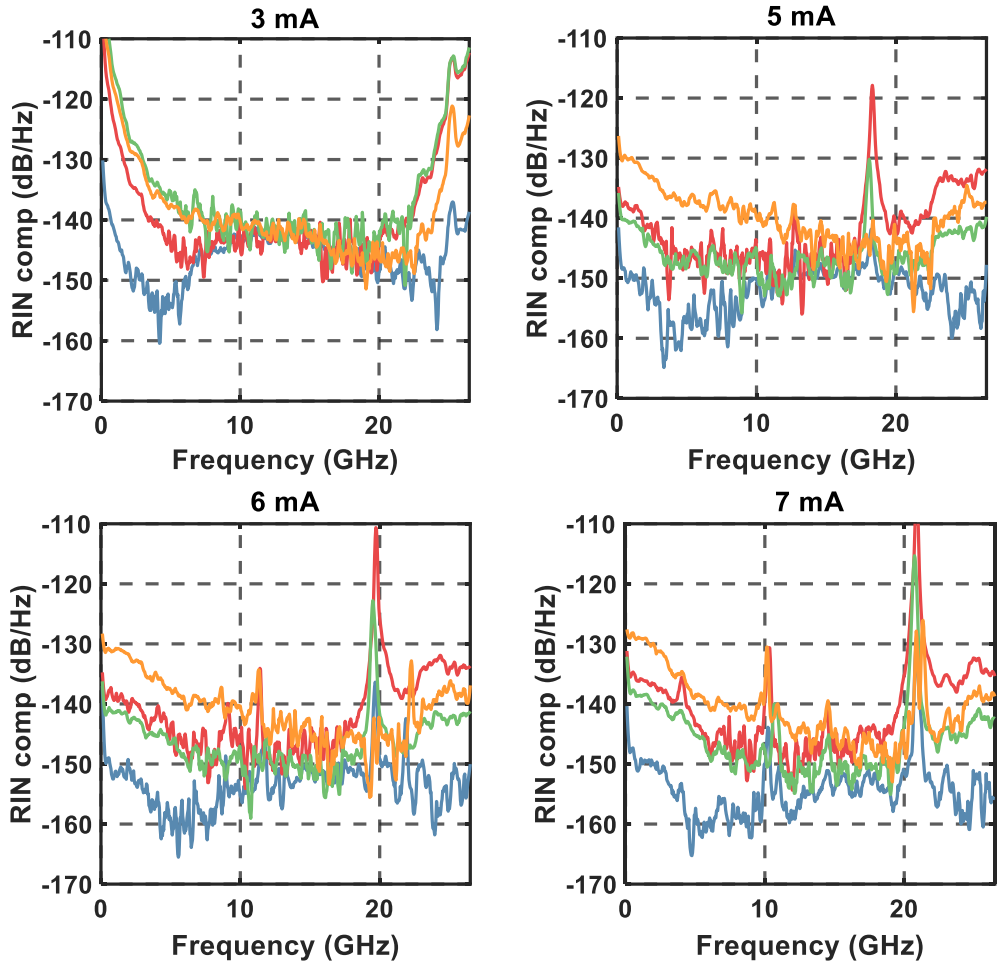

Fig. A.5. RIN Spectrum for VCSEL A 2mA-7mA, blue curves correspond to no polarization filter. Red, green, and yellow curves show evolution of RIN as polarization changes.

C.1 Experimental Results

Optical spectrum of VCSEL A is show in Figure A.4. It has an aperture of around 7um, with a threshold current of 0.7mA. Figure A.5 depicts the RIN spectrum of the VCSEL over a wide range of bias currents and external polarizations. High RIN peaks appear at higher currents and do not appear to be caused by the resonance frequency of the modes. As stated before, these peaks do not seem to affect the frequency response of the VCSEL. There also seems to be a small difference of around 1dB between the VCSEL polarization states. Therefore, even small power fluctuations between and within mode groups can

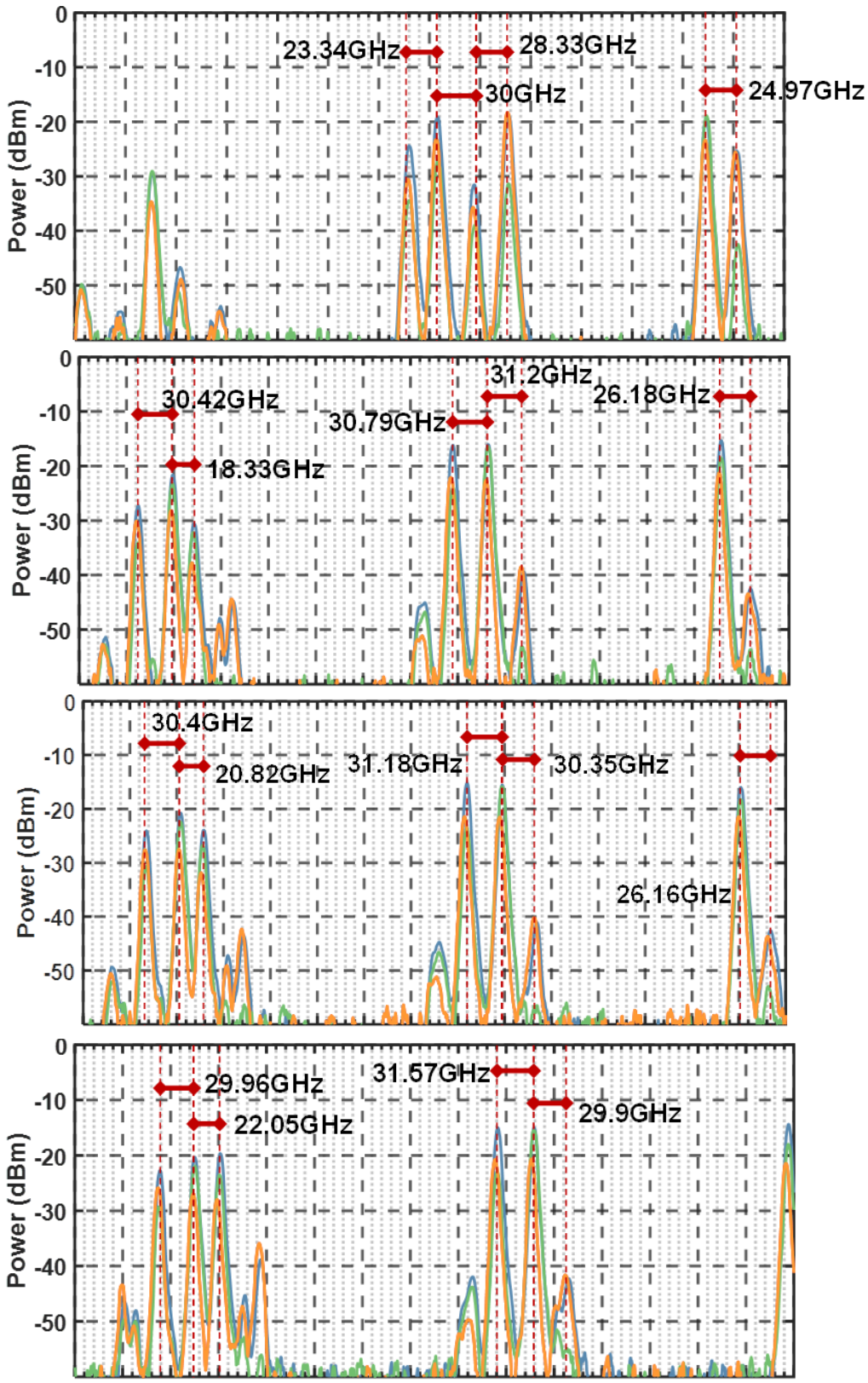

Fig. A.6. Second order spectrum at 3mA, 5mA, 6mA, 7mA (top to bottom)

greatly influence the RIN. Peaks seem to be somewhat dependent on polarization as seen in Fig A.5. The low frequency RIN enhancement can be explained as MPN due to mode selective losses. This effect is pronounced when a polarizer is inserted and as we increase bias currents.

Figure A.6 shows the optical spectrum with the corresponding frequency separation that corresponds to the adjacent mode. At low bias currents high RIN peaking can be seen at around 25GHz. At 5mA these tend to subside and a new peak at ~18GHz is clearly present. As we move toward higher currents RIN peaking shifts to higher frequencies. The 5mA peak which starts to form at around 18.3GHz corresponds to separation of modes in the third mode group. Smaller peaking also begins to occur 13GHz but does not seem to correspond to any discernable mode separation. As we move toward higher current the peaking keeps increasing. The same two modes within the mode group seem to be the culprit. Between 5 and 7 mA we see a linear trend between RIN peaking and current. The RIN spectrum shows three peaks not caused by classical resonance. While multimode VCSELs may not share the same carrier reservoir as edge emitters, RIN peaking has not been found to be a fundamental source of RIN peaking and therefore photon beating, may play an effect on this phenomenon. A higher number of carrier reservoir would lead to extra peaks, but these would also be apparent in the VCSEL frequency response of the laser. What we are looking for are small fluctuations which would not affect the small signal response of the multimode VCSELs but would affect its RIN. Therefore, polarization switching seems to be the fundamental cause.

The frequency and magnitude changes with bias current. This is different than seen in [85], [86]. Shift in frequencies might be due to the VCSEL having higher self-heating

effects which is a side effect of higher bandwidth VCSELs. It is important to note that these VCSEL have significantly low RIN and that even small changes in power distributions could easily affect the RIN spectrum which could have been hidden or negligible on VCSELs with higher RIN.

PUBLICATIONS

Thesis Related Work:

A. Melgar, V. A. Thomas, and S. E. Ralph, "Multi-Objective Laser Rate Equation Based Parameter Extraction Using VCSEL Small Signal Response and RIN Spectra," Journal of Lightwave Technology, vol. 38, no. 23, pp. 6437-6445, 2020.

A. Melgar, V. A. Thomas and S. E. Ralph, "Multimode VCSEL Parameter Extraction for Optical Link Models," in ECOC, 2018.

A. Melgar, V. A. Thomas, J. Lavrencik and S. E. Ralph, "Parameter Extraction through Joint Optimization of Modulation Response and RIN Spectra," in OFC, 2018.

A. Melgar, V. A. Thomas, J. Lavrencik, S. Varughese and S. E. Ralph, "Experimentally benchmarked fiber propagation model for 50Gbps PAM-4 MMF links employing multimode VCSELs," in OFC, 2017.

Future Publications:

A. Melgar, V. A. Thomas, B. D.B. Klein and S. E. Ralph, “Stochastic Multimode VCSEL Rate Equation Model and Parameter Extraction with MPN” J. Lightwave Technol. 2021.

Other Publications:

S. Varughese, **A. Melgar**, V. Thomas, P. Zivny, S. Hazzard and S. E. Ralph, "Accelerating Assessments of Optical Components Using Machine Learning: TDECQ as Demonstrated Example," in Journal of Lightwave Tech., vol. 39, no. 1, pp. 64-72, 2021.

V. Thomas, **A. Melgar**, S. Varughese, D. Garon, K. Tan, S. A. Hazzard, M. Agoston, P. Zivny, S. E. Ralph, "TDECQ Sensitivity to Algorithmic Implementation and Noise Characterization," in OFC, 2020.

Varughese, Siddharth, D. Garon, **A. Melgar**, V. A. Thomas, P. Zivny, S. Hazzard, S.E. Ralph, “Accelerating TDECQ Assessments using Convolutional Neural Networks.” In OFC, 2020.

J. Lavrencik, E. Simpanen, S. Varughese, **A. Melgar**, V. A. Thomas, J. S. Gustavsson, W. V. Sorin, S. Mathai, M. Tan, A. Larsson, and S. E. Ralph, "Error-Free 100Gbps PAM-4 Transmission over 100m OM5 MMF using 1060nm VCSELs," in OFC, 2019.

S. E. Ralph, J. Lavrencik, and **A. Melgar**, “VCSELs and 100G," in SPIE, 2019

J. Lavrencik, S. K. Pavan, **A. Melgar** and S. E. Ralph, "Direct measurement of transverse mode correlation and fiber-enhanced RIN through MMF using 850nm VCSELs," in OFC, 2016.

L.A. Graham, H. Chen, J. Cruel, J. Guenter, B. Hawkins, B. Hawthorne, D.Q. Kelly, **A. Melgar,** M. Martinez, E. Shaw, and J. A. Tatum "High-power VCSEL arrays for consumer electronics", in Proc. SPIE 9381, 2015.

REFERENCES

[1] J. A. Tatum et al., "VCSEL-Based Interconnects for Current and Future Data Centers," in Journal of Lightwave Technology, vol. 33, no. 4, pp. 727-732, 2015.

[2] J. Lavrencik, S. Kota Pavan, V. A. Thomas and S. E. Ralph, "Noise in VCSEL-Based Links: Direct Measurement of VCSEL Transverse Mode Correlations and Implications for MPN and RIN," in Journal of Lightwave Technology, vol. 35, no. 4, pp. 698-705, 15 Feb.15, 2017.

[3] Jim A. Tatum "Evolution of VCSELs", Proc. SPIE, 2014.

[4] A. Tatarczak et al., "Reach Extension and Capacity Enhancement of VCSEL-Based Transmission Over Single-Lane MMF Links," in Journal of Lightwave Technology, vol. 35, no. 4, pp. 565-571, 2017.

[5] G. P. Agrawal, *Fiber-Optic Communication Systems*, John Wiley & Sons, New York, USA, 1992.

[6] The Fiber Optic Association, Inc. "Fiber Optic Cable Plant Nomenclature: Types of MM Fiber," 2018. [Online]. Available: https://www.thefoa.org/tech/OM.html. [Accessed May 31, 2021].

[7] Robert Dahlgren, "Noise in Fiber Optic Communication Links", 1999. [Online]. Available: http://www.svphotonics.com/pub/pub029.pdf, (accessed May 31, 2021).

[8] IEEE 802.3, "The 10G Ethernet Link Model - IEEE 802," 2006. [Online]. Available: http://www.ieee802.org/3/ae/public/adhoc/serial_pmd/documents/10GEPBud3_1_16a.xls, (accessed May 31, 2021).

[9] J. A. Tatum, G. D. Landry, D. Gazula, J. K. Wade and P. Westbergh, "VCSEL-Based Optical Transceivers for Future Data Center Applications," OFC, 2018.

[10] G. P. Agrawal, *Optical Communication: Its History and Recent Progress*, Springer, Cham, 2016.

[11] National Archives and Records Administration, "Alexander Graham Bell's Telephone Patent Drawing and Oath," 1876. [Online]. Available: https://catalog.archives.gov/id/302052, (accessed June 27, 2021).

[12] NPTEL, "Electronics and Communication Engineering - Optical Communication," 2016. [Online]. Available: https://nptel.ac.in/courses/117/101/117101054/, (accessed June 27, 2021).

[13] T. H. Maiman, “Stimulated Optical Radiation in Ruby,” Nature, vol. 187, p. 493, 1960.

[14] K. C. Kao and G. A. Hockham, "Dielectric-fibre Surface Waveguides for Optical Frequencies," in Proceedings of the Institution of Electrical Engineers, vol. 113, no. 7, pp. 1151-1158, 1966.

[15] J. Hecht, *City of Light: The Story of Fiber Optics*. New York: Oxford UP, 1999.

[16] M. Shimizu, F. Koyama, K. Iga, “Polarization Characteristics of MOCVD grown GaAs/GaAlAs CBH Surface Emitting Lasers,” in Japanese Journal of Applied Physics, vol. 27, no. 9R, 1774-1775, 1998.

[17] M. X. Jungo, D. Erni and W. Bachtold, "VISTAS: A Comprehensive System-oriented Spatiotemporal VCSEL Model," in IEEE Journal of Selected Topics in Quantum Electronics, vol. 9, no. 3, pp. 939-948, 2003.

[18] P. V. Mena, J. J. Morikuni, S.-M. Kang, A. V. Harton, and K. W. Wyatt, "A Comprehensive Circuit-Level Model of Vertical-Cavity Surface-Emitting Lasers," Journal of Lightwave Technology, vol. 17, no. 12, pp. 2612-2632, 1999.

[19] E. S. Bjorlin, J. Geske, M. Mehta, J. Piprek and J. E. Bowers, "Temperature Dependence of the Relaxation Resonance Frequency of Long-wavelength Vertical-Cavity Lasers," in IEEE Photonics Technology Letters, vol. 17, no. 5, pp. 944-946, 2005.

[20] J. Piprek, M. Mehta, and V. Jayaraman "Design and optimization of high-performance 1.3-μm VCSELs," Proc. SPIE 5349, 2004.

[21] P. V. Mena, J. J. Morikuni, S. -. Kang, A. V. Harton and K. W. Wyatt, "A simple rate-equation-based thermal VCSEL model," in Journal of Lightwave Technology, vol. 17, no. 5, pp. 865-872, 1999.

[22] A. Valle, J. Sarma and K. A. Shore, "Spatial hole burning effects on the dynamics of vertical cavity surface-emitting laser diodes," in IEEE Journal of Quantum Electronics, vol. 31, no. 8, pp. 1423-1431, 1995.

[23] L. A. Coldren and S. W. Corzine, *Diode Lasers and Photonics Integrated Circuits*, John Wiley & Sons, New York, USA, 1995.

[24] Fiberlabs Inc., “Semiconductor Laser Diodes,” [Online]. Available: www.fiberlabs.com/glossary/about-semiconductor-laser-diode/, (accessed June 27, 2021).

[25] A.F.J. Levi., *Essential Semiconductor Laser Device Physics*, Morgan & Claypool Publishers, 2018.

[26] D. D. Bhawalkar, W. A. Gambling and R. C. Smith, "Investigation of Relaxation Oscillations in the Output from a Ruby Laser," in Radio and Electronic Engineer, vol. 27, no. 4, pp. 285-291, 1964.

[27] T. Menne and F. Rosenbaum, "Effect of Spatial Dependence in the Single-Mode Laser Rate Equations," in IEEE Journal of Quantum Electronics, vol. 2, no. 2, pp. 47-49, 1966.

[28] M. Danielsen, "A Theoretical Analysis for Gigabit/second Pulse Code Modulation of Semiconductor Lasers," in IEEE Journal of Quantum Electronics, vol. 12, no. 11, pp. 657-660, 1976.

[29] M. Morishita, T. Ohmi, J. Nishizawa, "Impedance Characteristics of Double-Heterostructure Laser Diodes," in Solid-State Electron., vol. 22, pp. 951-962, 1979.

[30] J. Katz, S. Margalit, C. Harder, D. Wilt and A. Yariv, "The Intrinsic Electrical Equivalent Circuit of a Laser Diode," in IEEE Journal of Quantum Electronics, vol. 17, no. 1, pp. 4-7, 1981.

[31] C. Harder, J. Katz, S. Margalit, J. Shacham and A. Yariv, "Noise Equivalent Circuit of a Semiconductor Laser Diode," in IEEE Journal of Quantum Electronics, vol. 18, no. 3, pp. 333-337, 1982.

[32] P. A. Morton, T. Tanbun-Ek, R. A. Logan, A. M. Sergent, P. F. Sciortino Jr., D. L. Coblentz, "Frequency response subtraction for simple measurement of intrinsic laser dynamic properties," in IEEE Photon. Technol. Lett., vol. 4, pp. 133-136, 1992.

[33] J. C. Cartledge and R. C. Srinivasan, "Extraction of DFB laser rate equation parameters for system simulation purposes," in Journal of Lightwave Technology, vol. 15, no. 5, pp. 852-860, May 1997.

[34] I. Tomkos, I. Roudas, R. Hesse, N. Antoniades, A. Boskovic, R. Vodhanel, "Extraction of Laser Rate Equations Parameters for Representative Simulations of Metropolitan-Area Transmission Systems and Networks," Optics Communication, vol. 194, pp. 109-129, 2001.

[35] Keysight Technologies Application Note, “N8836A PAM4 Design Challenges and the Implications on Test,” 2017 [Online]. Available: https://www.keysight.com/us/en/assets/7018-04746/application-notes/5992-0527.pdf, (accessed June 27, 2021).

[36] Intel Application Note, “AN 835: PAM4 Signaling Fundamentals,” 2019. [Online]. Available: https://www.intel.com/content/dam/www/programmable/us/en/pdfs/literature/an/an835.pdf, (accessed June 27, 2021).

[37] Keysight Technologies Application Note, “Error Analysis of PAM4 Signals,” 2020. [Online]. Available: https://www.keysight.com/us/en/assets/7018-06301/ application-notes/ 5992-3268.pdf, (accessed June 27, 2021).

[38] G. Shtengel, D. Ackerman and P. Morton. “True Carrier Lifetime Measurements of Semiconductor Lasers” in Electronics Letters, vol. 31, no. 20, pp. 1747-1748, 1995.

[39] Szczerba, et al., "4-PAM for High-speed Short-range Optical Communications," in Journal of Optical Communications and Networking, vol. 4, no. 11, pp. 885-894, 2012.

[40] D. Maliniak, “The Fundamentals of PAM4,” 2016. [Online]. Available: https://www.edn.com/the-fundamentals-of-pam4/, (accessed June 27, 2021).

[41] T. Toifl, et al., “A 22 Gb/s PAM-4 Receiver in 90-nm CMOS SOI Technology,” in Journal of Solid-State Circuits, vol. 41, no. 4, pp. 954–965, 2006.

[42] D. Cunningham, M. Nowell, D. Hanson, and L. Kazovsky, “The IEEE 802.3z worst case link model for optical physical media dependent specification,” 1997. [Online]. Available: http://www.ieee802.org/3/z/public/presentations/mar1997/ DCwpaper.pdf, (accessed June 27, 2021).

[43] D. Cunningham, P. Dawe, “Review of the 10Gigabit Ethernet Link Model” White Paper, 2001. [Online]. Available: https://docs.broadcom.com/doc/AV02-2485EN, (accessed June 27, 2021).

[44] K. Szczerba, et al., "4-PAM for high-speed short-range optical communications," Journal of Optical Communications and Networking, vol. 4, no. 11, pp. 885-894, 2012.

[45] J. G. Proakis, *Digital communication*, McGraw-Hill, 2008.

[46] S. Walklin and J. Conradi, “Multilevel Signaling for Increasing the Reach of 10 Gb/s Lightwave Systems,” in Journal of Lightwave Technology, vol. 17, no. 11, pp. 2235–2248, 1999.

[47] J. K. Pollard, “Multilevel Data Communication over Optical Fibre,” Optical Communications, vol. 138, no.3, pp.162–168, 1991.

[48] E. Agrell, J. Lassing, E. G. Ström, and T. Ottosson, “On the Optimality of the Binary Reflected Gray Code,” in Transactions on Information Theory, vol. 50, no. 12, pp. 3170–3182, 2004.

[49] R. Michalzik, *VCSELs: Fundamentals, Technology and Applications of Vertical-Cavity Surface-Emitting Lasers*, Springer, 2012.

[50] D. M. Kuchta, "Higher Speed VCSEL Links using Equalization," in ECOC, 2016.

[51] Y. Satuby and M. Orenstein, “Mode-coupling Effects on Small-signal Modulation of Multitransverse-Mode Vertical-cavity Semiconductor Lasers,” Journal of Quantum Electronics, vol. 35, no. 6, pp. 944-954, 1999.

[52] A. Melgar, V. A. Thomas and S. E. Ralph, "Multi-Objective Laser Rate Equation Based Parameter Extraction Using VCSEL Small Signal Response and RIN Spectra," in Journal of Lightwave Technology, vol. 38, no. 23, pp. 6437-6445, 2020.

[53] P.V. Mena, “Circuit-Level Modeling and Simulation of Semiconductor Lasers” Thesis, 1998.

[54] Y. Ou, J. S. Gustavsson, P. Westbergh, A. Haglund, A. Larsson and A. Joel, "Impedance Characteristics and Parasitic Speed Limitations of High-Speed 850-nm VCSELs," in Photonics Technology Letters, vol. 21, no. 24, pp. 1840-1842, 2009.

[55] C. Liang, W. Zhang, Q. Wang, S. Yao and Z. He, "Application-Oriented Investigation of Parasitic Limitation on Multilevel Modulation of High-Speed VCSELs," in Photonics Journal, vol. 11, no. 3, pp. 1-10, 2019

[56] M. Bruensteiner and G.C. Papen, "Extraction of VCSEL Rate-equation Parameters for Low-bias System Simulation," in Journal of Selected Topics in Quantum Electronics, vol. 5, no. 3, pp. 487-494, 1999.

[57] K. Minoglou, G. Halkias, E. D. Kyriakis-Bitzaros, D. Syvridis and A. Arapogianni, "VCSEL Device Modeling and Parameter Extraction Technique," in International Conference on Electronics, Circuits and Systems, 2007.

[58] Z. Yuan, M.V.R. Murty, S. Gupta, A. Badesha, “Modeling, Extraction and Verification of VCSEL Model for Optical IBIS AMI,” in DesignCon, 2014.

[59] "Vertical-Cavity Surface-Emitting Laser - VCSEL Validation" Optiwave, [Online]. Available: www.optiwave.com/resources/applications-resources/optical-system-vertical-cavity-surface-emitting-laser-vcsel-validation/, (accessed May 10, 2020)

[60] A. Melgar, V. A. Thomas, J. Lavrencik, and S. E. Ralph, "Parameter Extraction through Joint Optimization of Modulation Response and RIN Spectra," in OFC, 2018.

[61] L. M. Giovane et al., “Volume Manufacturable High Speed 850nm VCSEL for 100G Ethernet and Beyond,” in OFC, 2016.

[62] S. E. Hashemi, “RIN in High-Speed VCSELs for Short Reach Communication,” Thesis, 2012.

[63] B. J. Thibeault, et al., “High-Speed Characteristics of Low-optical Loss Oxide-Apertured Vertical-Cavity Lasers,” in Photonics Technology Letters, vol. 9, no. 1, pp. 11-13, 1997.

[64] Mathworks Documentation, “Multiobjective Optimization,” [Online]. Available: https://www.mathworks.com/help/gads/gamultiobj.html, (accessed May 10, 2020).

[65] R.T. Haftka, and Z. Gurdal, *Elements of Structural Optimization*, Springer, 1992.

[66] H. Dave, S.T.M. Fryslie, J.E. Schutt-Ainé, K.D. Choquette, "Modulation Enhancements for Photonic Crystal VCSELs," in Proc. SPIE, 2017.

[67] E. P. Haglund, P. Westbergh, J. S. Gustavsson and A. Larsson, "Impact of Damping on High-Speed Large Signal VCSEL Dynamics," in Journal of Lightwave Technology, vol. 33, no. 4, pp. 795-801, 2015.

[68] P. Westbergh, J. S. Gustavsson, B. Kögel, A. Haglund, A. Larsson and A. Joel, "Speed Enhancement of VCSELs by Photon Lifetime Reduction," in Electronics Letters, vol. 46, no. 13, pp. 938-940, 2010.

[69] S. E. Hashemi, Relative Intensity Noise (RIN) in High-Speed VCSELs for Short Reach Communication, Thesis, Chalmers University of Technology, 2012.

[70] J. Lavrencik, S. K. Pavan, D. K. Haupt and S. E. Ralph, "Direct Measurement of VCSEL Transverse Mode Correlation and kmpn," in IEEE Photonics Technology Letters, vol. 27, no. 19, pp. 2031-2034, 2015.

[71] J. Lavrencik, S. K. Pavan, A. Melgar and S. E. Ralph, "Direct Measurement of Transverse Mode Correlation and Fiber-Enhanced RIN through MMF using 850nm VCSELs," in OFC, 2016.

[72] J. Lavrencik, S. K. Pavan, D. K. Haupt and S. E. Ralph, "Direct Measurement of Transverse Mode Correlation and MPN using 900nm VCSELs," in OFC, 2015.

[73] H.-Y. Kao, et al., "Few-mode VCSEL Chip for 100-Gb/s Transmission over 100m Multimode Fiber," in Photonics Research, vol.5, no. 5, pp. 507-515, 2017.

[74] Y. Su, et al. “Few-mode Vertical-Cavity Surface-Emitting Lasers for Space-Division Multiplexing,” in Journal of Semiconductors, vol. 38, no. 9, pp. 094002, 2017.

[75] Chuyu Zhong et al., “Few-mode Vertical-Cavity Surface-Emitting Laser: Optional Emission of Transverse Modes with Different Polarizations” in Applied Physics Express, vol. 11, no. 5, pp. 052702, 2018.

[76] A. Valle and L. Pesquera, “Mode partition noise in multi-transverse mode vertical-cavity surface-emitting lasers,” in Proc. SPIE, vol. 3625, p. 46, 1999.

[77] A. Valle, J. Sarma, and K. A. Shore, “Spatial Hole Burning Effects on the Dynamics of Vertical Cavity Surface-Emitting Laser Diodes,” in Journal of Quantum Electronics, vol. 31, no. 8, pp. 1423–1431, 1995.

[78] J. Y. Law and G. P. Agrawal, “Mode-partition Noise in Vertical Cavity Surface Emitting Lasers,” in Photonics Technology Letters, vol. 9, no. 4, pp. 437–439, 1997.

[79] G. P. Agrawal, “Mode-partition Noise and Intensity Correlation in a Two-mode Semiconductor Laser,” Physical Review A, vol. 37, no. 7, pp. 2488–2494, 1988.

[80] F. Koyama, K. Morito, and K. Iga, “Intensity Noise and Polarization Stability of GaAlAs-GaAs Surface Emitting Lasers,” IEEE J. Quantum Electron., vol. 27, no. 6, pp. 1410–1416, 1999.

[81] J. P. Hermier, A. Bramati, A. Z. Khoury, V. Josse, E. Giacobino, P. Schnitzer, R. Michalzik, and K. J. Ebeling, “Noise Characteristics of Oxide-Confined Vertical-Cavity Surface-Emitting Lasers,” in IEEE Journal of Quantum Electronics, vol. 37, no. 1, pp. 87–91, 2001.

[82] K. H. Hahn, M. R. Tan, and S.-Y. Wang, “Intensity Noise of Large Area Vertical Cavity Surface Emitting Lasers in Multimode Optical Fibre Links,” in Electronic Letters, vol. 30, no. 2, pp. 139–140, 1994.

[83] “Modulating VCSEL”, Finisar Application Note 2007.

[84] Li, Shanglin, M. S. Nezami, D. Rolston and O. Liboiron-Ladouceur. “A Compact High-Efficient Equivalent Circuit Model of Multi-Quantum-Well Vertical-Cavity Surface-Emitting Lasers for High-Speed Interconnects,” in Applied Sciences vol. 10 2020.

[85] A. Quirce, A. Valle, C. Gimenez and L. Pesquera, "Intensity Noise Characteristics of Multimode VCSELs," in Journal of Lightwave Technology, vol. 29, no. 7, pp. 1039-1045, 2011.

[86] A. Valle and L. Pesquera, "Theoretical Calculation of Relative Intensity Noise of Multimode Vertical-Cavity Surface-Emitting Lasers," in Journal of Quantum Electronics, vol. 40, no. 6, pp. 597-606, 2004.